10-17-2022 3:00 PM

Characterization of 1D and 2D Materials with Tip-Enhanced Raman Spectroscopy

María Olivia Avilés, *The University of Western Ontario*

Abstract

Carbon-based materials, such as 1D single-walled carbon nanotubes (SWNT) or 2D graphene, are promising materials for a variety of applications in energy storage, biosensors, and medical imaging applications. Similarly, beyond graphene, 2D transition metal dichalcogenides (TMDs) that can have either a metallic or semiconducting character have gained interest for potential applications in electronics and photonics. Specifically, metallic TMDs such as vanadium disulfide (VS_2) show potential applications in optoelectronics and lithium-ion batteries. On the other hand, semiconducting TMDs like tungsten disulfide (WS_2) show a direct band gap, making them interesting for photovoltaic applications, transistors, or photodetectors. The characterization of the chemical and physical properties of such nanomaterials thus become necessary to understand their performance. Moreover, given that structural defects have a negative impact on their integration into devices understanding the formation of these defects is therefore critical. Raman spectroscopy is one of the fundamental techniques that can help to identify chemical properties of materials revealing functional groups at the surface or the presence of crystalline and structural defects. Tip-enhanced Raman spectroscopy (TERS) combines Raman spectroscopy and atomic force microscopy (AFM) to obtain spatial resolution that goes beyond the diffraction limit. TERS relies on the resonance of the local surface plasmon (LSPR) and a lightning-rod effect in the vicinity of the apex of a sharp metallic nanoscale tip, yielding to sub 20nm spatial resolution.

In this thesis, 1D and 2D carbon materials such as single walled carbon nanotubes and graphene, are characterized through TERS and artificial intelligence methods. Artificial neural networks (ANNs), a sub-field of machine learning are applied to analyze large amount of collected spectra and sort them efficiently based on their metallic or semiconductor character. 2D metallic VS_2 and semiconductive WS_2 are synthesized using chemical vapor deposition and analyzed though TERS discovering surface ripples and hidden layers. Furthermore, through the characterization of VS_2, it was found that photo-oxidation process promoted the production of vanadium oxides. Other characterization techniques such as Kelvin probe microscopy (KPFM) and nanomechanical modes were applied to reveal the electronic properties of these materials.

Keywords

Summary for Lay Audience

Nanotechnology offers numerous benefits for society including advanced materials for health, energy capture and storage, sensors, and green chemistry and chemical engineering. As technology advances and potential applications become reality, the importance of designing materials free of structural defects become of prime importance. These studies require the need of state-of-the-art instruments that facilitates the characterization of those materials with high spatial resolution.

TERS is a technique that complies with such high precision combining topography and vibrational characterization that provides precise physical geometry, structure, and crystallinity information. TERS utilizes a tip with atomic dimensions running over the surface of a sample, revealing topographical details, and simultaneously detecting molecule vibrations through localized Raman measurements. The high spatial resolution of this optical technique allows to determine the presence of defects on the material surface and their impact on the mechanical, chemical, and electronic properties.

Our study focuses on the characterization of one- and two-dimensional materials referred as 1D and 2D materials. Example of 1D nanomaterials are carbon nanotubes which have a diameter less than 1 nm and lengths exceeding hundreds of microns. Examples of 2D materials are graphene or transition metal dichalcogenides (TMDs) that can offer a variety of electronic properties varying from metallic to semiconducting. Metallic TMDs, such as vanadium disulfide (VS_2), show potential applications in optoelectronics and lithium-ion batteries, whereas semiconducting TMDs, like tungsten disulfide (WS_2), with specific band gap characteristics are of interest for photovoltaic and photodetector applications. In this work, the properties of such nanomaterials were investigated using nanophotonics tools in conjunction with nanoscale conduction measurements to better understand the properties of these materials.

Co-Authorship Statement

The thesis contains material from previously published manuscripts. Dr. François Lagugné-Labarthet was the corresponding author on the presented manuscripts and was responsible for the supervision of María Olivia Avilés Galarza throughout her studies. This thesis includes materials from four publications, which had contributions from co-authors.

María Olivia Avilés Galarza was the primary author of the published papers presented in Chapters 4 and 5, while for Chapter 3 and 6 was responsible for some experimental work.

Chapter 3:

Kajendirarajah, U.; Avilés, M. O.; Lagugné-Labarthet, F. Deciphering tip-enhanced Raman imaging of carbon nanotubes with deep learning neural networks. Phys. Chem. Chem. Phys. 2020, 22 (32), 17857-17866.

Usant Kajendirarajah who was the primary author involved in the technical aspects of the applicability of machine learning neural networks of the data. María Olivia Avilés was responsible for the sample preparation, characterization, and analysis of the TERS results while the manuscript was primarily written by Usant Kajendirarajah and Dr. François Lagugné-Labarthet.

Chapter 4:

Avilés, M. O.; Jelken, J.; Lagugné-Labarthet, F. Periodic Spiral Ripples on VS_2 flakes: A Tip-Enhanced Raman Investigation. J. Phys. Chem. Lett. 2022,13,41,9771-9776.

Synthesis and characterization and writing were performed by María Olivia Avilés, and technical advice and manuscript revision were taken from Dr. Joachim Jelken and corresponding author Dr. François Lagugné-Labarthet.

Chapter 5:

Oxides and transition metal dichalcogenide were synthesized with the help of Dr. Zhiqiang Wang and Dr. Tsung-Kong Sham in their research laboratory in at Western University. Technical advice and knowledge transfer were acquired for the synthesis method.

Chapter 6:

Jelken, J.; Avilés, M. O.; Lagugné-Labarthet, F. The Hidden Flower in WS_2 Flakes: A Combined Nanomechanical and Tip-Enhanced Raman Exploration. ACS Nano. 2022, 16, 8, 12352–12363.

Dr. Joachim Jelken was the primary author and was responsible for the AFM, QNM and analysis of the experimental data and writing the manuscript. María Olivia Avilés was responsible for confocal Raman, KPFM and TERS data acquisition. Dr. François Lagugne-Labarthet edited all María Olivia Avilés work.

Additional collaborations were done with Dr. Madalena Kozachuk, Dr. Ron Martin, Dr. Tsun-Kong Sham, Brianne Potts, Dr. Joe Gilroy, Jasveer Dhindsa, Dr. Ryan Maar, Dr. Stephanie Barbon, Zachary Powell, Dr. Leila Mazaheri, MSc. Pooneh Farhat, MSc. Sydney Legge, Dr. Zhiqiang Wang, and Ari Forman which resulted in publications that are not direct subjects of the thesis. Most of the involvement was in experimental assistance on AFM, confocal Raman measurements, FTIR and discussions.

Acknowledgments

Table of Contents

List of Tables

List of Figures

List of Appendices

List of Abbreviations

1D	One-dimension
2D	Two-dimension
3D	Three-dimension
AFM	Atomic force microscopy
ANN	Artificial neural networks
CNT	Carbon nanotube
CPD	Contact potential difference
CVD	Chemical vapor deposition
EDX	Energy dispersive X-Ray
FMM	Force modulation mode
KPFM	Kelvin probe force microscopy
LSPR	Local surface plasmon resonance
LSPR	Local surface plasmon resonance
MWNT	Multi-walled carbon nanotube
MWNTs	Multi-walled carbon nanotubes
QNM	PeakForce quantitative nanomechanics
SEM	Scanning electron microscopy
SERS	Surface enhanced Raman spectroscopy
SERS	Surface enhanced Raman spectroscopy

SPP	Surface plasmon polariton
STM	Scanning tunneling microscopy
SWNT	Single-walled carbon nanotube
TEM	Transmission electron microscope
TERS	Tip-enhanced Raman spectroscopy
TMDs	Transition metal dichalcogenides

Chapter 1

1   Introduction

In 1991, carbon nanotubes (CNT) were first images by Ijima, [1] providing the first proof of one-dimensional (1D) nanomaterials. Several years later in 2004, [2] the isolation of graphene, a two-dimensional (2D) nanomaterial, enabled the recognition of its exceptional thermal, electrical, and optical properties. With the development of new technology, the fabrication of nanoscale devices has attracted the attention of the research community around the world to improve the performances and miniaturization of a variety of electronic and photonic elements.

1D and 2D materials can be obtained through many different methodologies. However, depending on the selected synthesis pathway a change in the surface morphology and polydispersity is observed, affecting their mechanical, chemical, and electronic properties. For this reason, to understand the growth, morphology, nucleation, and topography of these materials, high spatial resolution techniques critical to understand the properties of these single building bricks. In particular, the use of tip-enhanced Raman spectroscopy (TERS), relies on the use of plasmonics to produce an enhanced and localized local electromagnetic field to yield high spatial resolution. In this thesis, we explore the synthesis of 1D and 2D materials by chemical vapor deposition, and the characterization of their and the physical and chemical properties through enhanced spectroscopy.

1.1   1D and 2D Materials

Nanomaterials have at least one of their dimensions below 100 nm and can be classified as 0D, 1D, 2D, and 3D. [3]

0D materials are usually composed of small particles in the 1 to 10 nm range such as metallic particles, fullerenes, quantum dots or other materials. 1D materials, such as nanorods and carbon nanotubes, are extended beyond the nanoscale along one direction, and present high electrical conductivity, flexibility, and strength. [3] Due to their exceptional

properties, carbon nanotubes have been used as components in transistors, sensors, [4] electrodes, nano inks for printed electronics, [5] as well in photonic and optoelectronic devices. [6]

On the other hand, 2D materials have only one dimension, generally their thickness, less than 100 nm. Layered materials such as graphene, and transition metal dichalcogenides (TMDs) have paved their applicability in different energetic storage devices generally mixed with other components or with functionalized surfaces. [7, 8]

1.1.1   1D and 2D Carbon Materials

It was in 1789 when A.L Lavoisier proposed the name "carbo" meaning coal in Latin to carbon materials. [9] These materials have several types of allotropes, which are defined as a different structural form of the same element. Allotropes include diamond, graphite, graphene, lonsdaleite, buckyball, amorphous carbon, single-walled carbon nanotube and others.

Graphene and Graphite

Graphene is a two-dimensional isolated monolayer form of carbon with atoms arranged in a honeycomb lattice. [2] It is the building block for graphite (3D), carbon nanotubes (1D) and fullerenes (0D). In 2010 Novoselov and Geim were awarded the Nobel prize for their discovery. [2] Graphene is a semi-metal or a zero-gap semiconductor without any dopants. Due to its physical and chemical properties, graphene has attracted the attention of researchers for many potential industrial applications.

Graphene is formed by mechanical exfoliating one sheet of graphite and its electronic properties are strongly dependent on the number of layers. Only monolayer and bilayer materials have a zero-gap semiconductive property with single type electrons and holes, respectively. Otherwise, when the number of layers increases between 2 and 10 (multilayer), covalent bonds provide in-plane stability while weak van der Waals like forces keep the sheets together due to the π-bonds. **Figure 1.1a, b** reveals the hexagonal carbon arrangement structure of graphene in real and reciprocal space and the **a1** and **a2**

unitary vectors that generate the lattice. The distance between carbons located in two neighboring hexagonal cells is $a = \sqrt{3}a_{C-C}$, where $a_{C-C} = 0.142 \ nm$. The lattice for the unit cell is shown as a dashed red line in **Figure 1.1a** and has two non equivalent carbon atoms A and B. **Figure 1.1b** identifies the reciprocal space represented with two-unit vectors **b1** and **b2,** rotated $90°$ from the real space unit vectors. This represents the hexagonal Brillouin zone of graphene. The figure also shows the high symmetry points Γ, K and M located at the center, corner, and center edge.

The structural configuration of the hexagonal lattice may have a zig-zag edge, armchair or a combination of both as revealed in **Figure 1.1c**.

Structures containing more layers of graphene, including thin films, are identified as graphite, and are classified as 3D materials. Graphite has been used since prehistoric times as a decorative pigment, nowadays, it continues to be used as pencils for writing and drawing. Three types of graphite can be found: amorphous, vein and flake graphite. In its natural form, is a soft material composed of layers of sp^2 hybridized carbons forming planar hexagonal rings and is also recognized because of its high thermal conductivity. Graphite layers are separated approximately by 3.35 Å and have a carbon-carbon covalent sigma (σ) bond with a length of 1.42 Å. Graphite is normally stacked in hexagonal sequence ABAB, however, rhombohedral sequence could be also obtained from milling process.
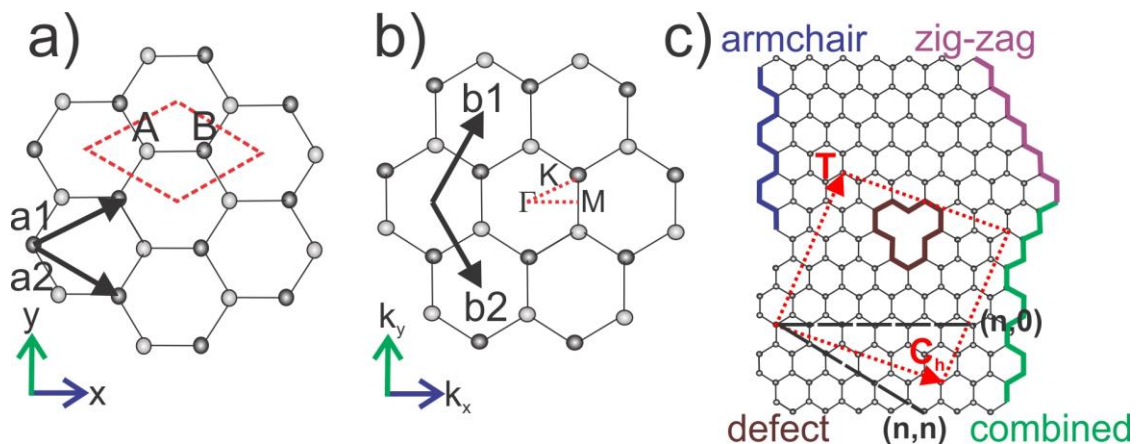
Figure 1.1 a) 2D Graphene lattice in real space. Dashed diamond shows unit cell with two carbon atoms A and B. a1 and a2 are unit vectors. b) Graphene lattice in reciprocal space showing b1 and b2 unit vectors where Γ, K and M are reciprocal symmetry points in a Brillouin zone. c) Armchair, zig-zag and combined structure as well as defect.

Carbon Nanotubes (CNT)

Carbon nanotubes (CNT) were discovered by Ijima in 1991. [1] The synthesis of the CNT was performed using the arc-discharge method and the characterization was achieved using electron microscopy techniques, determining that the structure corresponded to multi-walled nanotubes (MWNTs). Two years later, single-walled carbon nanotubes (SWNTs) were synthesized which opened a pathway for new fundamental theoretical studies of CNTs classification. [10] Nowadays, the morphology of these materials is studied through high resolution techniques such as transmission electron microscopy (TEM) and scanning tunneling microscopy (STM) to confirm their hollow cylinders arrangement derived from a honeycomb lattice. In carbon nanotubes the graphene sheet is rolled up in the direction of the chiral vector (C_h), that in combination with the translational vector (T) conforms the unit cell of the nanostructure in real space. The schematic representation is shown in **Figure 1.1c**.

It was not until 1998 that the electronic properties of the carbon nanotubes were identified. Depending on the geometrical characteristics, they are classified as semi-metallic or metallic. The remarkable mechanical and electronic properties of CNT make them appealing for industry applications. The electronic properties of CNTs are influenced by two main factors, chirality, and defects over the surface. Chirality is related to the possibility of the material or molecule being distinguishable from its mirror image, while the defects comprise a variety of morphologies such as pentagons, heptagons, vacancies, or dopants. [11] CNT can be categorized as achiral (armchair and zig-zag) or chiral depending on the primary symmetry as observed in **Figure 1.2a**. Zig-zag configuration in a nanotube corresponds to a small gap semiconductor (not entirely metallic) whereas the armchair exhibits metallic behavior. [11]

Hexagonal Brillouin zone is shown in **Figure 1.2b** where Dirac cones represent the features that occur in electronic band structures describing unusual electron transport properties. In the same figure, both metallic and semiconductive band structures are represented in the E-K plots showing the bandgap (Eg) of a semiconductive material that a metal does not possess. [12]
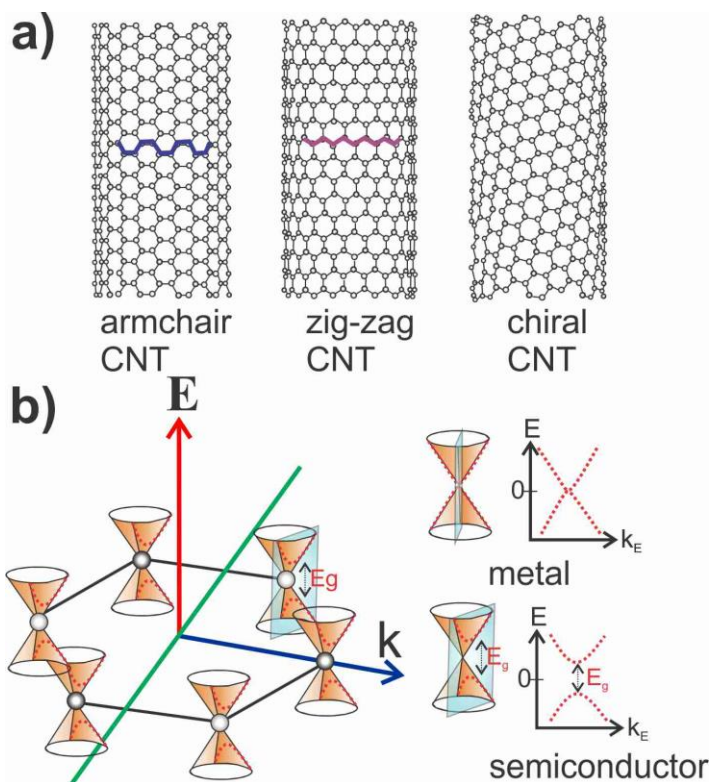
Figure 1.2 a) Classification of armchair, zig-zag, and chiral configuration of carbon nanotubes. b) Hexagonal Brillouin zone of graphene where Dirac cones are represented touching valence and conduction bands at K and K'. To the top right Dirac cones represent intersect of a K (K') point to give a metallic band structure, where a bottom right the K (K') point is missed showing the Eg band gap to give a semiconductive band structure. [12]

1.1.2   Transition Metal Dichalcogenides (TMDs)

The discovery of graphene leads to the fabrication of new 2D structures including transition metal dichalcogenides (TMDs), black phosphorus (BP), oxides, hexagonal boron nitride (h-BN), silicone and others. TMDs are made up of a metallic or semiconductor material with a MX_2 composition, where M denotes a transition metal that can be vanadium (V), tungsten (W) or molybdenum (Mo), and X represents a chalcogen such as sulfur or selenide. [13]

The different properties in TMDs are defined by the coordination of transition metal atoms and its stacking sequence that determines the phase or polymorphs. The combination of d-electron configuration and coordination determines the electrical and conductive properties off the TMDs. The trigonal prismatic and octahedral are the most important coordination structures of TMDs as it is shown in **Figure 1.3a**. In addition, there are three main phases 1T, 2H and 3R are shown **Figure 1.3b**. The numbers 1,2 and 3 indicate the non-identical layers within the TMDs. The letters indicate the resulting symmetry where T represents the tetragonal, H hexagonal and R rhombohedral. 1T TMDs are considered metallic while 2H and 3R phases are semiconductive. [13]
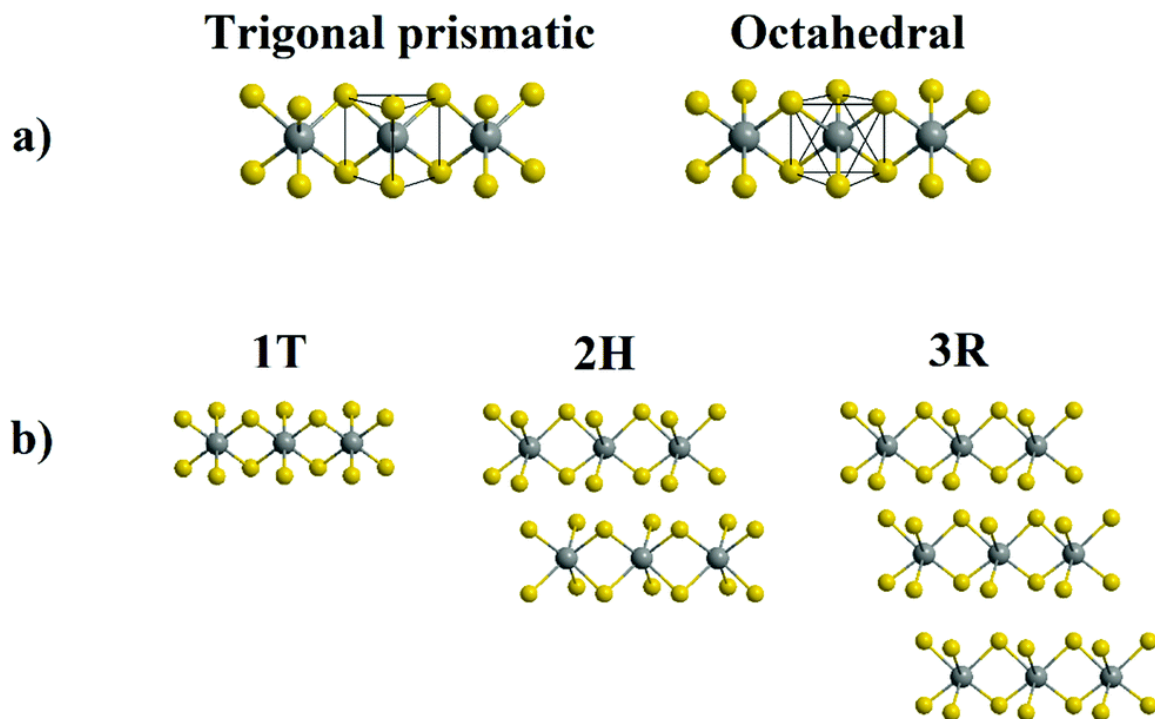
Figure 1.3 a) Trigonal prismatic and octahedral coordination in TMDs. b) TMDs polymorph phases 1T, 2H and 3R, where grey spheres represent the transition metal and yellow ones represent chalcogen atoms. [14] Reproduced from reference [14] with permission from the Royal Society of Chemistry.

In this thesis, we will focus on the synthesis and on vanadium disulfide (VS_2), and tungsten disulfide (WS_2). The oxidation process into the oxides VO_2 and V_2O_5 was also studied.

Vanadium Disulfide (VS$_2$)

VS$_2$ is a metal that has no bandgap, unlike most stable semiconductors such as MoS$_2$ whose bandgap can be tuned depending on the doping conditions or the number of layers. However, depending on the synthesized phase of VS$_2$, the conducting properties can be tuned ranging from a metallic to a semiconducting character. VS$_2$ shows a promising adjustable vanadium valence ranging from +5 to 0. It possesses interlayer distance (5.76 Å) that is large enough to insert any metal ions. Due to these properties, the potential applicability of the VS$_2$ includes the development of anode or cathode terminals of lithium batteries, [15-17] quantum computing devices, [18] in-plane supercapacitors[19, 20], sensors, [21] and as catalyzers for hydrogen evolution reactions. [22] VS$_2$ crystallizes in a layered 1T phase where the vanadium atoms are octahedrally coordinated between two layers of sulphur[23] and stacked together through weak Van der Waals interactions. [15] Besides to the 1T phase, researchers have successfully synthesized 2H phase semiconductive VS$_2$. [24] The difference between the phases is also noticed in the energy bandgap of the electronic structure, where 0.2eV implies the H-phase and a zero bandgap indicates 1T phase. The most remarkable characteristic of VS$_2$, either 2H or 1T phase, is its magnetic property. Researchers are now exploring how to understand the magnetic coupling mechanisms that other semiconductive TMDs lack. [25]

Tungsten Disulfide (WS$_2$)

WS$_2$ is structured as a triple stacked layers formed with a transition metal layer (W atom) encapsuled between two S atom layers, each with a hexagonal lattice structure. Within the three-layer stacked the W and S atoms are bonded by ionic covalent bonds and being held by weak Van der Walls forces. WS$_2$ unlike VS$_2$ has the 4 phases 1T, 1T', 2H and 3R. [26] For 2D films, the 2H phase is the most stable and common structure exhibiting a semiconductive property. 1T' phase has a well-known topological insulating characteristic, compared to the metallic properties of the 1T phase. In addition, it is possible to change WS$_2$ properties due to the irreversible phase transition between 1T to 2H produced by the application of infrared laser stimulation or electron beam irradiation. [27] WS$_2$ also displays

a direct to indirect bandgap transition that occurs when the thickness of the layers is reduced to one. During the synthesis, WS_2 can normally grow in in-plane or in axial directions. Moreover, certain studies show a super twisted spirals during the material growth.[28] WS_2 has a relatively good stability in ambient conditions,[29] superior electrical[30] and opto-electronic properties.[31]

1.1.3 Vanadium Oxides (VO_2, V_2O_5)

Among many 2D materials, metal oxides have been sporadically explored. Vanadium oxides have compounds that are diverse in their crystal structure as well as in their electronic properties.[32] Moreover, TMDs such as VS_2 appear to oxidize under laser radiation which promotes an oxidation reaction into VO_2.

The vanadium oxide VO_2 has direct application in infrared detectors because of its metal-insulator transition phase (MIT) feature which arises from a distortion in the crystalline phase. MIT can switch from monoclinic (M1) phase at room temperature to rutile type tetragonal phase (R) at 68°C. VO_2 has 14 known phases, including M1 and R, as well as A, synthesized by pulsed laser and B and D phases, obtained by hydrothermal reaction.[33, 34] Furthermore, the vanadium oxides V_2O_3, V_2O_7 and VO_2 (D) will further oxidize into their most stable compound V_2O_5 by thermal annealing. The latter oxide can also take a variety of phases, being α-V_2O_5 the most common one that crystallizes into an orthorhombic structure (space group P_{mmm}) with insulating characteristics. Vanadium-containing oxides (VO_2, V_2O_3, V_2O_7 and the more stable V_2O_5) are of particular interest for applications ranging from batteries to electrochromic,[35] and sensing devices.[36]

1.2 Applications of 1D and 2D Materials

Figure 1.4 shows a wide range of applications for 1D and 2D materials. For instance, thermal imaging requires a detection of longer wavelengths (more than 1200 nm) for which graphene is suitable as opposed to semiconductors such as WS_2 which are hardly applicable.[37] Nowadays, even fiber optics communications require 2D materials working with wavelengths in the 1200-1550nm range.[37] Light emitting diodes and displays need

emitting photons in the range of 390-700nm range. Specifically, in the field of energetic devices, batteries, supercapacitors, and optoelectronics are the most common examples of the applicability of 2D materials.
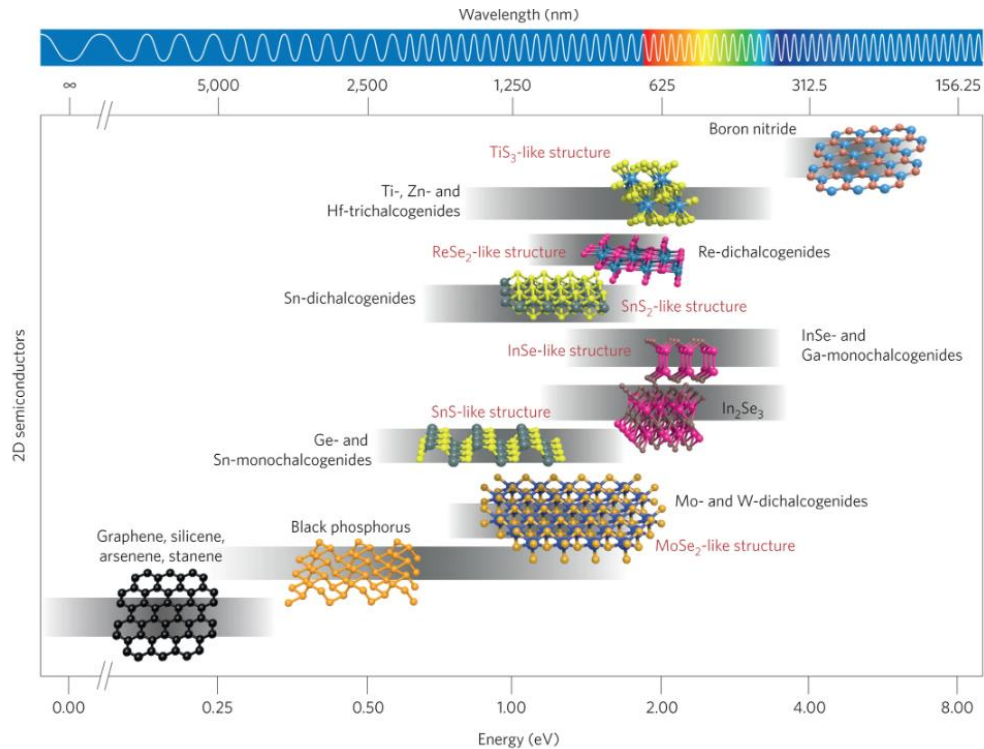
Figure 1.4 A few 2D semiconductors and their electronic band gap. Reprinted by permission from Springer Nature: Nature Photonics, Why all the fuss about 2D semiconductor?, Castellanos-Gomez, A., Copyright 2016. [37]

1.3 Plasmonics and Enhanced Spectroscopy

1.3.1 Surface Plasmons

Plasmonic nanoparticles have been used since the 4th century as evidenced by the Lycurgus cup that shows a green color under reflected light and red color under transmitted light. [38] This behavior was explained by the presence of gold, copper and silver nanoparticles contained in the cup such that when annealed at high temperature generates the change in color. In 1950s Pines and Bohm started to prove experimentally the interaction of collective

electron with the surface. [39] Surface plasmons are collective electron oscillations confined evanescently along the interface of a metal and a dielectric. [40] Unlike bulk plasmons, where the plasmon exists in the volume of the material in its longitudinal oscillation, surface plasmons exist on interfaces where is a transverse oscillation. In addition, surface plasmons has a longer lifetime and propagation distance, and through the correct and precise experiment settings, it interacts greatly with an external electromagnetic wave such as light. For the surface plasmon to be generated there must exist free electrons on one side of the interface (metal). Surface plasmons are classified as surface plasmon polaritons (SPP) and localized surface plasmons (LSPR).

1.3.2   Local Surface Plasmon Resonance (LSPR)

LSPR refers to the oscillation of electrons at the surface of metallic structures due to the interaction of the metal with incident light of a specific wavelength. Due to the small size of the nanomaterials, a confinement of the surface plasmon, known as the localized surface plasmon resonance (LSPR), is produced. The variation of the electric field of the incident electromagnetic wave produces the creation of an oscillating electric dipole by displacing the electrons and resonate in the metallic nanoparticle as illustrated in **Figure 1.5**. The metal interfaced with the dielectric acts as a nano-antenna generating a strong electromagnetic field in the near vicinity.
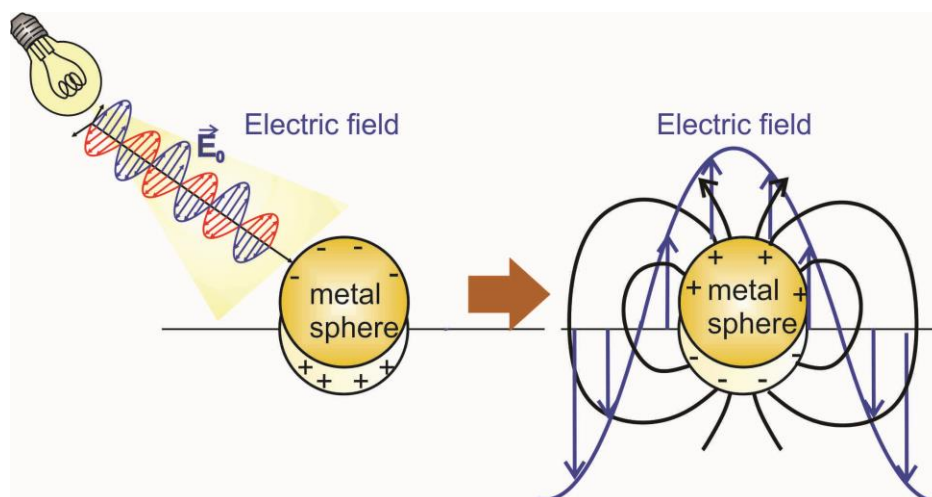
Figure 1.5 Sketch of the generation of LSPR on a metal sphere. Blue arrows correspond to the electric field and the black lines over the metal sphere correspond to the electric dipole field of the displaced electron cloud.

1.4   Characterization Techniques

1.4.1   Raman Spectroscopy

In 1928, Indian physicist Sir Chandrasekhara Raman studied the inelastic light scattering in molecules which turned out to be dependent on the nature of the molecules studies. He was awarded the Nobel Prize in 1930 for his pioneering work and the discovery of the Raman effect.

The Raman effect describes the inelastic scattering process between a photon and a molecule, determined by the fundamental vibrational or rotational mode of the latter. [41] Due to an energy exchange process, the incoming photon with energy $h\nu_L$ is shifted in energy by the characteristic energy of vibration $h\nu_m$. These shifts can be in positive or negative, depending on whether the molecule is in its vibrational ground state or in an excited state. In the first case, the incident photon loses energy due to the excitation of a vibrational mode (Stokes scattering). In the second case, the incident photon gains additional energy due to the de-excitation of such vibrational mode (anti Stokes scattering).

The frequencies of these two Raman bands are $h(v_L - v_m)$ and $h(v_L + v_m)$, respectively. Raman and Rayleigh scattering are illustrated in **Figure 1.6**.

Over the years, the research has been focused on the characterization of the TMDS semiconductors and metals through this technique.
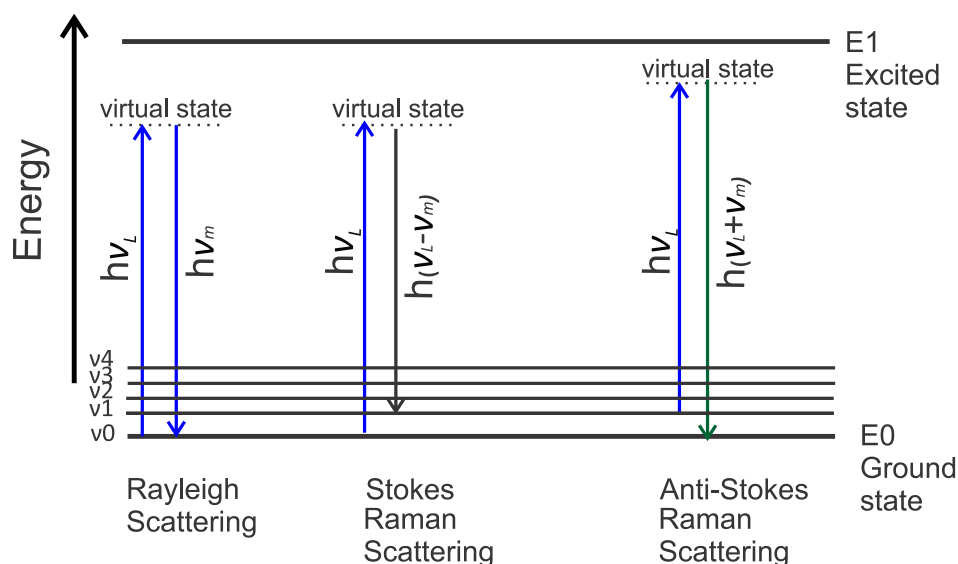
Figure 1.6 Raman and Rayleigh scattering depicting virtual states and ground states.

Diffraction Limit on Optical Spectroscopy

Lateral spatial resolution has been limited by diffraction. For the first time, in 1873, Ernst Abbe explained his theory and developed a formula for the diffraction limit in a microscope. [42] The equation estimates the smallest optical distance Δx between two objects (Airy discs) that can be observed while performing an optical measurement. In 1896, Lord Rayleigh [43] developed the Rayleigh criterion shown in **equation 1.1**, [42] which was a refined formula based on Abbe's diffraction limit. The calculated distance is directly proportional to the incident wavelength λ and inversely proportional to refractive index n of the medium and the angle α_r. The refractive index and angle are directly related to the microscope objective being used and defined by its numerical aperture ($N.A. = n.\sin(\alpha_r)$).

$$\Delta x = \frac{1.22\lambda}{2n \sin \alpha_r} \qquad (1.1)$$

Therefore, to achieve the best spatial resolution in a microscopy experiment, the optical components should have the larger N.A, short wavelength and optimized optical alignment. For years, researchers have tried to go beyond the mentioned diffraction limit, confocal Raman spectrometers is one of those developments that achieves better spatial and spectral resolution.

1.4.2   Atomic Force Microscopy

AFM is a topographical technique that can achieve atomic spatial resolution and has proved to be a key technique to probe the topography of surfaces with extreme resolution in the x, y, z directions. [44] Since its development in 1986 by Binnig and Rohrer,[45] AFM technique has been used to determine topography and mechanical properties in the biological, chemistry and physics fields. Binnig and Rohrer initially used a gold foil as a cantilever with an attached diamond tip to perform the experiments as, compared with the modern cantilevers which are usually made of Si, SiO_2 or Si_3N_4. AFM relies on the repulsive and attractive forces between the tip and the sample which generates a deflection upon the cantilever. The effect of the repulsive and attractive interactions are explained by the Lennard-Jones potential and is one of the main concepts required to understand the different modes of the AFM. [46] The operation of the AFM is based on three principle modes such as contact mode, dynamic mode also known as tapping mode, and non-contact mode. In contact mode the tip usually is in contact with the surface (0.5 nm separation), by the help of a piezoelectric scanner. This mode can produce a distortion on the image if lateral forces are applied and can reduce the spatial resolution by causing damage to the apex of the tip over time. In the dynamic mode, also known as semi-contact, tapping mode or intermittent contact, the cantilever oscillates at its resonance frequency with an amplitude between 20 to 100 nm and while the tip hovers above the surface. Finally, in the non-contact mode, the cantilever vibrates at a particular frequency a few nanometers above the sample. Changes in the frequency help to image the structure surface. [47] **Figure 1.7a-c** illustrates the three modes discussed.
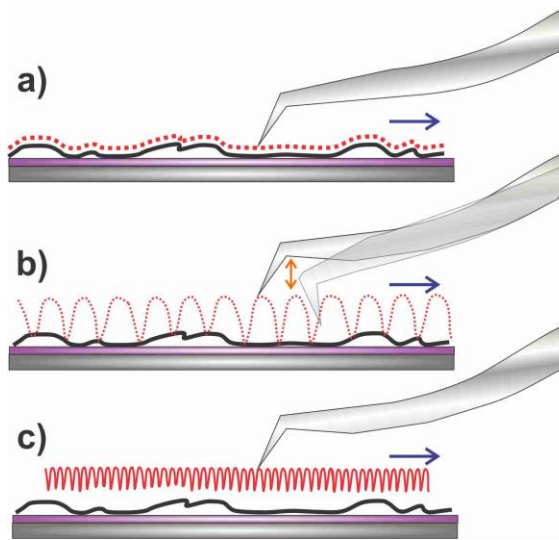
Figure 1.7 Different AFM modes a) contact b) tapping and c) non-contact.

1.4.3 Kelvin Probe Force Microscopy (KPFM)

KPFM was first introduced by Nonnenmacher in 1991, [48] and it measures the contact potential difference (CPD) between a conductive AFM tip and the sample. It maps the work function or surface potential with a high spatial resolution, and it has been used extensively to determine the electrical properties of semiconductors and metal interfaces.

KPFM determines and maps CPD defined by **equation 1.2**, [49] where Φ_{tip} and Φ_{sample} represent the work function of the tip and the sample, respectively, and e is the electronic charge.

$$V_{CPD} = \frac{(\Phi_{tip} - \Phi_{sample})}{e} \tag{1.2}$$

When a conductive tip is brought close to the sample surface, an electrical force is generated between the tip and sample surface due to the difference in their Fermi energy levels. [49]

1.4.4　Tip-Enhanced Raman Spectroscopy (TERS)

The main disadvantage of Raman Spectroscopy is that its inelastic scattering is 1000 times weaker than Rayleigh scattering (process that occurs in Infrared Spectroscopy). In 1974, Fleischman et al., [50] reported a large Raman signal absorbed in a roughened silver electrode providing for the first time a push towards an improvement of the weak Raman effect. Furthermore in 1977 two independent groups proposed a mechanism to boost the Raman effect known as Surface Enhanced Raman scattering (SERS). SERS is based on the electromagnetic and chemical theories. In 1985, Wessel suggested extending the SERS technology to the scanning probe microscopy by replacing the substrate with a metallic tip to be scanned over a sample. Thanks to the contributions of Zenobi, [51] Anderson[52] and Kawata[53] in 2000, the technique became known as TERS.

TERS combines the nanometer resolution of an AFM in combination with chemical sensitivity of a Raman Spectrometer. When both systems are coupled it generates an optical near-field enhancement by externally focusing a laser on the AFM tip to excite a surface plasmon and generating a LSPR at the vicinity of the tip's apex and the sample. Under best experimental and resonance conditions, TERS signal can be greatly enhanced. The gain is determined by the impinging laser wavelength, energy and polarization, and the tip material and geometry (permittivity, conductivity, radius, length). **Figure 1.8a-d** shows different TERS illumination setups. Furthermore, combines two techniques one topographical and another optical spectroscopical, which will be discussed in Chapter 2. Since LSPR is being generated at the tip's apex vicinity, the tip works as a nanoantenna as observed in **Figure 1.8e**. Raman signal can be furthered enhanced when a metallic surface is used as a substrate between the sample and the nanoantenna generating a "virtual metal dimer", [54] also referred as the gap mode as depicted in **Figure 1.8f**.
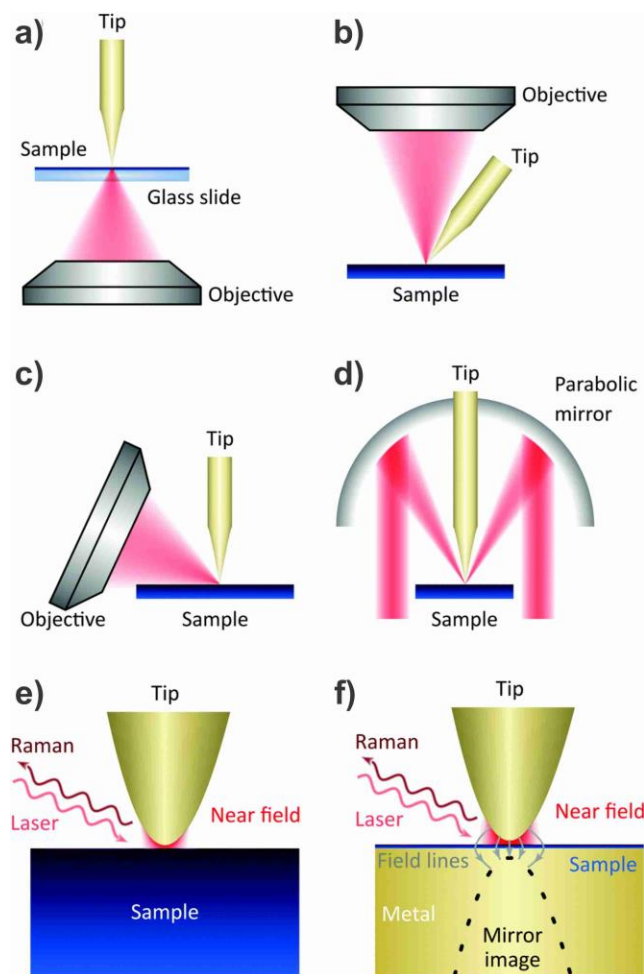
Figure 1.8 a) TERS with bottom illumination, b) top illumination, c) side illumination d) parabolic mirror geometries setups. Schematic of TERS process in e) bulk materials and f) gap-mode. Reproduced from Ref. [54] with permission from the Royal Society of Chemistry.

In optical near-field, the enhancement of the Raman signal from analyte molecules is proportional to the fourth power of the local electric field, as stated by **equation 1.3**. [55] where ρ is the Raman signal enhancement and $\mathbf{E}_{NF}$, $\boldsymbol{E}_{FF}$ is the near and far-field electric field, respectively.

$$\rho = \left(\frac{\mathbf{E}_{NF}}{\boldsymbol{E}_{FF}}\right)^{4} \tag{1.3}$$

Therefore, an enhancement factor (E_F) in TERS is calculated by **equation 1.4**.[55]

$$E_F = \left(\frac{I_{NF}}{I_{FF}} - 1\right)\frac{A_{FF}}{A_{NF}} \qquad (1.4)$$

Where I_{NF} and I_{FF} represent the spectral intensities of near-field and far field, respectively. A_{FF} is the diffraction limited far-field represented by the beam size of the laser beam and A_{NF} represents the near-field area of the hot-spot confined at the extremity of the AFM tip. The term $\left(\frac{I_{NF}-I_{FF}}{I_{FF}} = \frac{I_{NF}}{I_{FF}} - 1\right)$, is referred as enhancement contrast. It represents the increase of the signal in near-field conditions (tip is close to the surface) as compared to the far-field signal (tip away from the surface). The ratio $\frac{A_{FF}}{A_{NF}}$ is a normalization coefficient that considers the illuminated surfaces below the tip (A_{NF}) or in the absence of the tip (A_{FF}).

The improved results obtained through TERS resulted that in recent years there has been an increase in characterizations of TMDs. [56, 57]

1.5 Scope of Thesis

Applications of 1D and 2D materials are numerous in fields ranging from the semiconducting industry to biomedical imaging. Discovery and synthesis of new 1D and 2D materials yield to continuous discoveries in this field but the precise characterization of these materials is necessary using instrumentation that provide information beyond the physical characterization. The use of plasmonics is therefore of interest because it allows the identification of defects and strains on the surface of the materials producing alteration of their electronic and chemical properties. In the present thesis, high spatial resolution spectroscopy technique such as TERS, AFM and KPFM are applied to characterize the surface morphology and chemical composition of 1D and 2D materials. This manuscript is composed as follows: After a general introduction in Chapter 1, Chapter 2 provides the experimental methods necessary to understand the collected data on a variety of materials that are discussed in the subsequent chapters. Chapter 3 explains the first experimental

results of 1D and 2D carbon materials study through TERS combined with an artificial neural network (ANN) application for a reliable characterization of a large dataset of collected Raman spectra. In Chapter 4, the synthesis and characterization of vanadium disulfide using TERS is described. Additionally, a subsection of this chapter presents a discussion about the synthesis of rippled VS_2 and how the electronic properties are affected. This section includes TERS and KPFM characterization of VS_2. Chapter 5 focusses on the photoinduced oxidation of vanadium disulfide into various oxides using confocal Raman and TERS. Finally, Chapter 6 introduces semiconductive WS_2 and how hidden features at its surface can be revealed using TERS and Kelvin probe microscopy. Chapter 7 concludes on future work such as the synthesis and characterization of 2D heterostructure composed of TMDs and how nanoscale measurements are key to provide critical information on nanoscale materials.

1.6 References

(1) Iijima, S. Helical Microtubules of Graphitic Carbon. *Nature* **1991**, *354* (6348), 56-58.

(2) Novoselov, K. S.; Geim, A. K.; Morozov, S. V.; Jiang, D.; Katsnelson, M. I.; Grigorieva, I. V.; Dubonos, S. V.; Firsov, A. A. Two-Dimensional Gas of Massless Dirac Fermions in Graphene. *Nature* **2005**, *438* (7065), 197-200.

(3) Bashir, S.; Liu, J. Chapter 1 - Nanomaterials and Their Application. In *Advanced Nanomaterials and their Applications in Renewable Energy*, Liu, J. L., Bashir, S. Eds.; Elsevier, 2015; 1-50.

(4) Li, X.; Wang, J. One-Dimensional and Two-Dimensional Synergized Nanostructures for High-Performing Energy Storage and Conversion. *InfoMat* **2020**, *2* (1), 3-32.

(5) Sun, H.; Li, H.; You, X.; Yang, Z.; Deng, J.; Qiu, L.; Peng, H. Quasi-Solid-State, Coaxial, Fiber-Shaped Dye-Sensitized Solar Cells. *J. Mater. Chem. A* **2014**, *2* (2), 345-349.

(6) Lee, H. Y.; Kim, S. Nanowires for 2D Material-Based Photonic and Optoelectronic Devices. *Nanophotonics* **2022**, *11* (11), 2571-2582.

(7) Li, H.; Shi, Y.; Chiu, M.-H.; Li, L.-J. Emerging Energy Applications of Two-Dimensional Layered Transition Metal Dichalcogenides. *Nano Energy* **2015**, *18*, 293-305.

(8) Machín, A.; Fontánez, K.; Arango, J. C.; Ortiz, D.; De León, J.; Pinilla, S.; Nicolosi, V.; Petrescu, F. I.; Morant, C.; Márquez, F. One-Dimensional (1D) Nanostructured Materials for Energy Applications. *Materials* **2021**, *14* (10), 2609.

(9) Atanassova, M. Naming of Chemical Elements. *Bulg. J. Sci. Educ* **2015**, *24*, 125-137.

(10) Iijima, S.; Ichihashi, T. Single-Shell Carbon Nanotubes of 1-nm Diameter. *Nature* **1993**, *363* (6430), 603-605.

(11) Charlier, J. C. Defects in Carbon Nanotubes. *Accounts Chem. Res.* **2002**, *35* (12), 1063-1069.

(12) Weisman, R. B.; Kono, J. *Handbook Of Carbon Nanomaterials (Volumes 9-10)*; World Scientific, 2019.

(13) Singh, A. K.; Kumbhakar, P.; Krishnamoorthy, A.; Nakano, A.; Sadasivuni, K. K.; Vashishta, P.; Roy, A. K.; Kochat, V.; Tiwary, C. S. Review of Strategies Toward the Development of Alloy Two-Dimensional (2D) Transition Metal Dichalcogenides. *iScience* **2021**, *24* (12), 103532.

(14) Coogan, Á.; Gun'ko, Y. K. Solution-Based "Bottom-Up" Synthesis of Group VI Transition metal Dichalcogenides and Their Applications. *Mater. Adv.* **2021**, *2* (1), 146-164.

(15) Li, W.; Kheimeh Sari, H. M.; Li, X. Emerging Layered Metallic Vanadium Disulfide for Rechargeable Metal-Ion Batteries: Progress and Opportunities. *ChemSusChem* **2020**, *13* (6), 1172-1202.

(16) He, P.; Yan, M.; Zhang, G.; Sun, R.; Chen, L.; An, Q.; Mai, L. Layered VS$_2$ Nanosheet-Based Aqueous Zn Ion Battery Cathode. *Adv. Energy Mater.* **2017**, *7* (11), 1601920.

(17) Jing, Y.; Zhou, Z.; Cabrera, C. R.; Chen, Z. Metallic VS$_2$ Monolayer: A Promising 2D Anode Material for Lithium Ion Batteries. *J. Phys. Chem. C* **2013**, *117* (48), 25409-25413.

(18) Littlejohn, A. J.; Li, Z.; Lu, Z.; Sun, X.; Nawarat, P.; Wang, Y.; Li, Y.; Wang, T.; Chen, Y.; Zhang, L.; et al. Large Metallic Vanadium Disulfide Ultrathin Flakes for Spintronic Circuits and Quantum Computing Devices. *ACS Appl. Nano Mater.* **2019**, *2* (6), 3684-3694.

(19) Guo, Z.; Yang, L.; Wang, W.; Cao, L.; Dong, B. Ultrathin VS$_2$ Nanoplate With In-Plane and Out-of-Plane Defects for An Electrochemical Supercapacitor With Ultrahigh Specific Capacitance. *J. Mater. Chem. A* **2018**, *6* (30), 14681-14688.

(20) Feng, J.; Sun, X.; Wu, C.; Peng, L.; Lin, C.; Hu, S.; Yang, J.; Xie, Y. Metallic Few-Layered VS$_2$ Ultrathin Nanosheets: High Two-Dimensional Conductivity for In-Plane Supercapacitors. *J. Am. Chem. Soc.* **2011**, *133* (44), 17832-17838.

(21) Huang, L.; Zhu, W.; Zhang, W.; Chen, K.; Wang, J.; Wang, R.; Yang, Q.; Hu, N.; Suo, Y.; Wang, J. Layered Vanadium(IV) Disulfide Nanosheets as a Peroxidase-Like Nanozyme for Colorimetric Detection of Glucose. *Microchim. Acta* **2017**, *185* (1), 7.

(22) Yuan, J.; Wu, J.; Hardy, W. J.; Loya, P.; Lou, M.; Yang, Y.; Najmaei, S.; Jiang, M.; Qin, F.; Keyshar, K.; et al. Facile Synthesis of Single Crystal Vanadium Disulfide Nanosheets by Chemical Vapor Deposition for Efficient Hydrogen Evolution Reaction. *Adv. Mater.* **2015**, *27* (37), 5605-5609.

(23) Ji, Q.; Li, C.; Wang, J.; Niu, J.; Gong, Y.; Zhang, Z.; Fang, Q.; Zhang, Y.; Shi, J.; Liao, L.; et al. Metallic Vanadium Disulfide Nanosheets as a Platform Material for Multifunctional Electrode Applications. *Nano Lett.* **2017**, *17* (8), 4908-4916.

(24) Zhang, S.; Chang, P.; Zhang, Y.; Xu, X.; Guan, L.; Tao, J. Effect of Morphology and Stacking on Atomic Interaction and Magnetic Characteristics in Two-Dimensional H-Phase VS$_2$ Few Layers. *J. Mater. Sci.* **2022**, *57* (10), 5873-5884.

(25) Hossain, M.; Qin, B.; Sen, S. K. Chemical Synthesis and Substrate Temperature Effect on Morphology of 2D Vanadium Disulfide. *Cryst. Res. Technol.* **2021**, *56* (3), 2000184.

(26) Ding, J.; Feng, A.; Li, X.; Ding, S.; Liu, L.; Ren, W. Properties, Preparation, and Application of Tungsten Disulfide: A Review. *J. Phys. D. Appl. Phys.* **2021**, *54* (17), 173002.

(27) Ambrosi, A.; Sofer, Z.; Pumera, M. 2H → 1T Phase Transition and Hydrogen Evolution Activity of MoS$_2$, MoSe$_2$, WS$_2$ and WSe$_2$ Strongly Depends on the MX2 Composition. *Chem. Commun.* **2015**, *51* (40), 8450-8453.

(28) Zhao, Y.; Zhang, C.; Kohler, D. D.; Scheeler, J. M.; Wright, J. C.; Voyles, P. M.; Jin, S. Supertwisted Spirals of Layered Materials Enabled by Growth on Non-Euclidean Surfaces. *Science* **2020**, *370* (6515), 442-445.

(29) Perrozzi, F.; Emamjomeh, S. M.; Paolucci, V.; Taglieri, G.; Ottaviano, L.; Cantalini, C. Thermal Stability of WS$_2$ Flakes and Gas Sensing Properties of WS$_2$/WO$_3$ Composite to H$_2$, NH$_3$ and NO$_2$. *Sensor Actuat. B-Chem.* **2017**, *243*, 812-822.

(30) Zhang, W.; Huang, Z.; Zhang, W.; Li, Y. Two-Dimensional Semiconductors with Possible High Room Temperature Mobility. *Nano Res.* **2014**, *7* (12), 1731-1737.

(31) Fan, Y.; Zhou, Y.; Wang, X.; Tan, H.; Rong, Y.; Warner, J. H. Photoinduced Schottky Barrier Lowering in 2D Monolayer WS$_2$ Photodetectors. *Adv. Opt. Mater.* **2016**, *4* (10), 1573-1581.

(32) Radha, S. K.; Crowley, K.; Holler, B. A.; Gao, X. P. A.; Lambrecht, W. R. L.; Volkova, H.; Berger, M.-H.; Pentzer, E.; Pachuta, K. G.; Sehirlioglu, A. Ultrathin 2D-

Oxides: A Perspective On Fabrication, Structure, Defect, Transport, Electron, and Phonon Properties. *J. Appl. Phys.* **2021**, *129* (22), 220903.

(33) Zhang, R.; Fu, Q. S.; Yin, C. Y.; Li, C. L.; Chen, X. H.; Qian, G. Y.; Lu, C. L.; Yuan, S. L.; Zhao, X. J.; Tao, H. Z. Understanding of Metal-Insulator Transition in VO_2 Based on Experimental and Theoretical Investigations of Magnetic Features. *Sci. Rep.-UK* **2018**, *8* (1), 17093.

(34) Shvets, P.; Dikaya, O.; Maksimova, K.; Goikhman, A. A Review of Raman Spectroscopy of Vanadium Oxides. *J. Raman Spectrosc.* **2019**, *50* (8), 1226-1244.

(35) Chernova, N. A.; Roppolo, M.; Dillon, A. C.; Whittingham, M. S. Layered Vanadium and Molybdenum Oxides: Batteries and Electrochromics. *J. Mater. Chem.* **2009**, *19* (17), 2526-2552.

(36) Zaki, S. E.; Basyooni, M. A.; Shaban, M.; Rabia, M.; Eker, Y. R.; Attia, G. F.; Yilmaz, M.; Ahmed, A. M. Role of Oxygen Vacancies in Vanadium Oxide and Oxygen Functional Groups in Graphene Oxide for Room Temperature CO2 Gas Sensors. *Sensor Actuat. A.-Phys.* **2019**, *294*, 17-24.

(37) Castellanos-Gomez, A. Why all the fuss about 2D semiconductors? *Nat. Photonics* **2016**, *10* (4), 202-204.

(38) Museum, T. B. *Drinking-cup*. The British Museum, accessed 2022.

(39) Pines, D.; Bohm, D. A Collective Description of Electron Interactions: II. Collective vs. Individual Particle Aspects of the Interactions. *Phys. Rev.* **1952**, *85* (2), 338-353.

(40) Cao, E.; Lin, W.; Sun, M.; Liang, W.; Song, Y. Exciton-Plasmon Coupling Interactions: From Principle to Applications. *Nanophotonics* **2018**, *7* (1), 145-167.

(41) Maier, S. A. *Plasmonics: Fundamentals and Applications*; Springer, **2007**.

(42) Novotny, L. From near-field optics to optical antennas. *Phys.Today* **2011**, *64*.

(43) Rayleigh. XV. On the theory of optical images, with special reference to the microscope. *Lond. Edinb. Dublin Philos. Mag. J. Sci.* **1896**, *42* (255), 167-195.

(44) Zhang, H.; Huang, J.; Wang, Y.; Liu, R.; Huai, X.; Jiang, J.; Anfuso, C. Atomic Force Microscopy for Two-Dimensional Materials: A Tutorial Review. *Opt. Commun.* **2018**, *406*, 3-17.

(45) Binnig, G.; Quate, C. F.; Gerber, C. Atomic Force Microscope. *Phys. Rev. Lett.* **1986**, *56* (9), 930-933.

(46) Seo, Y.; Jhe, W. Atomic Force Microscopy and Spectroscopy. *Rep. Prog. Phys.* **2007**, *71* (1), 016101.

(47) Rana, M. S.; Pota, H. R.; Petersen, I. R. Improvement in the Imaging Performance of Atomic Force Microscopy: A Survey. *IEEE T. Autom. Sci. Eng.* **2017**, *14* (2), 1265-1285.

(48) Nonnenmacher, M.; O'Boyle, M. P.; Wickramasinghe, H. K. Kelvin Probe Force Microscopy. *Appl. Phys. Lett.* **1991**, *58* (25), 2921-2923.

(49) Melitz, W.; Shen, J.; Kummel, A. C.; Lee, S. Kelvin Probe Force Microscopy and Its Application. *Surf. Sci. Rep.* **2011**, *66* (1), 1-27.

(50) Fleischmann, M.; Hendra, P. J.; McQuillan, A. J. Raman Spectra of Pyridine Adsorbed At A Silver Electrode. *Chem. Phys. Lett.* **1974**, *26* (2), 163-166.

(51) Stöckle, R. M.; Suh, Y. D.; Deckert, V.; Zenobi, R. Nanoscale Chemical Analysis by Tip-Enhanced Raman Spectroscopy. *Chem. Phys. Lett.* **2000**, *318* (1), 131-136.

(52) Anderson, M. S. Locally Enhanced Raman Spectroscopy With An Atomic Force Microscope. *Appl. Phys. Lett.* **2000**, *76* (21), 3130-3132.

(53) Hayazawa, N.; Inouye, Y.; Sekkat, Z.; Kawata, S. Metallized Tip Amplification of Near-Field Raman Scattering. *Opt. Commun.* **2000**, *183* (1), 333-336.

(54) Kolhatkar, G.; Plathier, J.; Ruediger, A. Nanoscale Investigation of Materials, Chemical Reactions, and Biological Systems By Tip Enhanced Raman Spectroscopy – A Review. *J. Mater. Chem. C* **2018**, *6* (6), 1307-1319.

(55) Kumar, N.; Mignuzzi, S.; Su, W.; Roy, D. Tip-Enhanced Raman Spectroscopy: Principles and Applications. *EPJ Tech. Instrum.* **2015**, *2* (1), 9.

(56) Darlington, T. P.; Carmesin, C.; Florian, M.; Yanev, E.; Ajayi, O.; Ardelean, J.; Rhodes, D. A.; Ghiotto, A.; Krayev, A.; Watanabe, K.; et al. Imaging Strain-Localized Excitons in Nanoscale Bubbles of Monolayer WSe2 At Room Temperature. *Nat. Nanotechnol.* **2020**, *15* (10), 854-860.

(57) Farhat, P.; Avilés, M. O.; Legge, S.; Wang, Z.; Sham, T.-K.; Lagugné-Labarthet, F. Tip-Enhanced Raman Spectroscopy and Tip-Enhanced Photoluminescence of MoS2 Flakes Decorated with Gold Nanoparticles. *J. Phys. Chem. C* **2022**, *126* (16), 7086-7095.

Chapter 2

2   Experimental Methods

This chapter describes the methods and preparation associated with the different materials studied in this thesis.

2.1.1   Preparation of Gold Substrates

Gold substrates were prepared either by template stripping or electron-beam (e-beam) evaporation. Template stripped substrates provide ultra-flat surfaces with lower root-mean-squared (rms) roughness as compared to thin films prepared by e-beam. Typically, the roughness of the film is less than 1 nm for template stripping meanwhile films prepared by e-beam yield roughness in the 2-4 nm range. A smooth surface is necessary to provide excellent contrast for very small objects deposited at its surface.[1] Furthermore gold substrate is specifically important for tip-enhanced measurements to provide ideal condition to confine the incident electromagnetic field in gap-mode experiments. Films prepared by electron beam evaporation were using an adhesion layer of 5 nm Ti adhesion layer and 30 nm Au layer subsequently deposited. Template stripped substrates were prepared by depositing 100 nm of gold on a Si wafer without any adhesion layer, followed by the application of UV glue onto a 1×1 cm^2 piece of glass cover slip (100 µm thick). The cut substates were glued, onto the gold wafer and cured using a UV lamp during 5-10 min. The layers were then glued and stripped using a very sharp cleaned razor blade to generate smooth surfaces. **Figure 2.1** shows the difference between both methods. It is observed large topography changes and quantified with the rms roughness.
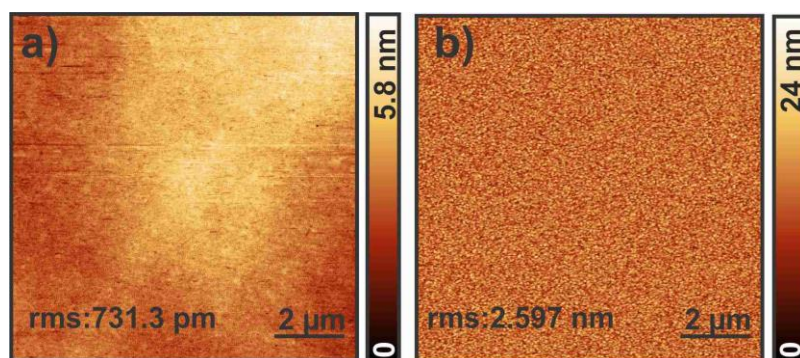
Figure 2.1 AFM scans of gold substrates prepared by a) template stripped method, b) e-beam deposition.

It must be mentioned that template stripped substrates were used for the preparation of graphene and CNTs in Chapter 3. E-beam deposited substrates were used in the experimental work described in Chapter 4 and 5. Template stripped is not suitable, since it uses either epoxy or UV resin for which the transferring procedure requires the use of strong solvents as acetone which appeared to damage the Au film.

2.1.2 Preparation of Graphene Sheets

Graphene sheets immersed in ethanol were acquired from KWI Polymers Solutions company. Solution was sonicated for 30 minutes and centrifuged at 1400 rpm for 20 minutes in order to exfoliate the sheets that were aggregated. Zonal Centrifugation method using differential separation was followed to obtain a rough distribution of flakes, [2] this method helps size sorting of large flakes of graphene. Finally, we proceeded to drop-cast around 10-20 µL of solution over the template stripped Au substrate and left the sample dry overnight.

2.1.3 Preparation of SWNT

Figure 2.2a,b shows the compounds used to prepare the metallic and semiconductive carbon nanotubes. Metallic SWNTs with 0.03 mg mL^{-1} (Nanointegris Isonanotubes-M 99% Solution) was sonicated for 2 minutes and centrifugated prior to be drop-casted onto a template stripped gold substrate. Metallic SWNTs varied in diameter between 1.2–1.7

nm. Additionally, the semiconductive SWNT solution (Nanointegris HiPco purified) shown in **Figure 2.2b** was prepared with 0.5 mg mL^{-1} in 1% sodium dodecyl sulfate (SDS), sonicated for 1 hour and 20 minutes, and then centrifuged for 1 hour at 1500 rpm. The semiconductive SWNTs were drop-casted, as prepared, into a template stripped gold substrate. After 24 hours of drying, to remove the surfactant, water with acetic acid (0.1% v/v) was used to rinse the substrate with SWNTs.
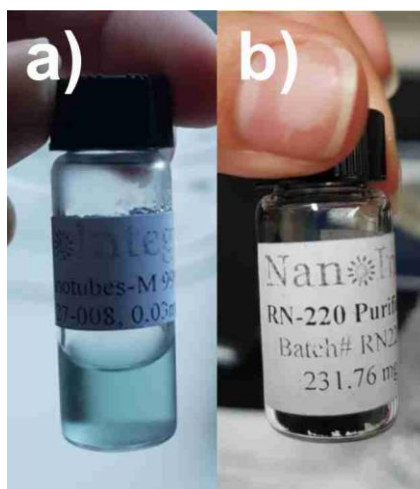
Figure 2.2. a) SWNTs NanoIntegris Isonanotubes on solution metallic. b) SWNTs Nanointegris HiPCo purified powder semiconductive.

2.1.4   Chemical Vapor Deposition (CVD)

Chemical vapor deposition (CVD) is a vapor transport synthesis technique. In this process, a gaseous precursor is formed upon heating and deposits onto a heated substrate to form a film or a flake.[3] The substrate, temperature, composition of the reaction mixture, gas total pressure, and ratio of the materials used are critical experimental parameters and alter the morphology, composition, and subsequent properties of grown material.[4] CVD has the advantage over exfoliation to produce high purity crystals and solid-state materials. In this thesis various transition metal dichalcogenides semiconductive, metallic and oxides including VS_2, VO_2, and WS_2 were synthesized through this method. The single zones

furnaces Lindberg/Blue M 1500°C and Lindberg Blue Mini-mite were used for the synthesis of different compounds (**Figure 2.3a,b**).

Figure 2.3. a) Lindberg/Blue M 1500°C single zone furnace. b) Lindberg Blue Mini-mite 1100°C single zone furnace.

VS$_2$

VS$_2$ was grown using a Lindberg Blue Mini-Mite single zone tube furnace equipped with a 1" fused quartz tube. The sulfur (180 mg, Millipore Sigma powder 99.98 % purity) was placed in an alumina boat stream upwards, close to the inlet of the carrier gas, followed by 35 mg VCl$_3$ precursor (Alfa Aesar powder 99% purity) located approximately 9 cm away stream downwards. At the center of the furnace approximately 20 cm away from the sulfur precursor, freshy cleaved fluorophlogopite mica (referred as mica afterwards) substrates (MIT corp., size 8 mm × 8 mm × 0.2 mm) were strategically located. The quartz tube was purged with argon at 400 sccm for 30 min to eliminate any oxygen residue in the chamber. Subsequently, the argon flow rate is reduced to 80 sccm and hydrogen gas is introduced at a mass flow rate of 20 sccm. The ramping was started after additional 5 min, to stabilize the gas concentration and flow rate. The temperature was changed from room temperature (22 °C) to 650 °C with a heating rate of 20 °C/min. For the generation of ripples over the surface or defects, the whole furnace was shifted by 1.5 cm stream upwards (in the direction of the sulfur precursor) right before reaching 630°C. Afterwards, the temperature setpoint remained at 650°C for 15 min and then cooled down to room temperature under 80 sccm of argon flow only. The samples were immediately characterized and stored in argon atmosphere to prevent oxidation. To avoid generation of ripples or defects a Niobium round

magnet was used to push the boat S precursor slowly into the heating zone once the thermocouple was marking the melting point of the VCl_3 precursor.

VO₂, V₂O₅

For vanadium oxides, a salt assisted method was used in which the V_2O_5 (Alfa, 99.2%) and KI or KCl (Sigma, 99.99%) precursors were mixed and placed in the center of an alumina (Al_2O_3) boat positioned at the central part of the Lindberg/Blue M 1500 °C furnace. Fluorphlogopite mica substrate, were located one on the top and one at 6 cm away downstream of the center of the crucible boat for the deposition of flakes. Another boat, positioned upstream 27 cm from the center of the furnace, contained sulphur. Prior to the synthesis procedure, the system was purged with 100 sccm of argon for 30 min. Once the furnace was started, the inside temperature level increased from 20 to 730 ℃ with a heating rate of 50 ℃/min, under 50 sccm of Ar and 10 sccm of H_2. After the indicated steps were accomplished, the hydrogen gas flow was shut off and the argon was left flowing at 20 sccm while the furnace was cooling down. As soon as the quartz tube reached 60 ℃, it was opened to remove the samples for their immediate characterization.

WS₂

The WS_2 was synthesized using WO_3 (Alfa Aesar, 99.8%) as the tungsten source using the single zone furnace Lindberg Blue Mini-Mite and Ar was used as the carrier gas. The sulfur (180 mg, Sigma Aldrich 99.9%) was placed in an alumina boat initially outside the hot zone of the furnace. A small iron screw was installed in front of the boat to externally change the position of the boat with the help of a magnet. The WO_3 (30 mg) was positioned in an alumina boat in the center of the furnace. The Si substrate with a 280 nm SiO_2 layer was placed 6 cm from the WO_3 boat stream downwards. The system got purged for 40 min with a flow rate of 400 sccm. Afterwards the flow rate was switched to 200 sccm. During the experiment, the temperature was increased during the experiment from room temperature to 750 °C with a heating rate of 12 °C/min and from 750 °C to 860 °C with a heating rate of 6.0 °C/min. At 570 °C the sulfur boat was displaced towards the edge of the furnace, in such a way that the sulfur slowly starts to melt. The distance between the sulfur

and WO₃ boat was reduced to 24 cm. Due to the temperature gradient existent within the furnace, the temperature of the substrate becomes lower than that of WO₃. During the cooling period to room temperature the flow rate was changed to 100 sccm.

2.1.5   Transferring Method

The different characterization techniques required the need of a conductive substrate, such as a gold thin film, meanwhile the TMD flakes were grown in SiO_2/Si or mica substrates. Polymethyl methacrylate (PMMA) method was exploited to transfer the flakes grown over SiO_2/Si and mica substrates to a deposited TiAu (5/30 nm) thin film prepared by e-beam evaporation. PMMA method consisted of dissolving 50 mg of PMMA in 600 µL of Chloroform. 20 µL of this solution was spin coated on the substrate with the TMD flakes at1600 rpm creating a transparent thin layer. The substrate was baked at 150°C for 5 minutes to cure the film. The sample was then submerged in DI during 10 min. After 10 min the film detached from the substrate with the help of soft sonication. PMMA film onto which the flakes were attached, was scooped out onto gold-coated substrate. The excess DI water on the PMMA film was left to dry and then baked at 60°C for 2 minutes maximum. Samples were left overnight in acetone to dissolve the PMMA layer. The different steps are summarized in **Figure 2.4.**
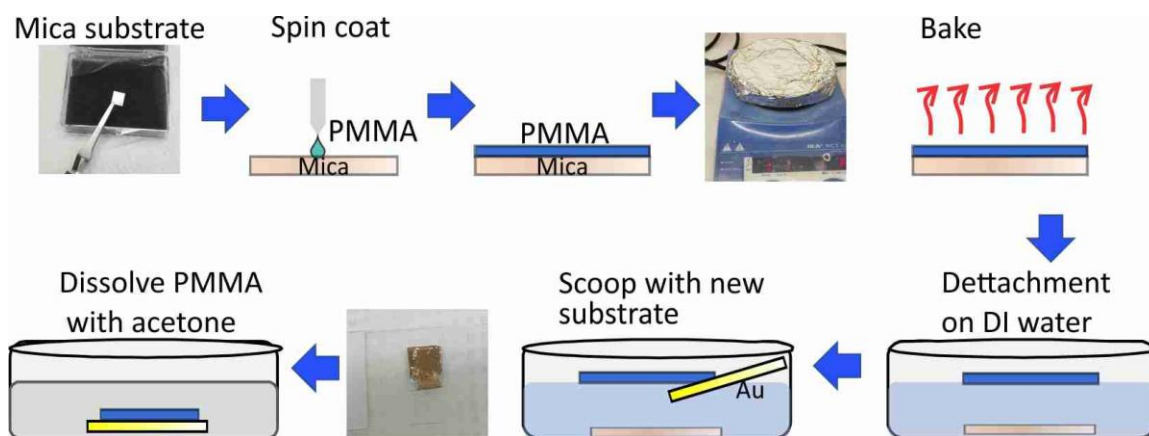
Figure 2.4. PMMA step by step transferring method.

2.2 Characterization Techniques

2.2.1 Confocal Raman Spectroscopy

An XploRa Plus Raman micro spectrometer from HORIBA Scientific was used in all our experiments (**Figure 2.5a,b)**.This compact confocal spectrometer integrates different excitation lasers, gratings, objectives, pinhole, white light source and a CCD camera. In this study 638 nm (red) and 532 nm (green) incident wavelength lasers were used. The gratings of 600, 1200 and 1800 grooves per mm were used in most experiments when high spectral resolution was needed optical micrographs and point spectra were acquired using an Olympus M plan N 100× with a 0.9 numerical aperture (N.A.). The pinhole and slit were generally set at 300 µm and 100 µm, respectively, unless stated otherwise. All measurements were conducted at room temperature.
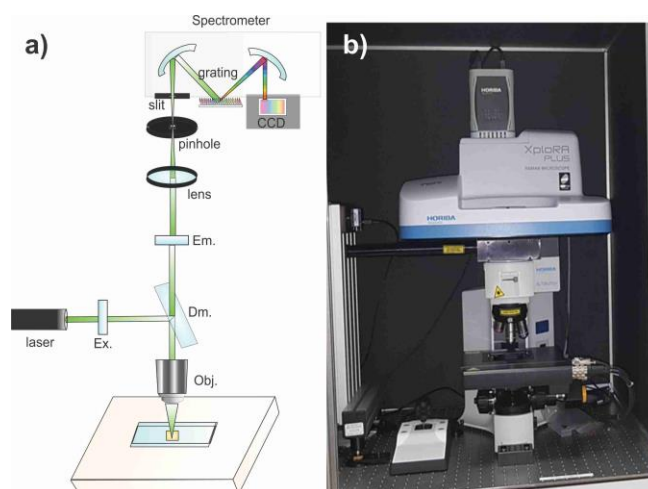
Figure 2.5 a) Sketch of the internal elements of the confocal spectrometer. b) Horiba XploRA Plus spectrometer.

Photoluminescence Spectroscopy (PL)

Photoluminescence occurs when upon incident excitation with light, the stimulated material emits photon with lower energy. As light impinges the material, absorption of this radiation yields to the formation of electron-hole pairs. This process causes electron to jump temporarily to a higher electronic state. Subsequently, the particle's energy is

released (photons) during a relaxation period returning to a lower or ground state vibrational energy level.

In inorganic materials studied in this work, lattices are connected through covalent bonds and the formation of electron-hole pairs produces a delocalization of electronic states in the form of a broad valence and conduction bands. There exist two types of PL emission referred as band-to-band or intrinsic and sub-bandgap or extrinsic emissions. Intrinsic emission PL occurs when excited electron falls back directly to the valence band whereas for the case of the extrinsic emission the excited electron is trapped by the defect center or impurity that occupies an energy level within the semiconductor bandgap. [5]

2.2.2   Atomic Force Microscopy (AFM)

Different AFMs were used in this thesis.

Measurements combined with TERS, and Kelvin Force microscopy (Chapters 3-6) were conducted using an AIST-NT OmegaScope instrument in tapping mode. Tapping mode probes NCLR from NanoWorld were used to acquire different scans. The length of the probes was approximately 225 µm, a resonance frequency of 190 kHz with a force constant of 48 N/m. The scan rate ranged from 0.5 to 1.2 Hz depending on the sample. Resolution was mostly kept at 300×300 pixels.

Nanomechanical measurements using (Chapter 6) intermittent contact mode and PeakForce Quantitative Nanomechanics (QNM) scans were conducted with a Bioscope Catalyst AFM using NCLR cantilevers and Bruker TAP525A probes depending on the nanomechanical measurements. The scan rate used ranged from 0.5 Hz for the intermittent contact mode to 0.3 Hz for the QNM measurements. The resolution was kept at 512×512 pixels for all measurements. Bruker TAP525A cantilever had a resonance frequency 525 kHz and a spring constant of 200 N/m.

Finally, AFM measurements using force modulation mode (FMM) measurements (Chapter 6) that were performed using Nanowizard II AFM (JPK), with Bruker OLTERPA-R3

probes. The cantilevers had a resonance frequency of 70 kHz, spring constant of 2 N/m and the scan rate of 0.3 Hz. FMM measurements exploit AC and DC signals, where DC signal gave the vertical and lateral deflection of the cantilever associated to the height and friction information. AC signal gives the phase and amplitude and extra information on mechanical properties such as young modulus and adhesion.

2.2.3   Kelvin Probe Force Microscopy (KPFM)

AIST-NT instrument with a conductive module was used for the KPFM measurements. For KPFM μMasch HQ:NSC14/Cr-Au probes were used that had a resonance frequency of about 160 kHz and a spring constant of 0.5N/m. CPD maps were obtained by varying the lift between the sample and the probe to generate a high-resolution map.

2.2.4   Tip-Enhanced Raman Spectroscopy (TERS)

OmegaScope atomic force microscope combined to an XploRA Raman micro spectrometer (HORIBA Scientific) equipped with a 600, and 1200 grooves per mm was used for the TERS acquisition. The setup has a fixed side illumination geometry (60° relative to a perpendicular line from the sample) for all experiments performed as illustrated in **Figure 2.6a,b.** Mitutoyo M Plan Apo objective of 100× with large working distance, 0.7 N.A in reflection, was used for both excitation and collection in backscattering geometry. Both 532 nm or 638nm were used in the TERS measurements in conjunction with silver and gold-coated tips, respectively.

Optical scattering was first performed to identify a hotspot at the apex of the tip for TERS enhancement. An AFM topography map was then recorded prior the TERS experiment to locate the structures of interest. The scan was obtained setting an oscillation amplitude of ~20 nm. The TERS spectra of all measurements were finally recorded in the Spec-Top mode, meaning that for each pixel one spectrum is acquired with the tip in direct contact with the surface. Between two pixels of the map the tip is moved in intermittent contact mode to prevent damage to the probe and to keep the plasmonic enhancement.

Chapter 3 explains the characterization of carbon based 1D and 2D materials using gold OMNI TERS NC probes purchased from HORIBA. These particular probes were coated with 60 nm of Au, spring constant of 93 N /m, and a resonance frequency of 320 kHz. Areas of maximum 100×100 pixels representing 10000 Raman spectra were recorded with a scanning rate of 1 Hz.

Chapters 4,5 and 6 explain characterization and synthesis of TMDs using Bruker VTESPA-300 probes with silver or gold homemade coating. For the silver coated case there was no adhesion layer added restricting the probes to be used within three days to avoid oxidation. For the gold tips, 15 nm of Ti was deposited and serves as an adhesion layer adding approximately 60 nm of Au. The tips from Bruker were intermittent contact cantilevers with a spring constant of 42 N/m, and a resonance frequency of 300 KHz.
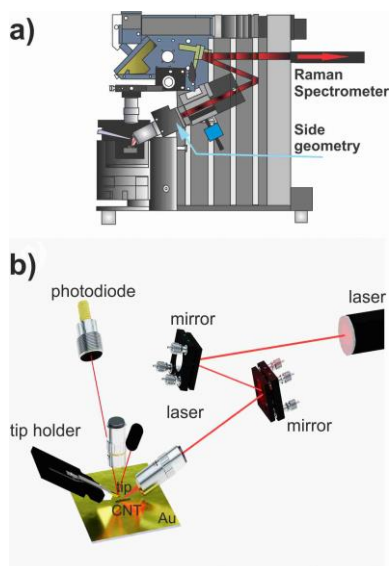
Figure 2.6 a) Complete sketch from OmniScope AIST-NT system reproduced from reference [6] from the Royal Society of Chemistry. b) Zoom in view of TERS setup with the sample and tip holder revealing a carbon nanotube sample in gap-mode where the CNT is sandwiched between a Au coated tip and a Au substrate.

2.2.5 Machine Learning: Artificial Neural Networks (ANN)

Machine Learning approach for data analysis began with Walter Pitts and neuroscientist Warren McCulloch in 1943, who developed a methodology using neural networks. [7] It relies on computational algorithms designed to emulate human intelligence by learning from a set of examples with features. One of the applications of ANN models has been to automate data analysis that outputs result promptly.

Part of the set of examples trains the model to recognize relevant features, patterns, and specific knowledge that in our case such served for a rapid characterization and analysis in vibrational spectroscopy. [8] In the past years, ANN has been very popular in the areas of biology, chemistry, and engineering to treat massive amounts of data. Generally, it consists of an input, hidden and output layers. Input data passes through hidden layers to perform mathematical calculations and passing such information to the following layers for optimization. The learning techniques can be unsupervised and supervised. We used supervised learning technique for the work reported in this thesis.

Chapter 3 describes the application of ANN in the TERS rapid identification and study of CNTs using TERS technique. Packages from the Python (version 3.7.3) data science software stack were exploited in the data pre-processing and feature engineering stages of a machine learning workflow. Pandas version 0.25.0, Matplotlib version 3.1.1, and NumPy version 1.17.0. Jupyter Notebook facilitated the construction of the architecture and topology of ANNs as well as the model training. Seaborn version 0.9.0 was used to create heat-maps and assess the correlation of native and derived features of the data set. When the highest accuracy value was reached, the ANN result data were exported from Jupyter Notebook to JSON or YAML format for input and reading files into a software that makes predictions using the machine learning model to create enhanced ANN generated hyperspectral maps. Processing an entire hyperspectral cube of 10000 TERS spectra took about 6 hours. [6]

2.3 References

(1) Vogel, N.; Zieleniecki, J.; Köper, I. As Flat As It Gets: Ultrasmooth Surfaces from Template-Stripping Procedures. *Nanoscale* **2012**, *4* (13), 3820-3832.

(2) Sun, X.; Luo, D.; Liu, J.; Evans, D. G. Monodisperse Chemically Modified Graphene Obtained by Density Gradient Ultracentrifugal Rate Separation. *ACS Nano* **2010**, *4* (6), 3381-3389.

(3) Hernandez Ruiz, K.; Wang, Z.; Ciprian, M.; Zhu, M.; Tu, R.; Zhang, L.; Luo, W.; Fan, Y.; Jiang, W. Chemical Vapor Deposition Mediated Phase Engineering for 2D Transition Metal Dichalcogenides: Strategies and Applications. *Small Science* **2022**, *2* (1), 2100047.

(4) Carlsson, J.-O.; Martin, P. M. Chapter 7 - Chemical Vapor Deposition. In *Handbook of Deposition Technologies for Films and Coatings (Third Edition)*, Martin, P. M. Ed.; William Andrew Publishing, 2010; 314-363.

(5) Tebyetekerwa, M.; Zhang, J.; Xu, Z.; Truong, T. N.; Yin, Z.; Lu, Y.; Ramakrishna, S.; Macdonald, D.; Nguyen, H. T. Mechanisms and Applications of Steady-State Photoluminescence Spectroscopy in Two-Dimensional Transition-Metal Dichalcogenides. *ACS Nano* **2020**, *14* (11), 14579-14604.

(6) Kajendirarajah, U.; Olivia Avilés, M.; Lagugné-Labarthet, F. Deciphering Tip-Enhanced Raman Imaging of Carbon Nanotubes with Deep Learning Neural Networks. *Phys. Chem. Chem. Phys.* **2020**, *22* (32), 17857-17866.

(7) Foote, K. D. The History of Machine Learning and Its Convergent Trajectory Towards AI. In *Machine Learning and the City*, 2022; 129-142.

(8) Lussier, F.; Thibault, V.; Charron, B.; Wallace, G. Q.; Masson, J.-F. Deep Learning and Artificial Intelligence Methods for Raman and Surface-Enhanced Raman Acattering. *Trends Analyt. Chem* **2020**, *124*, 115796.

Chapter 3

3   Carbon-Based 1D and 2D Materials and Their Study Through Tip-Enhanced Raman

Carbon-containing nanomaterials such as nanotubes, fullerenes or graphene are interesting from a pure physical and chemical viewpoint due to their exceptional electron and thermal conductivity and their mechanical properties. Even though many applications were though to use these nanomaterials for future nanoelectronics devices, they are mainly used in bulk quantities together with other elements. For example, graphene is one element used in modern batteries, it can control the speed over which the battery can be charged and discharged. Further applications include photovoltaics, sensors, lubricants, thermal management, and drug delivery. [1] Characterization of such materials at the individual level is necessary to determine its properties and requires instruments with high spatial resolution to probe individual defects, surface functionalization or interaction with other materials. In this chapter, graphene, graphite, and carbon nanotubes (CNTs) are characterized through AFM, Raman Spectroscopy and TERS. Since these methodologies produce last amount of data, machine learning protocols are used to analyze and sort the collected spectra. Specifically, artificial neural networks (ANN) are exploited for the generation and rapid analysis of hyperspectral maps of TERS of CNTs.

3.1 AFM and Raman Spectroscopy Characterization of Graphene and Graphite

Graphene powder was obtained from KWI Polymers Solutions (Boisbriand, Quebec, Canada). The preparation of graphene samples and substrates is explained in Chapter 2. The resulting flakes, obtained from deposition, are shown in **Figure 3.1a.** An AFM scan reveals the different morphologies of the flakes, attributed to the separation method by centrifugation, showing the exfoliation of several sheets with various thicknesses. **Figure 3.1b,c** shows graphene with a thickness of 0.37 nm corresponding to a bilayer, whereas the graphite presents diverse thickness reaching values beyond a micron in some cases. [2] The thickness of flakes was determined in the selected cross sections 1 and 2. Position 1

reveals graphene sheet (**Figure 3.1b**) whereas location 2 shows graphite with a thickness of 4.75 nm, equivalent to ~12 layers (**Figure 3.1b**). Flake dimension range in lateral size between 5 nm to 3 μm, noticing that as the lateral dimension increases, there is a greater chance to find multilayered materials.

We characterized graphite through Raman spectroscopy using 638 nm laser excitation and 600 gr/mm grating. The observed main three modes are displayed in **Figure 3.1d**. As explained in Chapter 1, Raman spectroscopy is a vibrational technique that provides information of chemical structure, phase, crystallinity, and interactions between molecules. For the graphene case, its electronic and chemical properties are bound by its crystallinity and chemical structure.

The D band, observed at 1326 cm^{-1}, is attributed to structural defects in the graphitic plane. The appearance of this out-of-plane band, indicates the presence of defects along the flake. A, low intensity, or absence reveals an unaffected sp^2 that is not excited due to symmetry restrictions. The G primary band also known as graphite mode, is an in-plane mode that appears in any sp^2 carbon material and shifts slightly depending on the specific allotrope. The G band originates from a double degenerate phonon mode longitudinal (LO) and transverse optical (iTO) at the Γ point in the Brillouin zone center and it is related to the E$_2$g symmetry mode.[3] Its wavenumber is 1580 cm^{-1}. In our results we found a third band G', also known as 2D which is a second-order overtone of a D band, and it is dependent on the laser excitation energy. A simple analysis in our characterization identified a graphite flake. The determination of G' broad band through a Lorentzian fit approximated full width half maximum (FWHM) of a broad band of 100 width, determining the multi-layered flake.[4]

Due to the limitation on the optical view magnification bound to the diffraction limit in confocal microscope, we could not obtain the exact of number of graphene sheet layers within the substrate. To determine the thickness, defects, wrinkles and even chirality we characterized the flakes using TERS technique.
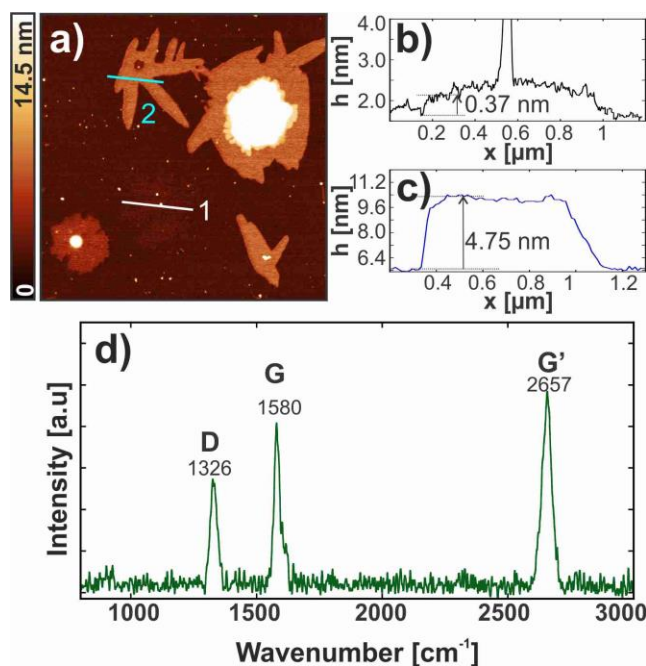
Figure 3.1 a) AFM of different flakes of graphene and graphite showing selected cross sections. Height profiles are displayed for b) graphene and c) graphite. d) Raman spectrum of graphite.

3.2 Tip-Enhanced Raman Spectroscopy of Graphite

TERS was performed on graphene sheets and graphite to reveal surface defects and wrinkles. TERS spectra were acquired with a 638 nm using 600 gr/mm grating with 400ms of exposure per pixel. For further experimental methods refer to Chapter 2.

Results are observed in **Figure 3.2a-d**. This multilayer sample was composed of 15 layers. Such thickness is indicative of a graphitic character instead of graphene. In the averaged TERS spectra, shown in **Figure 3.2a,** the D, G and G' modes have a maximum intensity value on locations 1, 2 and 3. Modes were fitted through a Lorentzian function and analyzed using Labspec 6 program. D band's maximum wavenumber were found to be 1348, 1334 and 1354, for positions 1,2,3, respectively. D band wavenumber changes accordingly to the level of disorder. Results indicate the greater are the defects, the greater is the intensity. Position 3, where the flake is twisted, reveals a greater intensity. On

contrary, spectra from position 1 and 2 spectra present a very low intensity of the D band, most likely due to a larger thickness; a greater crystallinity implies less disorder. [5] The G band maximum wavenumber varies as well only for average spectrum 1 showing 1585 cm^{-1} in comparison to the 1591 cm^{-1} modes found in spectra 2 and 3, that is a 5 cm^{-1} redshift. The shift can be attributed to a possible strain in the numerous graphene layers. [6] For the G' band case, it was found drastic shifts depending on the positions on the surface. The maximum wavenumber observed were 2665, 2651 and 2658, from position 1,2,3, respectively. The G' mode wavenumber can also reveal the thickness dependency on the number of graphene sheets. [7] To generate TERS maps, selected integrated region of bands were chosen as follows: [1308-1382] cm^{-1} for D band, [1540-1620] cm^{-1} for G band and finally [2650-2731] cm^{-1} for G' band as depicted in **Figure 3.2b-e**. There was a greater TERS intensity signal in the range of 5.44-5.76×10^{5} for the G' band than the other bands, rendering improved details in the surface topography. An all-color map is generated from the combination of the D, G and G' integrated bands that shows the wrinkle and small strand in the surface near position 2 achieved by the high spatial resolution of the TERS technique. In general, our experimental data show a low TERS enhancement of ~1.3 factor enhanced signal of the G band, also referred as a contrast, [8] which was described in **equation 1.4** of chapter 1. TERS enhancement is analyzed through a tip-in/ tip-out experiment (see **Appendix A1)**, the low enhancement is most probably due to in-plane vibrations of graphene and out-of-plane enhancement of the electric field along the coated AFM tip. [9]
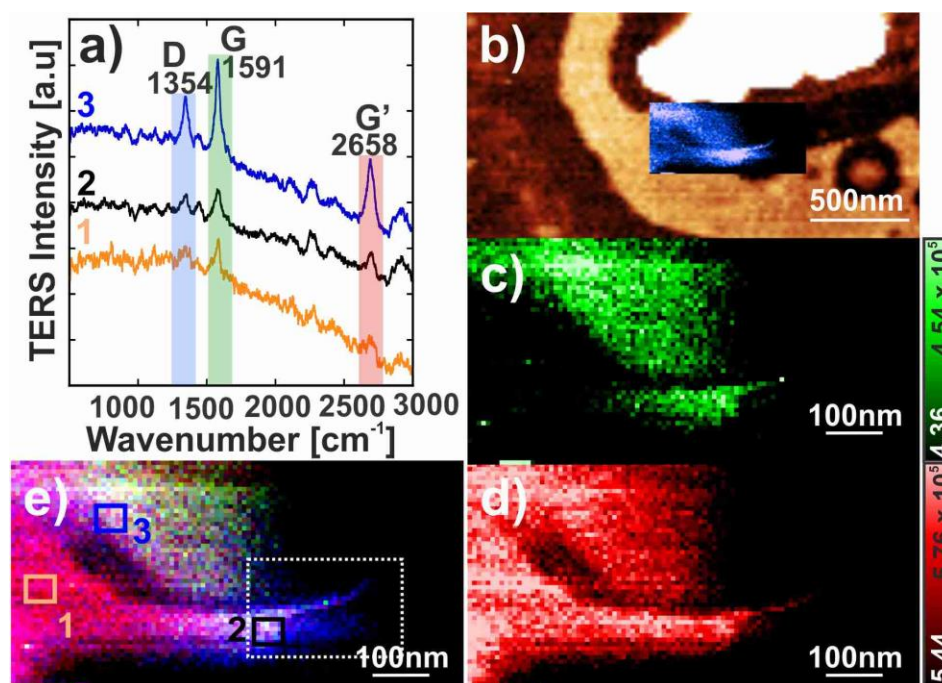
Figure 3.2 a) Averaged TERS spectra extracted from different surface locations of the graphite flake. TERS maps generated by integrated b) D band overlapped with AFM scan, c) G band and d) G' band. e) All colored map generated by integrating all D, G and G' modes illustrating location of average extracted spectra from a) and white square showing wrinkles over the surface of graphite.

3.2.1   Analysis of Defects

The intensity ratio (I_D/I_G) between the D and G band, has been correlated to topographical defects revealed by AFM and crystallinity of graphite. Ratio indicates the amount of disorder associated with defects in the surface of the graphite. As this ratio value increases, the presence of defects increases. Published work on graphite attributes poor crystallinity to intensity ratios in the range of 1 to 2.6 whereas a high crystalline character is associated with ratio varying from 0.1 to 0.3. [10] **Figure 3.3a,b** shows the ratio map obtained in two flakes through TERS, in which the colored bar indicates the I_D/I_G ratio. The ratio map in **Figure 3.3a** highlights values between 0.92 to 1.06. Values greater 1 express poorer crystallinity on the graphite sheet which compared with the TERS map of **Figure 3.2e**

reveals the presence of wrinkles and twists in the surface associated to a greater disorder. A thinner graphite flake (**Figure 3.3b**) was characterized by TERS. The I_D/I_G ratio ranged from 0.9 to 1.2. The greatest ratio of approximately 1.2 is located on the area where a grain boundary is present. On the contrary, the lowest ratio corresponds to a place where the thickness of the layers increases. In our study, I_D/I_G indicates that the graphite samples have poorer crystallinity.
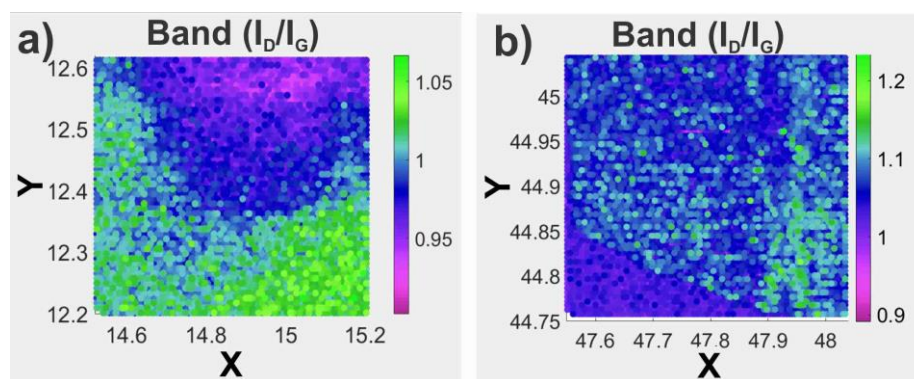
Figure 3.3 TERS ratio map of I_D/I_G of two graphite flakes with a) less disorder b) greater disorder in their defect ratio structure.

3.3 Tip-Enhanced Raman Spectroscopy of Single-Walled Carbon Nanotubes (SWNTs)

This section explains measurements obtained through TERS maps on single-walled carbon nanotubes (SWNTs), which served as reference for nanoscale object. TERS spatial resolution together with spectral selectivity is used to facilitate discrimination of semiconductive and metallic materials. By exploiting artificial neural networks, we characterize SWNTs. Two models are developed. The first model classifies the spectra as representing CNTs or background whereas the second model identifies the existence of three main vibrational modes. Finally, enhanced visualizations of CNTs helps in the analysis of defect areas.

3.3.1 Optical Resolution and Mapping of 1D CNTs

Raman spectroscopy has helped to provide measurement of quality conductivity, chirality, and electron quantum confinement in single-walled nanotubes. [11] However due to its lack of high spatial resolution, TERS is necessary to provide Raman measurements at the scale of a single carbon nanotube.

As mentioned in Chapter 2, two different CNTs were prepared to identify major differences in the Raman modes. The topography and the TERS maps of the G mode of a bundle of semiconductive CNTs that splits into several smaller bundles are shown in **Figure 3.4a,b**. The cross sections displayed in **Figure 3.4b** corresponding to different areas of the sample are indicative of the lateral topographical resolution of our AFM instrument which is convoluted by the tip geometry. These values are larger than Z values providing a more precise assessment of the diameter of the bundles. The cross sections 1-3 are reported in **Figure 3.4c**. The lateral measurements based on full width at half height varies from 21-50 nm, meanwhile the height of the CNT bundles varies from 1 to 10nm. TERS images, based on the integration of the G mode (**Figure 3.4d**), shows the cross sections that are sharper than the topographical images due to the localized electromagnetic confinement at the tip's apex. The smaller nanotube bundle measured indicates that the estimated spatial resolution is ~21 nm a value that is limited by the tip's geometry. A higher spatial resolution could be reached if the rougher coating single metal can generate an even smaller nanoparticle at the extremity of the probe. [12]
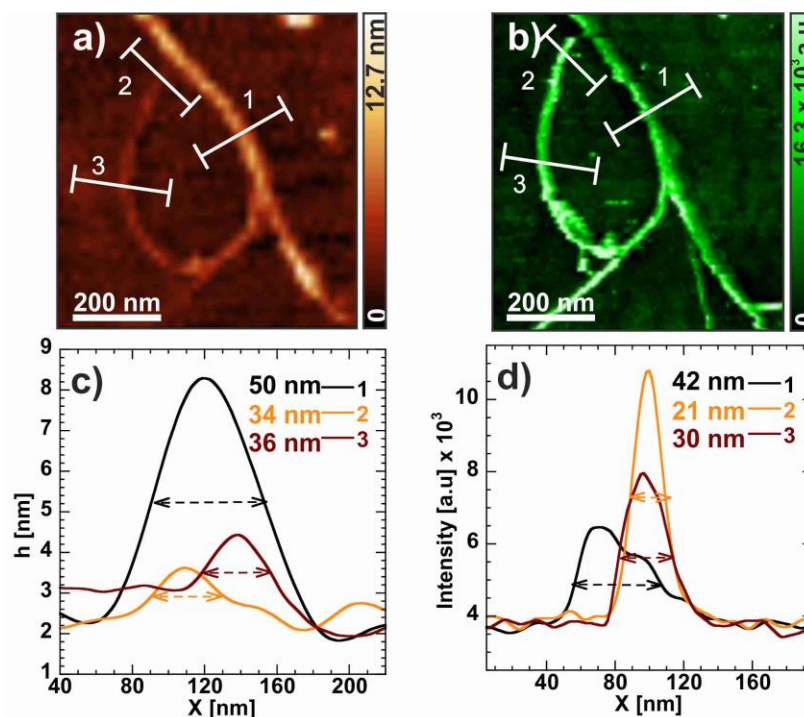
Figure 3.4 a) AFM height profile scan of the semiconductive SWNT. b) TERS maps shows the G band intensity of the semiconductive CNT. Cross sections corresponding to 1-3 of the c) height profiles corresponding to the topography and d) TERS G band intensity band. Reproduced from [13] with permission from the PCCP Owner Societies.

In this work we use TERS to identify the semiconductive or metallic character of a mixture of nanowires by determining the spectral shift and broadening of the G mode into G^+ and G^- bands as shown in **Figure 3.5a-d**.

A semiconductive wire was investigated by TERS and is shown in **Figure 3.5a,c** . The colored boxes shown in the map in **Figure 3.5a** correspond to the average spectra in **Figure 3.5c**. In contrast, for the metallic nanowires (**Figure 3.5b**), the TERS spectra of **Figure 3.5d** is clearly shifted and broadened for the G- band.

For the metallic SWNTs shown in **Figure 3.5b**, averaged areas were selected to show the shift and structure of the split from the referred two modes. Previous work has reported that the G^+ and G^- modes are associated with longitudinal-optical (LO) and transverse optical (TO) phonons. [14, 15] In metallic nanotubes, the LO phonon appears with a broader

band shift (**Figure 3.5d**, G$^-$ band) due to the conduction of electrons representing a continuum plasmon. [14] However, given that not all areas show this G$^-$ band shift, some areas are presumably semiconductive. Although **Figure 3.5d** shows the blue and green spectra from the averaged areas to be associated to a metallic property, it is arguable the red spectrum still has a semiconductive character. Regardless of conductivity, our ANN models do not present any decrease in performance and maintain sensibility and applicability.
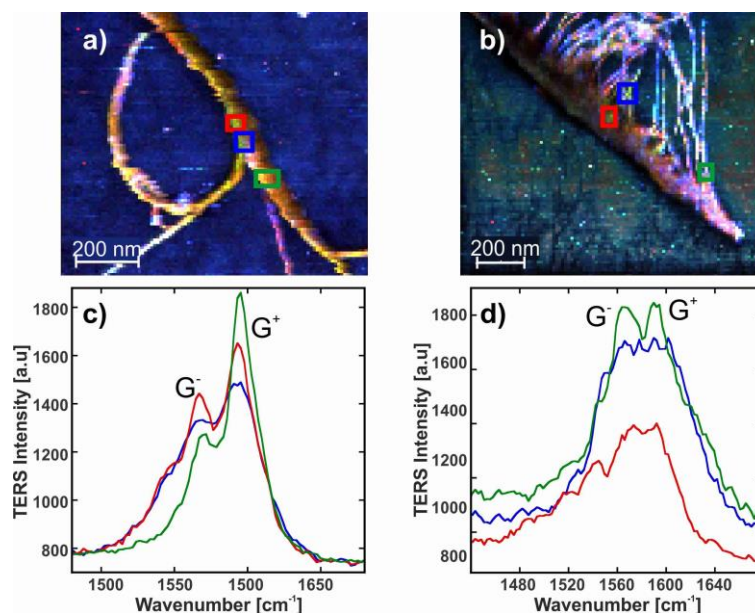
Figure 3.5 TERS all color maps generated from integration of D, G and G' bands for a) semiconductive and b) metallic SWNT. Extracted average spectra (square red, blue and green) revealing the G band for a c) semiconductive and d) metallic SWNT. Reproduced from [13] with permission from the PCCP Owner Societies.

Additional vibrational modes that were not characteristic of CNTs were detected and correspond to C-H vibrations and the iTOLA band. These bands are attributed to organic surfactant residue left from the sample preparation or from combinations of vibrational modes. [16, 17] In particular, the iTOLA band appears as a result of the combination of optical and acoustic modes, [18] and might be introduced due to the presence of diluted acid treatment

to remove organic residue in the sample preparation. iTOLA mode depends on the double resonance process which is dependent on the excitation wavelength. [17]

TERS enhancement is analyzed through a tip-in/ tip-out experiment (see **Appendix A2),** which gave a factor of ~1.6.

3.3.2   TERS Carbon Nanotubes Study Using ANN

The architecture of the ANNs can be split into three components: the input layer, the hidden layer, and the output layer. The input layer receives the number of independent features that are fed into the neurons. The hidden layer is composed of neurons responsible for the mathematical computations. In the case of ANN Model 1 and Model 2, all abstractions have two hidden layers of 20 neurons each. The output layer uses a function to normalize the output as a 0 or 1, which correlates to our dependent features, the values being predicted. For the case of ANN Model 1, there is a 'background' or 'carbon nanotube' classification decision. For the case of ANN Model 2, the output corresponds to 'Noise' or 'D-Band' for the first constituent, 'Noise' or 'G-Band' for the second constituent, and 'Noise' or '2D'-Band' for the third constituent. Optimal results from the ANN models were achieved by splitting the experiment's data set (examples) as 70% for training and 30% for validation. Once the models have been constructed and trained, our ANNs were used to make predictions on unseen TERS data to assess the accuracy of real applications. If unsatisfactory, the workflow was checked to adjust accordingly and re-evaluate accuracy. This continuing process came to a halt as real application accuracies of 98% for Model 1 and 96% for Model 2 were achieved. The process can be further observed in **Figure 3.6**.
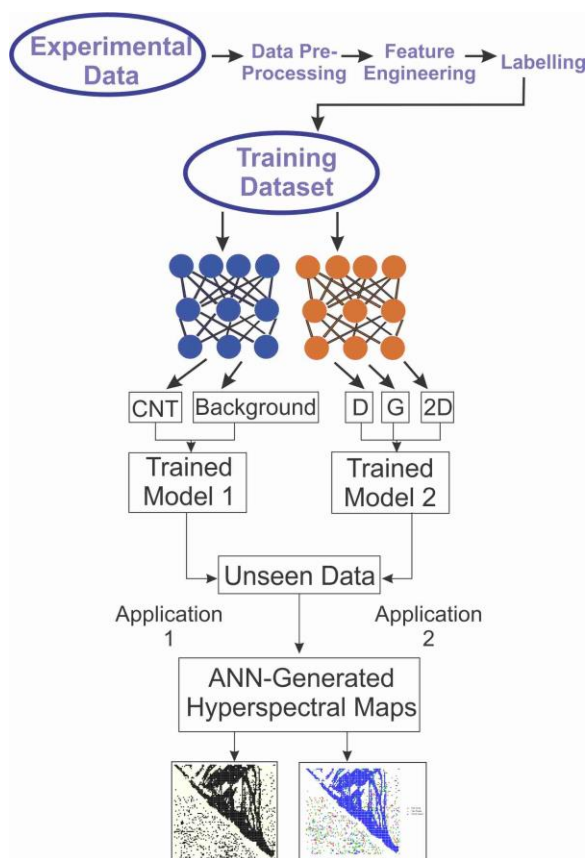
Figure 3.6 Machine learning workflow, identifying the models 1 and 2. Reproduced from [13] with permission from the PCCP Owner Societies.

Hyperspectral maps shown in **Figure 3.7a-d** were generated with ANN model 1, and model 2 for the respective semiconductive and metallic CNTs. Model 1 discriminated only background versus the vibrational signals of carbon allotropes and nanotubes as illustrated in **Figure 3.7a,c.** Additionally, model 2 was applied to reveal number of vibrational bands present at each carbon allotrope located at specific set of (X,Y) coordinates. Possible number of vibrational bands corresponds to three modes observed. The high dispersion of vibrational signals observed in the maps are attributed to the sonication of the CNT preparation, which may have generated allotropes sediments. For further rapid analysis, a combination of model 1 and 2 is presented in **Figure 3.7b,d** illustrating the classifications of specific peaks. The composition breakdown is categorized as only G (one peak), only D and G (two peaks), only G and G' (two peaks), or D and G and G' (three peaks). As a

result, these two figures can give a comprehensive understanding of the total band composition that appears at each specific XY coordinate of the hyperspectral map.

The absence of G' band in sites outside of the CNTs (**Figure 3.7b**) may be attributed to the oxidation of the allotrope carbon sediments. Furthermore, the higher density of the G+G' bands (orange dots) appearing at the border of the semiconductive CNT, is associated to an apparent absence of the D band in these vicinities. The small or inexistent intensity value of the D band revealed the non-presence of defects. The blue dots representing locations where all three vibrational modes are present, are consistent with the characteristic vibrational spectra of SWNT. The straggling blue dots found sparsely outside the nanotubes may be associated to residues because of sonication. The same observations apply for metallic CNT as depicted in **Figure 3.7c,d**.
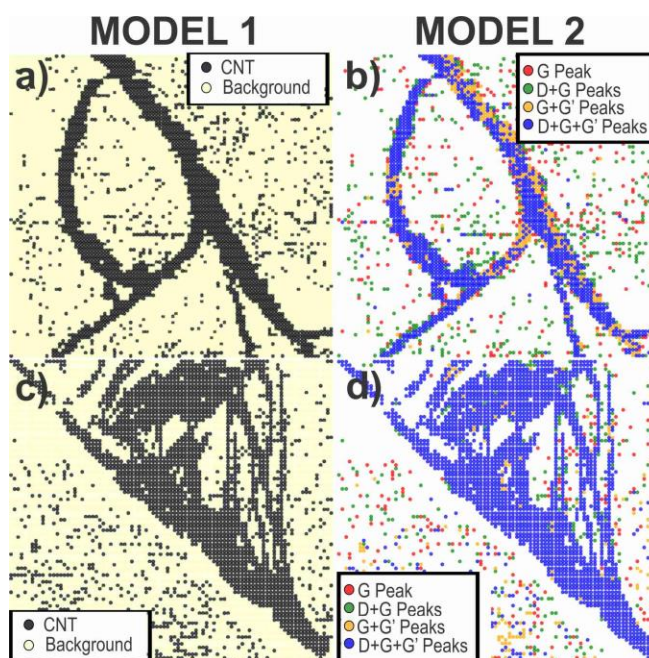
Figure 3.7 Semiconductive CNT of a) ANN Model 1 discriminating background versus carbon nanotube and b) ANN model 1 +2 classifying spectra into different modes present. Metallic CNT revealing c) ANN Model 1 and d) ANN model 1 +2. Reproduced from [13] with permission from the PCCP Owner Societies.

3.3.3   Accuracy and Defect Analysis

Defect analysis was performed through the TERS software and furthered improved using ANN. Hyperspectral maps generated using the combination of models 1 and 2 are represented in **Figure 3.8a,b** in the form of ratio of intensities of the D and G modes, I_D/I_G, for the semiconductive and metallic SWNT. The maps reveal the defect distribution along the surface of the SWNTs of the two samples. ANN generated maps provide a more accurate determination of background, highlighting the presence of debris around the main bundles. The precision relies on ANN model 2 algorithm which takes into consideration only CNT classification from model 1 instead of analyzing the whole TERS raw data and giving just approximate values of defect ratio. As a result, maps generated by ANN render a higher spatial resolution and provide an accurate and good estimate of the I_D/I_G ratio range. Average spectra, extracted from the TERS image data is presented in **Figure 3.8c,d**. By comparing two different CNTs (**Figure 3.8a,b**), the metallic one has higher defect density factor (**Figure 3.8b**), represented by the darker orange regions localized on the bundles. This is attributed to those SWNTs with many bundled threads of CNTs that have been mechanically ripped during the scanning TERS measurement. For the semiconductive SWNT shown in **Figure 3.8a, c,** a similar observation regarding the higher density ratio of defects can be found at the curvature of bent bundles. The average spectra observed in **Figure 3.8c, d** reveals several peaks (splitting) within the D band mostly observed for the metallic CNT. The latter may be attributed to the previously reported double resonance theory. [19] The double resonance is associated to an elastic scattering of the phonons around the K and Γ points in the graphene Brillouin zone. [17]
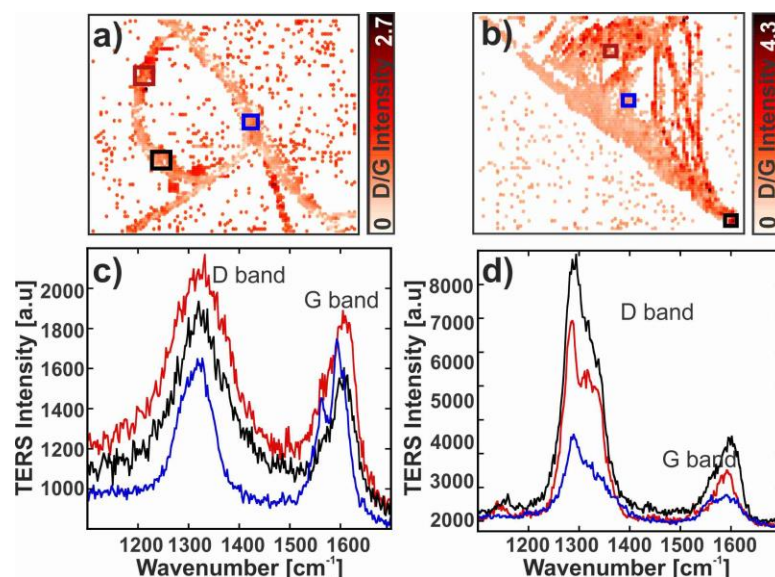
Figure 3.8 Maps from combined ANN model 1 and 2 showing I$_D$/I$_G$ ratio for a) semiconductive and b) metallic SWNTs. TERS spectra for each average location determined in a) and b) for the cases of c) semiconductive and d) metallic SWNT. Reproduced from [13] with permission from the PCCP Owner Societies.

3.4   Conclusion

In this chapter we characterize graphite and SWNTs from prepared samples, using high spatial resolution TERS mapping. We find bilayer graphene with a thickness of 0.37 nm, whereas for graphite, the thickness varies. TERS acquisition on graphene is problematic due to in-plane mode vibrations. The low enhancement TERS signal of factor ~1.2-1.3 from graphene sheet made it difficult to distinguish the vibrational bands. On contrary, TERS signal is detectable for graphite. The side illumination of the TERS tip geometry setup facilitates revealing specific defects on the surface such as wrinkles and ruptures. I$_D$/I$_G$ maps of graphite show the specific XY coordinates and regions for poor crystallinity over the surface of two different flakes.

For CNTs, we determine the smallest spatial resolution of ~21 nm for a bundle. Such resolution goes beyond the diffraction limit revealing the importance of the TERS technique. Metallic and semiconductive SWNT reveal a different split of the G vibrational

band (G^+ and G^-) that is attributed to longitudinal-optical (LO) and transverse optical (TO) phonons. The importance of the SWNT classification is essential for several applications in industry. It can be assumed that the samples presented in this study are mixtures of conformational zigzag and arm-chair structures of SWNT bundles. According to our results, D band decreased in specific locations of the semiconductive CNT bundle due to electron-phonon coupling.

ANN renders fast and enhanced TERS hyperspectral maps for the analysis of CNTs. ANN model 1 increases the contrast and accurately segregates CNT spectra from background. Model 2 shows the composition of vibrational bands at position coordinates X, Y. Results agree with literature findings demonstrating the importance of instruction of machine learning for rapid analysis. Artificial intelligence and machine learning have more to offer that preliminary work mentioned in this chapter. Classification, supervised learning, and deep learning with ANNs only scratch the surface of the capabilities of machine learning.

3.5 References

(1) El-Kady, M. F.; Shao, Y.; Kaner, R. B. Graphene for Batteries, Supercapacitors and Beyond. *Nat. Rev. Mater.* **2016**, *1* (7), 16033.

(2) Kumar, V.; Kumar, A.; Lee, D.-J.; Park, S.-S. Estimation of Number of Graphene Layers Using Different Methods: A Focused Review. *Materials* **2021**, *14* (16), 4590.

(3) Pimenta, M. A.; Dresselhaus, G.; Dresselhaus, M. S.; Cançado, L. G.; Jorio, A.; Saito, R. Studying Disorder in Graphite-Based Systems by Raman Spectroscopy. *Phys. Chem. Chem. Phys.* **2007**, *9* (11), 1276-1290.

(4) Ni, Z. H.; Wang, H. M.; Kasim, J.; Fan, H. M.; Yu, T.; Wu, Y. H.; Feng, Y. P.; Shen, Z. X. Graphene Thickness Determination Using Reflection and Contrast Spectroscopy. *Nano Lett.* **2007**, *7* (9), 2758-2763.

(5) Sato, K.; Saito, R.; Oyama, Y.; Jiang, J.; Cançado, L. G.; Pimenta, M. A.; Jorio, A.; Samsonidze, G. G.; Dresselhaus, G.; Dresselhaus, M. S. D-band Raman Intensity of

Graphitic Materials as a Function of Laser Energy and Crystallite Size. *Chem. Phys. Lett.* **2006**, *427* (1), 117-121.

(6) Wu, J.-B.; Lin, M.-L.; Cong, X.; Liu, H.-N.; Tan, P.-H. Raman Spectroscopy of Graphene-based materials and Its Applications in Related Devices. *Chem. Soc. Rev.* **2018**, *47* (5), 1822-1873.

(7) Shearer, C. J.; Slattery, A. D.; Stapleton, A. J.; Shapter, J. G.; Gibson, C. T. Accurate Thickness Measurement of Graphene. *Nanotechnology* **2016**, *27* (12), 125704.

(8) Stadler, J.; Schmid, T.; Zenobi, R. Developments in and practical guidelines for tip-enhanced Raman spectroscopy. *Nanoscale* **2012**, *4* (6), 1856-1870.

(9) Kumar, N.; Mignuzzi, S.; Su, W.; Roy, D. Tip-Enhanced Raman Spectroscopy: Principles and Applications. *EPJ Tech. Instrum.* **2015**, *2* (1), 9.

(10) Inam, A.; Brydson, R.; Edmonds, D. V. Raman Spectroscopy Study of the Crystallinity of Graphite Formed in An Experimental Free-Machining Steel. *Mater. Charact.* **2020**, *163*, 110264.

(11) Tian, Y.; Jiang, H.; Laiho, P.; Kauppinen, E. I. Validity of Measuring Metallic and Semiconducting Single-Walled Carbon Nanotube Fractions by Quantitative Raman Spectroscopy. *Anal. Chem.* **2018**, *90* (4), 2517-2525.

(12) Bhattarai, A.; Crampton, K. T.; Joly, A. G.; Wang, C.-F.; Schultz, Z. D.; El-Khoury, P. Z. A Closer Look at Corrugated Au Tips. *J. Phys. Chem. Lett.* **2020**, *11* (5), 1915-1920.

(13) Kajendirarajah, U.; Olivia Avilés, M.; Lagugné-Labarthet, F. Deciphering tip-enhanced Raman imaging of carbon nanotubes with deep learning neural networks. *Phys. Chem. Chem. Phys.* **2020**, *22* (32), 17857-17866.

(14) Okuno, Y.; Saito, Y.; Kawata, S.; Verma, P. Tip-Enhanced Raman Investigation of Extremely Localized Semiconductor-to-Metal Transition of a Carbon Nanotube. *Phys. Rev. Lett.* **2013**, *111* (21), 216101.

(15) Xu, Z.; Liang, Z.; Ding, F. Isomerization of sp2-Hybridized Carbon Nanomaterials: Structural Transformation and Topological Defects of Fullerene, Carbon Nanotube, and Graphene. *Wires. Comput. Mol. Sci.* **2017**, *7* (2), e1283.

(16) Sheremet, E.; Rodriguez, R. D.; Agapov, A. L.; Sokolov, A. P.; Hietschold, M.; Zahn, D. R. T. Nanoscale Imaging and Identification of a Four-Component Carbon Sample. *Carbon* **2016**, *96*, 588-593.

(17) Rao, R.; Reppert, J.; Podila, R.; Zhang, X.; Rao, A. M.; Talapatra, S.; Maruyama, B. Double Resonance Raman Study of Disorder in CVD-Grown Single-Walled Carbon Nanotubes. *Carbon* **2011**, *49* (4), 1318-1325.

(18) Dresselhaus, M. S.; Dresselhaus, G.; Saito, R.; Jorio, A. Raman Spectroscopy of Carbon Nanotubes. *Phys. Rep.* **2005**, *409* (2), 47-99.

(19) Puech, P.; Kandara, M.; Paredes, G.; Moulin, L.; Weiss-Hortala, E.; Kundu, A.; Ratel-Ramond, N.; Plewa, J.-M.; Pellenq, R.; Monthioux, M. Analyzing the Raman Spectra of Graphenic Carbon Materials from Kerogens to Nanotubes: What Type of Information Can Be Extracted from Defect Bands? *C* **2019**, *5* (4), 69.

Chapter 4

4   Growth of Spiral 1T Vanadium Disulfide (VS$_2$) Pattern and Characterization Through Tip-Enhanced Raman Spectroscopy

In this chapter we introduce 2D materials known as transition metal chalcogenides (TMDs). TMDs with metallic character have received intense interest for a broad range of applications ranging from battery development to magnetic quantum devices. [1, 2] Using atmospheric pressure chemical vapor deposition vanadium disulfide (VS$_2$) flakes are synthesized with a metallic 1T phase which displays either flat surface or shows nanoscale spiral ripples over its surface. To understand the origin of these surface ripples, tip-enhanced Raman spectroscopy (TERS) and Kelvin probe force microscopies (KPFM) were jointly used to investigate their composition and their electronic properties.

4.1   Growth and Topography of VS$_2$

VS$_2$ flakes were synthesized using CVD technique as described in the experimental methods of Chapter 2. The synthesis recipe precursor quantities and flow remained the same except for the introduction of a fast change in the temperature gradient accomplished by physically shifting the furnace for the rippled flakes case. **Figure 4.1a** illustrates the sketch of the atmospheric pressure CVD VS$_2$ procedure used for the synthesis. Given that the VCl$_3$ precursor has a high reactivity with light and moisture conditions, it needs to be handled in an inert chamber environment. The VS$_2$ synthesis reaction proceeds only with the addition of the H$_2$ gas flow and sulfur in inert conditions, otherwise the reaction becomes thermodynamically infeasible. To overcome such condition, it is necessary the addition of H$_2$ flow to help the sulfurization process, modifying it and making the following reaction occur: [3, 4]

$$VCl_4 \text{ (g)} + S_2 \text{ (g)} + 2H_2 \text{ (g)} \rightarrow VS_2 \text{ (s)} + 4 \text{ HCl (g)}$$
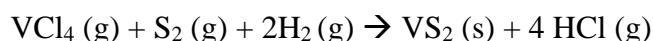
The sulfur powder precursor (S) was initially located outside the furnace but close to its edge. A magnet is used to push the S precursor once the temperature reaches 630°C

forming the bulk or thin layered VS$_2$ flakes depicted in **Figure 4.1b.** The rippled 1T-VS$_2$ (**Figure 4.1c**) were formed when the whole furnace was shifted upwards by 1.5 cm without the assistance of the magnet once the temperature reaches the final ramp. The growth substrates used were Silicon (Si) and mica. Mica is predominantly used for a lateral growth meanwhile Si substrate induce an axial growth.
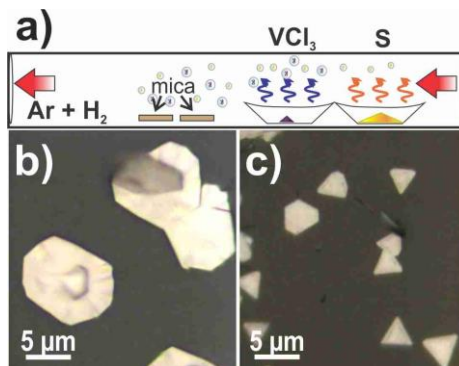
Figure 4.1 a) CVD sketch of VS$_2$ synthesis process. Optical micrograph of b) bulk and c) rippled 1T-VS$_2$ flakes.

Lateral dimension growth of flakes with no surface ripples varied from 1 µm to 20 µm. Various thicknesses were obtained through the synthesis process as shown in the AFM scans of **Figure 4.2a-d.** There exists a growth preference of bulk flakes depicted in the AFM scan of **Figure 4.2a** showing a thickness of ~105 nm whereas the bulk flakes show thicknesses beyond 1 µm. Height profiles reveal that the lowest synthesized crystal thickness of VS$_2$ on mica substrate was 12 nm (**Figure 4.2b**). Triangular, half and complete hexagonal structured VS$_2$ flakes were grown as shown in **Figure 4.2b, c**; these flakes vary in thickness by 5 nm**.** Other rippled flakes reveal a periodic right- or left-handed spiral of hexagonal shape which grows from the center towards the outside of the flake. As displayed in **Figure 4.2d,** the approximate edge height of 102 nm has a periodicity.
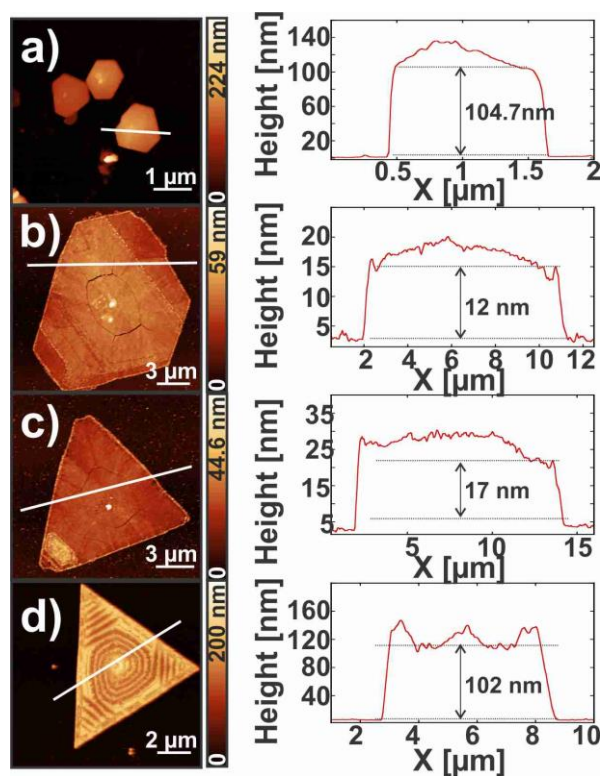
Figure 4.2 AFM scans of a) bulk, b, c) thin and d) rippled VS$_2$ flakes. The corresponding height profiles are shown next the micrographs to the right.

Table 4.1 summarizes the height, averaged period, and depth of the spirals of several VS$_2$ flakes. The periodicity was measured in 5 flakes selected from different samples obtained by repeating the CVD procedure. There was no thickness-dependence on chirality, and both left- and right-handed spirals grow from the center towards the edge of the flakes. Interestingly, the periodicity of the ripples (Λ~100-400 nm) depends on the location of the substrate in the CVD furnace and consequently on the change in temperature due to the shift of the furnace.

Table 4.1 Summary of averaged period versus averaged depth within each sample of the rippled VS$_2$ flakes.

Sample Number	Average of period [nm]	Average Depth [nm]	Thickness [nm]
1	272	27.5	30
2	226	26.0	43.2
3	337	23.0	52.3
4	297	27.0	68
5	358	28.6	81
6	159	16.4	93
7	310	33.4	109
8	382	35.5	124
9	400	26.3	132
10	259	17.5	139
11	400	27.0	140
12	347	29.3	147
13	290	16.8	183
14	265	16.8	193

The surface corrugation of the VS$_2$ rippled flakes is composed of small grains with different orientation as depicted in **Figure 4.3a-f**. Triangular VS$_2$ flakes were synthesized, mostly grown near the edges of the mica substrate as depicted in the AFM micrograph and optical image of **Figure 4.3a,b**. A greater detail in the growth predisposition of crystallites is observed in the SEM (**Figure 4.3c**). Respective zoom areas of the AFM and SEM of flakes are depicted in **Figure 4.3d, f.** Overall, around 20% of the flakes displayed the spirals with R or L chirality. In the maxima of the corrugation the crystallites are oriented vertically, while in the minima areas, an in-plane orientation is predominantly observed, this is further depicted in the sketch in **Figure 4.3e**.
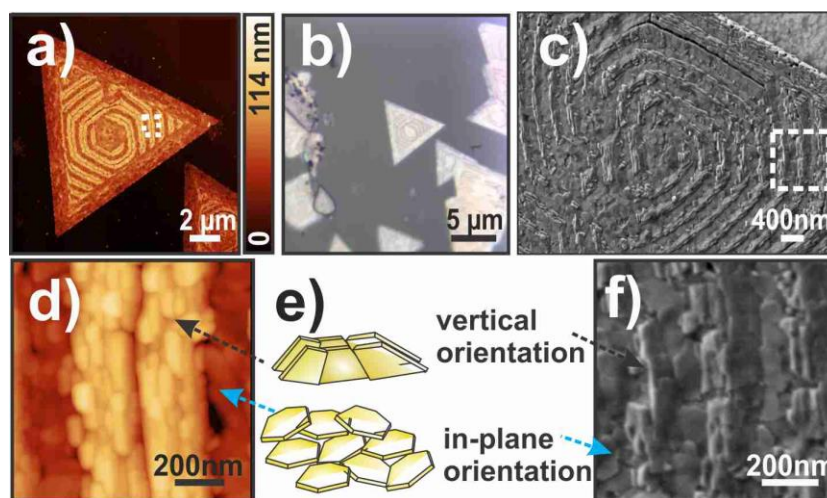
Figure 4.3 a) AFM micrograph and b) optical image of as grown VS$_2$ flakes on mica flurophlogopite. c) SEM image, d) AFM micrograph zoom-in of a) and e) sketch depicting the local grain orientation of the surface structure. f) SEM image zoom-in of c).

4.2 Kelvin Probe Force Microscopy (KPFM) of VS$_2$

Kelvin probe force microscopy (KPFM) technique allows nanometer scale imaging of the surface potential. To further understand how the ripples might affect the work function of the VS$_2$ flakes, Kelvin probe force microscopy (KPFM) measurements were performed. Contact potential difference map was acquired with the AFM scan for better correlation as observed in **Figure 4.4a**. The flake showed a left-handed spiral structure. **Figure 4.4b** displays the CPD map in more detail. A spiral modulation of the surface potential and grain boundaries between the different crystal orientations were visible. To assign the surface potential modulation to the topography variation and to calculate the work function of the VS$_2$ a cross-section in the CPD and topography map was taken (see **Figure 4.4c, d**). Results indicated that the surface potential was out-of-phase with the topography, meaning that a local maximum of the corrugation the surface potential is reaching its local minimum. The amplitude of the surface corrugations was ~ 28 nm with its surface potential change of ~20

mV. The work function was calculated from the CPD using the **equation 1.2**. The calibration was performed on a HOPG sample.

V_{CPD} describes the measured surface potential. Solving **equation 1.2** for Φ_{Tip} permits to obtain the work function of the tip:

$$\Phi_{Tip} = eV_{CPD} + \Phi_{HOPG} = 0.27 \text{ eV} + 4.65 \text{ eV} = 4.92 \text{ eV} \qquad (4.1)$$

Now, the work function of the VS$_2$ flake is obtained by solving **equation 4.1** for Φ_{Sample} and adding Φ_{Tip} calculated in **equation 4.2**:

$$\Phi_{VS_2} = \Phi_{Tip} - eV_{CPD} = 4.92 \text{ eV} - (-0.31 \text{ eV}) = 5.23 \text{ eV} \qquad (4.2)$$

The calculated work function of the VS$_2$ flake was ~5.23 eV which is larger than the work function of gold and indicating the intrinsic metallic behavior of the 1T VS$_2$ flake. A plot of the work function modulation along the flake surface is shown in **Figure 4.4e**, revealing a change in the work function of 14 meV caused by the ripples. Previous studies on theoretical simulations revealed a very approximate value for the work function of 5.45 eV for a monolayer of VS$_2$. [5] The small difference between the experimental measured value of the work function and its theoretical value is attributed to the grain orientation and the local geometry variation caused by the ripples. The offset may also be caused by a water layer being formed over the surface, since KPFM is sensitive to small dipoles adsorbed on the surface and absolute values are usually recorded in ultra-high vacuum systems. The comparison with the topography revealed that the work function is larger in regions of a vertical crystal orientation. The modulation of the work function is of interest for the increase of the efficiency of electronic devices, such as photovoltaic devices.
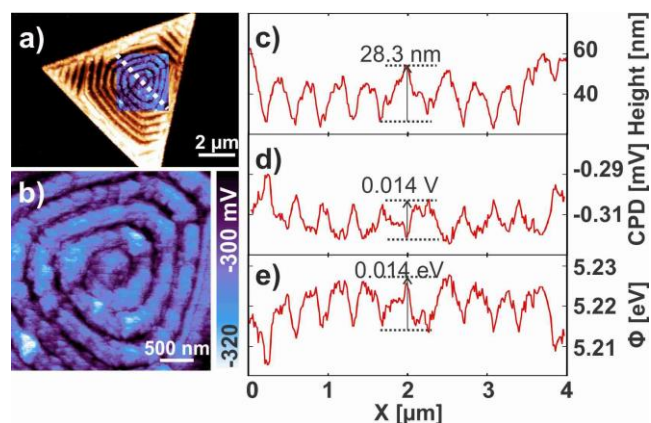
Figure 4.4 a) Overlay of the CPD map with the AFM micrograph of the rippled VS₂ flake. A detailed CPD map with inverted contrast is shown in b). The cross section of the topography is shown in c) and of the CPD in d), indicated by the white line in a). The calculated work function modulation is seen in e).

4.3 Raman Spectroscopy of VS$_2$

The VS$_2$ flakes were characterized through confocal Raman spectroscopy to determine the polymorph conformation of the crystal structure and to observe possible induced shift of the phonon modes caused by the surface spiral pattern. [6] Previous studies revealed a possible photo-oxidation of VS$_2$ at high energy dose illumination through its characterization by Raman spectroscopy.[3] Therefore, it was imperative to characterize the flakes with a low laser power using a longer acquisiton time. In addition, to avoid possible oxidation the TMDs were immediately characterized and kept under inert conditions (Ar) for storage.

Raman spectra of the VS$_2$ flakes are shown in **Figure 4.5a-c**, using a 532 nm and 638nm incident wavelength. The inset shows the optical micrographs for each of the corresponding plots by color scheme. For the 532nm laser excitation in **Figure 4.5a** the A$_{1g}$ out-of-plane mode is found between 324-328 cm^{-1}. [3, 7] Modes in the range 250-276 cm^{-1} are attributed to the E$_{2g}$ mode. Its intensity is lower, since it is an in-plane mode, which agrees with previous reports. [3, 8] In the 100-200 cm^{-1} region other phonon modes are observed, which include 124, 147, 167, and 188 cm^{-1}. In the following, these unassigned modes will be

defined as phonon mode p1, p2, p3 and p4, respectively. These modes have not been assigned to a specific type. However, the 158 cm^{-1} mode is associated with a defect mode that involves a two-phonon process, which was reported for other metallic TMD. [9] A two-phonon process is a second order Raman scattering process in which the photoexcited electron-hole pair excites two phonons with opposed momentum before its recombination. [10-12] In addition, Ji et *al*. mentioned a two-phonon mode for the VS$_2$ in the region of 100-200 cm^{-1}. [3] A blueshift of the A$_{1g}$ mode of 3 cm^{-1} is observed between the red spectrum and the two other spectra in **Figure 4.5a**, which is attributed to the thickness variation of the flake. For comparison, the thicknesses of the flake of the red inset were measured to ~35 nm, while the flake of the blue inset is ~65 nm thick. The height of the flake of the green inset is in the ~ 1 µm range. Between the blue and green spectra no shift of the A$_{1g}$ mode was observed. The E$_{2g}$ mode indicates a blueshift of 7 cm^{-1} for the red spectrum, with respect to the green spectrum, and none between green and blue, which is attributed to the thickness of the flake as well. [1] The p4 mode at 194 cm^{-1} appears more intense and broadened for the thicker flake (green spectrum and optical image in **Figure 4.5a**). This mode is usually seen in VS$_2$ using the hydrothermal method which results in a vertical orientation of the flakes. [13]

Figure 4.5b shows Raman spectra using a 638 nm excitation laser, indicating a fluorescence that is coming from the mica substrate. Furthermore, a blueshift (3 cm^{-1}) for the A$_{1g}$ mode for thin flakes is observed, matching the observations when using a 532 nm excitation. The change in the excitation wavelength is shifting the A$_{1g}$ mode from 324 cm^{-1} to 326 cm^{-1}, which corresponds to a redshift of 2 cm^{-1}. The E$_{2g}$ mode is not observed using 638 nm excitation, which may be attributed to the resonance at 532 nm incident wavelength that causes a charge transfer electronic transition. A confocal Raman map of the p3 mode, under 532 nm excitation, is seen in **Figure 4.5c** and compared with the AFM scan of the flake. A lack in spatial resolution is revealed, making it impossible to reveal the ripples over the surface.
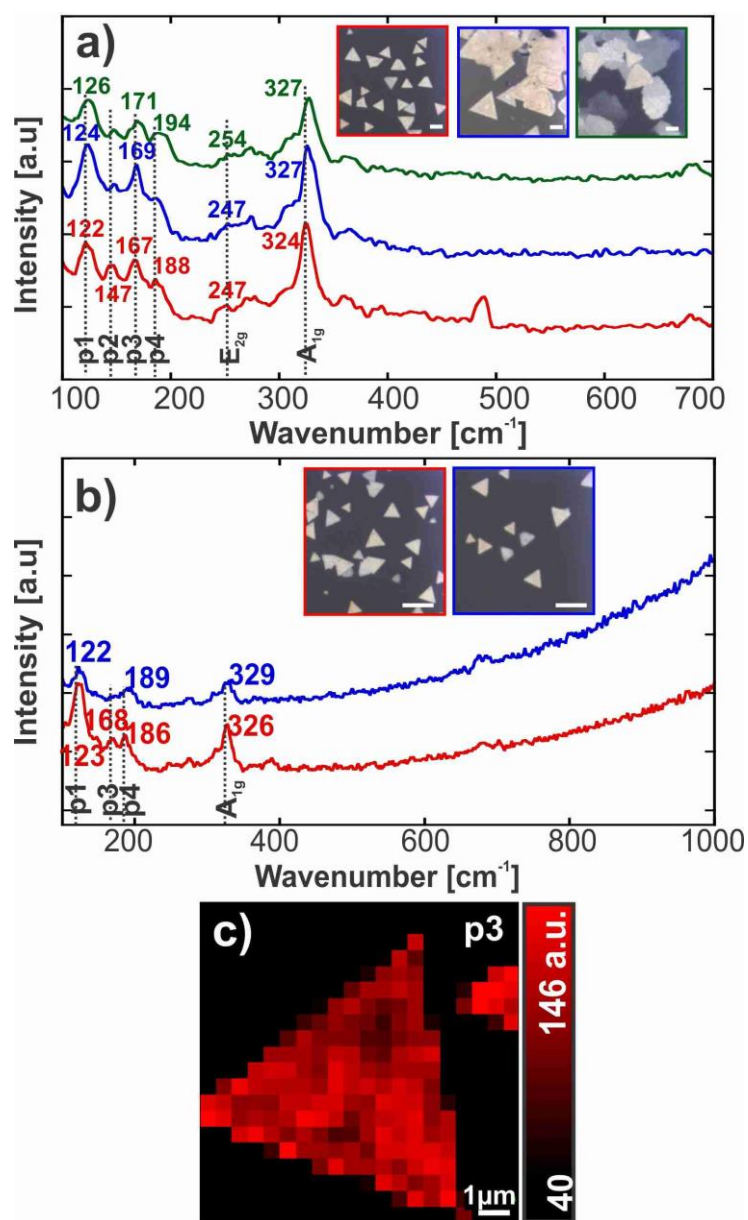
Figure 4.5 Confocal Raman spectra of a) three VS$_2$ flakes with different thicknesses (red: ~35 nm, blue: ~65 nm, green: ~1 µm) using 532 nm excitation laser and b) two different flakes using 638 nm excitation (red: ~35 nm and blue:~20 nm). The inset shows the corresponding optical image with a scale bar of 5 µm. The spectra were offset for clarity. c) Confocal Raman map of the p3 phonon mode, integrated over the spectral range 154-183 cm^{-1} using 532 nm laser excitation. The surface corrugation is not visible, indicating a lack of spatial resolution.

4.4 Tip-Enhanced Raman Spectroscopy (TERS) of VS$_2$

The spatial resolution accessible in TERS yields further topographical details on the ripples and the effect of their orientation on the Raman modes. To benefit from the TERS gap mode procedure, the VS$_2$ flakes were transferred to a gold substrate to avoid photoluminescence and Raman modes of the mica substrate, using the PMMA-transfer method. [14]

Ag coated tips were used in combination with a 532 nm laser, while in the case of a 638 nm excitation Au coated cantilevers were used. The laser was p-polarized for both excitations. The spectra were recorded in Spec-top mode, meaning that for each pixel one spectrum is acquired with the tip in direct contact with the surface. Between two pixels, the sample is moved in intermittent contact mode to prevent the probe from damage and to keep the plasmonic enhancement. The TERS map consists of 64000 spectra in case of the 638 nm excitation, each recorded with an acquisition time of 300 ms and an intensity of ~8×10^7 mW/cm^2. In contrast, only 123 spectra were obtained in the case of the 532 nm excitation, using an intensity of ~3×10^7 mW/cm^2 and an acquisition time of 30 s to avoid photo-oxidation of the flakes.
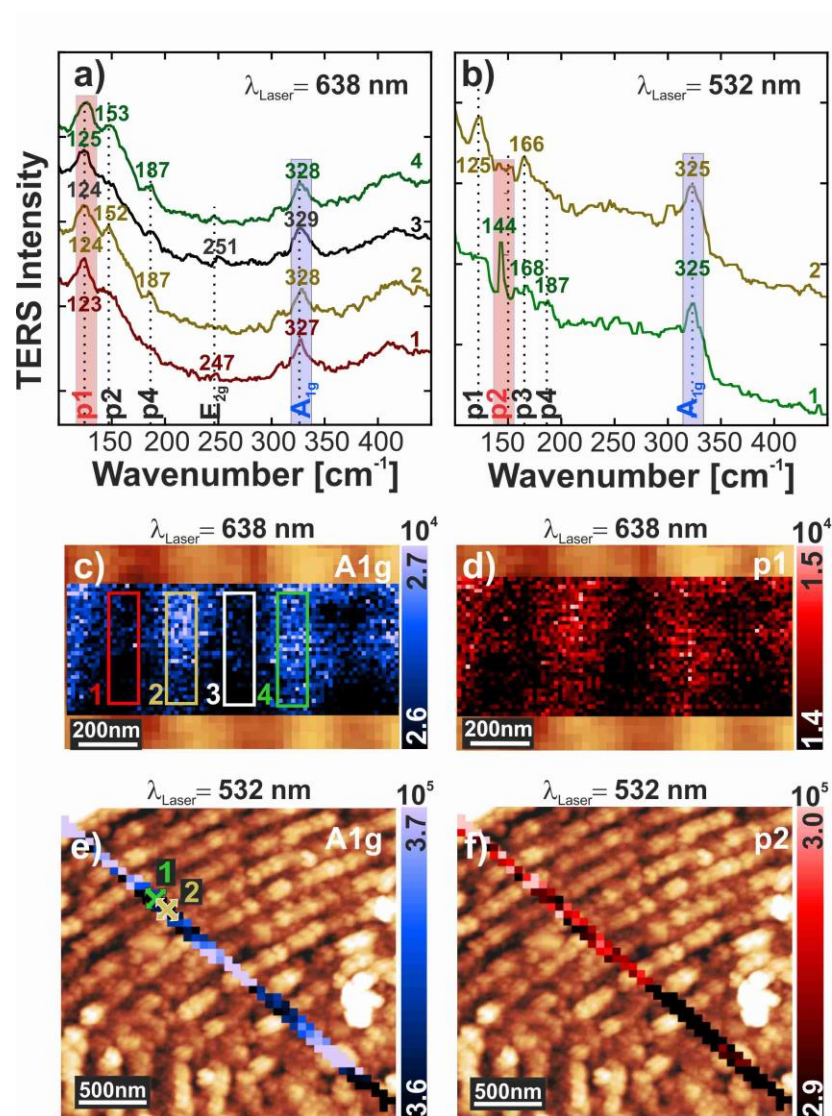
Figure 4.6. TERS spectra using a) 638 nm and b) 532 nm excitation. The overlay of the topography with the TERS map of the A1g mode is shown in c) and of the p1 mode in d) using a 638 nm laser. The 4 colored boxes in c) show the location of the averaged TERS spectra of a). An overlay of the A_{1g} mode with the AFM micrograph using a 532 nm laser is shown in e) and for the p2 mode in f).

Averaged TERS spectra collected at 638 nm excitation in conjunction with a gold tip were acquired at four different positions within the surface corrugation as depicted in **Figure 4.6a**. In contrast, two characteristic point spectra for 532 nm excitation are displayed in

Figure 4.6b. The spectra in **Figure 4.6a** are averaged over 210 spectra (the total number of acquired spectra of the A_{1g} Raman map is 6400). The positions of the averaged TERS spectra of **Figure 4.6a** are indicated by the colored boxes in the overlay of the topography with the TERS map of the A_{1g} mode in **Figure 4.6c**. The overlap of the topography with the TERS maps of the p1 mode are shown in **Figure 4.6d**.

Crystallites that have an in-plane orientation, further shown in the sketch of **Figure 4.3e**, are observed at positions 1 and 3 of the TERS map in **Figure 4.6c** which corresponds to the minimum of the surface corrugation. On the other hand, at positions 2 and 4 of the TERS map in **Figure 4.6c,** the grain orientation appears predominantly vertical with maximum surface relief. The A_{1g} mode appears in the two averaged TERS spectra of the maximum of the surface corrugation at the same position. This contrasts with the spectra at the minima positions (positions 1 and 3) where a blueshift (position 1) and redshift (position 3) of ± 1 cm^{-1} are observed with respect to the A_{1g} wavenumber at positions 2 and 4. The width of the p1 is changing from 13.6 cm^{-1} at position 4 to 2.3 cm^{-1} at position 3. The broadening of the Raman modes at position 4 is attributed to the loss of crystallinity in that area of the flake. [15] The p3 mode is not observed for the 638 nm excitation while it appears under 532 nm excitation. The p2 and p4 mode only appear at the maximum of the surface corrugation.

It is assumed that these phonon modes are out-of-plane modes, because of the out-of-plane platelets orientation in case of their appearance and the corresponding interaction with the vertical polarized laser. This speculation is based on the appearance of the in-plane E_{2g} mode, which is only observed for an in-plane grain orientation.

To increase the low TERS intensity under 638 nm excitation, the laser wavelength was changed to 532 nm in conjunction with an Ag tip, thus providing better resonance conditions for the investigation of the VS_2 flake and a better S/N ratio as shown by the spectrum in **Figure 4.6b.** even though the laser intensity was reduced to $\sim 3 \times 10^7$ mW/cm^2 to avoid photo-oxidation.

An extra shoulder beside the A_{1g} mode is observed which corresponds to the silicon (Si) mode of the tip. However, no significant difference in the A_{1g} mode of these two-point spectra is observed. The p2 mode is only seen at the maximum of the ripples (position 1) at 144 cm^{-1} (spectrum 1 in **Figure 4.6b**), where the crystal grain orientation is out-of-plane, and the corresponding TERS map is shown **Figure 4.6f**. This mode has been found in VO_2 and is showing a contamination or possible photo-oxidation. [16] The p3 mode appears more intense and sharper at the minimum of the corrugation (position 2), which can be associated with a more crystalline character. Here, the local crystal grain orientation is in-plane with the substrate (see **Figure 4.3e**). A small blueshift of the p3 mode of 2 cm^{-1} from 168 cm^{-1} at the maximum of the ripples (position 1) to 166 cm^{-1} at the minimum (position 2) can be observed. A summary of the confocal Raman and TERS results for the excitation wavelength 532 nm and 638 nm can be found in **Table 4.2**.

Table 4.2 Summary of the confocal Raman and TERS measurements on the rippled VS$_2$ flakes.

λ_{Laser} (nm)	Mode	Peak position (cm-1)	Observation
Confocal Raman			
532	A1g	324 - 327	red shift for thicker flakes
	E2g	247 - 254	red shift for thicker flakes
	p1	122 - 126	red shift for thicker flakes
	p2	147	appears only for thinner flakes

	p3	167 - 171		red shift for thicker flakes
	p4	188 - 194		indicates vertical flake orientation.
638	A1g	326 - 329		blue shift for thicker flakes
	E2g	-		
	p1	122 - 123		
	p2	-		
	p3	168		only revealed in thicker flakes
	p4	186 - 189		blue shift for thicker flakes
TERS		Max. of grating	Min. of grating	
		vertical grain orientation	in-plane grain orientation	
532	A1g	325 ($w = 14.3$)	325 ($w = 17.7$)	
	E2g	-	-	

	p1	-	125	
	p2	144	-	indicates an oxide formation
	p3	168 (w = 11.7)	166 (w = 7.8)	more intense and sharper at the minimum of the corrugation.
	p4	187	-	
638	A1g	328 (w = 12.9)	327 - 329 (w = 17.5)	
	E2g	-	247 - 251	appears at the minima of the corrugation.
	p1	124 - 125 (w = 13.6)	123 - 124 (w = 2.3)	
	p2	152 - 153	-	
	p3	-	-	
	p4	187	-	mode appears only at the maximum of the corrugation

w = width

In the TERS experiments the focussing of the laser on the apex of cantilever generates a local hot spot through excitation of a plasmon mode of the metal-coated tip. This is

enhancing the local electromagnetic field at the junction between the tip and the sample and subsequently, enhancing the Raman signal. **Figure 4.7a** shows the recorded Raman spectra with the tip direct in contact with the surface (tip-in) and with a certain lift-off (tip-out). The tip-in spectrum carries the near-field + far-field enhancement while the tip-out signal shows only the far-field scattering. The field enhancement depends upon several parameters such as tip geometry, incident excitation, tip-sample distance, and dielectric properties of the sample. The VS_2 shows a metallic character, therefore a quenching of the enhancement is expected.

From **Figure 4.7a** the enhancement factor (EF) is obtained by **equation 1.4**. [17, 18] For these experiments, the EF was estimated to $\sim 1.5 \times 10^2$, indicating the low enhancement due to the metallic character of the VS_2 flake. The spatial resolution of the TERS measurements is estimated from **Figure 4.7**. Therefore, a trench in the topography (**Figure 4.7b**) and TERS map of the A_{1g} mode (**Figure 4.7c**) was analysed. The gaussian fit of the trench in the cross-section reveals a full width at half maximum (FWHM) distance of 60 nm for the topography (**Figure 4.7d**) and 77 nm for the TERS data (**Figure 4.7e**). Such spatial resolution of the TERS map is well below the optical diffraction limit, revealing the advantage of the TERS-technique.
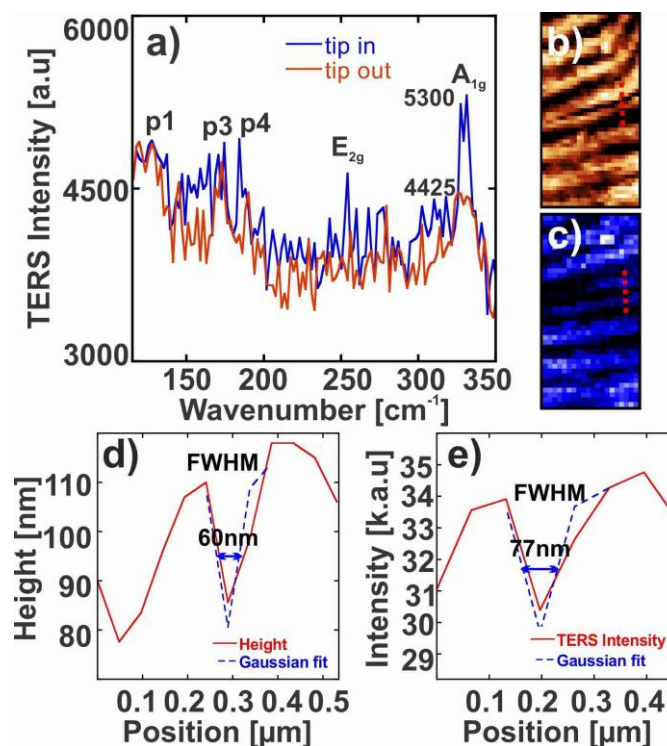
Figure 4.7 TERS enhancement factor and spatial resolution analysis. a) Tip-out (far field) and tip-in (near-field + far-field) TERS spectra used for the EF calculation. The spatial resolution of the TERS setup is estimated from the AFM scan (b) and TERS map of the A_{1g} mode (c) of the rippled VS_2 flake. d) Height cross section, indicated by the red dashed line in b), and gaussian fit. e) TERS cross section obtained from c) and gaussian fit.

4.5 Conclusion

CVD technique is an effective technique to synthesize metallic 1T VS_2 flakes with a flat surface or with the presence of left- and right-handed spiral surface patterns. The formation of the fine structure is caused by a rapid change in the sulfur feeding rate, the precursor ratio (S/VCl$_3$), the temperature and the cooling rate. Without the rapid feeding rate, the spiral structures cannot be observed. The spirals are composed of different oriented small crystallites. The change in orientation of the crystallite domains further shifts the

vibrational modes of the VS$_2$ as determined by TERS and is modulating the work function by 14 meV as measured by KPFM.

Additionally, strains and grain boundaries between the different domains are formed. The modulation of the work function and the surface corrugation is of particular interest for the development of opto-electronic devices, such as solar cells and photodiodes, or could be potentially used in the field of photonics, e.g., as optical resonator or waveguide.

4.6 References

(1) Littlejohn, A. J.; Li, Z.; Lu, Z.; Sun, X.; Nawarat, P.; Wang, Y.; Li, Y.; Wang, T.; Chen, Y.; Zhang, L.; et al. Large Metallic Vanadium Disulfide Ultrathin Flakes for Spintronic Circuits and Quantum Computing Devices. *ACS Appl. Nano Mater.* **2019**, *2* (6), 3684-3694.

(2) Abdul Wasey, A. H. M.; Das, G. P. Electronic and Magnetic Properties of Vanadium Dichalcogenides: A Brief Overview on Theory and Experiment. *J. Appl. Phys.* **2022**, *131* (19), 190701.

(3) Ji, Q.; Li, C.; Wang, J.; Niu, J.; Gong, Y.; Zhang, Z.; Fang, Q.; Zhang, Y.; Shi, J.; Liao, L.; et al. Metallic Vanadium Disulfide Nanosheets as a Platform Material for Multifunctional Electrode Applications. *Nano Lett.* **2017**, *17* (8), 4908-4916.

(4) Hossain, M.; Qin, B.; Sen, S. K. Chemical Synthesis and Substrate Temperature Effect on Morphology of 2D Vanadium Disulfide. *Cryst. Res. Technol* **2021**, *56* (3), 2000184.

(5) Wasey, A. H. M. A.; Chakrabarty, S.; Das, G. P. Quantum Size Effects in Layered VX2 (X = S, Se) Materials: Manifestation of Metal to Semimetal or Semiconductor Transition. *J. Appl. Phys.* **2015**, *117* (6), 064313.

(6) Lee, K.-L.; Chang, C.-C.; You, M.-L.; Pan, M.-Y.; Wei, P.-K. Enhancing the Surface Sensitivity of Metallic Nanostructures Using Oblique-Angle-Induced Fano Resonances. *Sci. Rep.-UK* **2016**, *6* (1), 33126.

(7) Yuan, J.; Wu, J.; Hardy, W. J.; Loya, P.; Lou, M.; Yang, Y.; Najmaei, S.; Jiang, M.; Qin, F.; Keyshar, K.; et al. Facile Synthesis of Single Crystal Vanadium Disulfide Nanosheets by Chemical Vapor Deposition for Efficient Hydrogen Evolution Reaction. *Adv. Mater.* **2015**, *27* (37), 5605-5609.

(8) Hossain, M.; Wu, J.; Wen, W.; Liu, H.; Wang, X.; Xie, L. Chemical Vapor Deposition of 2D Vanadium Disulfide and Diselenide and Raman Characterization of the Phase Transitions. *Adv. Mater. Interfaces* **2018**, *5* (16), 1800528.

(9) Klein, M. V. Theory of Two-Phonon Raman Scattering in Transition Metals and Compounds. *Phys. Rev. B* **1981**, *24* (8), 4208-4223.

(10) Saito, R.; Hofmann, M.; Dresselhaus, G.; Jorio, A.; Dresselhaus, M. S. Raman Spectroscopy of Graphene and Carbon Nanotubes. *Adv. Phys.* **2011**, *60* (3), 413-550.

(11) Venezuela, P.; Lazzeri, M.; Mauri, F. Theory of Double-Resonant Raman Spectra in Graphene: Intensity and Line Shape of Defect-Induced and Two-Phonon Bands. *Phys. Rev. B* **2011**, *84* (3), 035433.

(12) Zólyomi, V.; Koltai, J.; Kürti, J. Resonance Raman Spectroscopy of Graphite and Graphene. *Phys. Status Solidi B Basic Res.* **2011**, *248* (11), 2435-2444.

(13) Liang, H.; Shi, H.; Zhang, D.; Ming, F.; Wang, R.; Zhuo, J.; Wang, Z. Solution Growth of Vertical VS_2 Nanoplate Arrays for Electrocatalytic Hydrogen Evolution. *Chem. Mater.* **2016**, *28* (16), 5587-5591.

(14) Su, J.; Wang, M.; Li, Y.; Wang, F.; Chen, Q.; Luo, P.; Han, J.; Wang, S.; Li, H.; Zhai, T. Sub-Millimeter-Scale Monolayer p-Type H-Phase VS_2. *Adv. Funct. Mater.* **2020**, *30* (17), 2000240.

(15) Maguire, P.; Fox, D. S.; Zhou, Y.; Wang, Q.; O'Brien, M.; Jadwiszczak, J.; Cullen, C. P.; McManus, J.; Bateman, S.; McEvoy, N.; et al. Defect Sizing, Separation, and Substrate

Effects in Ion-Irradiated Monolayer Two-Dimensional Materials. *Phys. Rev. B* **2018**, *98* (13), 134109.

(16) Huang, T.; Yang, L.; Qin, J.; Huang, F.; Zhu, X.; Zhou, P.; Peng, B.; Duan, H.; Deng, L.; Bi, L. Study of the Phase Evolution, Metal-Insulator Transition, and Optical Properties of Vanadium Oxide Thin Films. *Opt. Mater. Express* **2016**, *6* (11), 3609-3621.

(17) He, Z.; Voronine, D. V.; Sinyukov, A. M.; Liege, Z. N.; Birmingham, B.; Sokolov, A. V.; Zhang, Z.; Scully, M. O. Tip-Enhanced Raman Scattering on Bulk MoS2 Substrate. *IEEE J, Sel. Top. Quant.* **2017**, *23* (2), 113-118.

(18) Kumar, N.; Rae, A.; Roy, D. Accurate Measurement of Enhancement Factor In Tip-Enhanced Raman Spectroscopy Through Elimination Of Far-Field Artefacts. *Appl. Phys. Lett.* **2014**, *104* (12), 123106.

Chapter 5

5 Photo-Oxidation from VS$_2$ Tip-Enhanced Raman Spectroscopy Study of Vanadium Oxides Formation

In this chapter, we address the characterization of 1T-VS$_2$ and the formation of different vanadium oxides subproducts from the CVD synthesis. In addition, VS$_2$ 1T phase reveals instability by undergoing transformation to VO$_2$ (A) phase and further oxidation into α-V$_2$O$_5$ through laser ablation. The characterization of VS$_2$ platelets through Raman spectroscopy has led to variable observations due to the chemical instability and photoinduced transformation of VS$_2$. The formation of oxides polymorphs, as the VS$_2$ degrades upon exposure to ambient conditions, the irradiance of the source used for the Raman measurements appears to play an important role yielding either decomposition or further oxidation of the VS$_2$ flakes. In order to understand the interplay between light irradiation and the phase transition of VS$_2$, high spatial resolution tip-enhanced Raman measurements (TERS) were conducted on single flakes. We show how TERS was applied to find vanadium oxide mixtures on the surface of CVD grown flakes.

5.1 AFM, SEM and EDX of VO$_2$

VS$_2$ and VO$_2$ were synthesized through APCVD methods, nucleated in triangular and hexagonal shaped thin flakes. Initially, it was believed that following a salt-assisted method it would be possible to synthesize the 2H-VS$_2$ phase, however analysis revealed the composition of VO$_2$ instead.

For VO$_2$ flakes, a surface morphology difference was observed when using two different salt precursors. **Figure 5.1a** shows a hexagonal shape with a nucleation and growth from the center to the outer edge of the flake. The figure reveals a nucleation accumulation of approximately double the number of layers in the edge compared to the center. **Figure 5.1b** reveals a multi-stacked triangular shaped flake, the growth difference of both **Figure 5.1a** and, **b** is attributed to the different salt precursors (KCl and KI, respectively) used in the synthesis method. While switching the salt precursors, both cases (flakes in **Figure 5.1a,**

b) using the main V_2O_5 as the initial precursor, show the influence of the salt type in the nucleation growth of the VO_2 crystals.

The topography cross sections shown in **Figure 5.1c, d** indicate the height profile corresponding to the cross sections shown in **Figure 5.1a, b**, respectively.

Height profile shown in **Figure 5.1c** reveals that the flake has a thickness varying between 24 nm and 44 nm. VO_2 usually grows in nanotubes and ribbons through vapor transport techniques with one-layer thickness of approximate 0.62 nm. Therefore, from our cross-section measurements, we determine that there are ~40 layers for the 24 nm thick area and ~73 layers for the 44 nm thick central area. [1-3] On the other hand, the thickness of the triangles in **Figure 5.1b** was determined to be from 34 to approximately 81 nm, which corresponds to 55-131 layers, respectively.
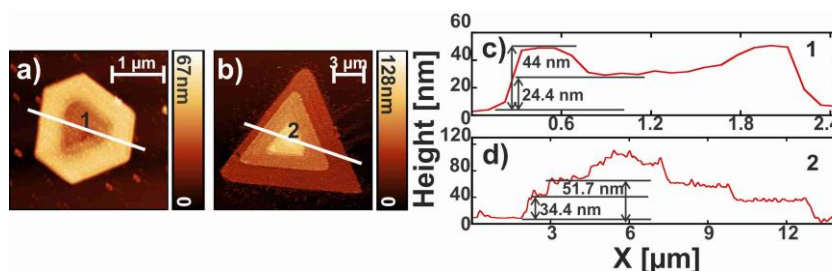
Figure 5.1 a, b) AFM scan of hexagonal and triangular VO_2. Height profiles of flakes corresponding to cross sections 1 (c) ,2 (d), from a, and b AFM scans.

SEM micrographs of VO_2 and VS_2 product can be observed in **Figure 5.2**. **Figure 5.2a** and **b** show ultra-thin flakes of VO_2 grown on mica. A film of VS_2 crystallites, shown in **Figure 5.2c**, was synthesized by increasing the H_2 flow. **Figure 5.2d** shows the bulk VS_2 with a layered and axial growth predisposition. Overall, the crystal growth of VS_2 and VO_2 varied in lateral dimensions, displaying mostly dimensions of 2 µm or less for VO_2 and a maximum of 3 µm for VS_2.
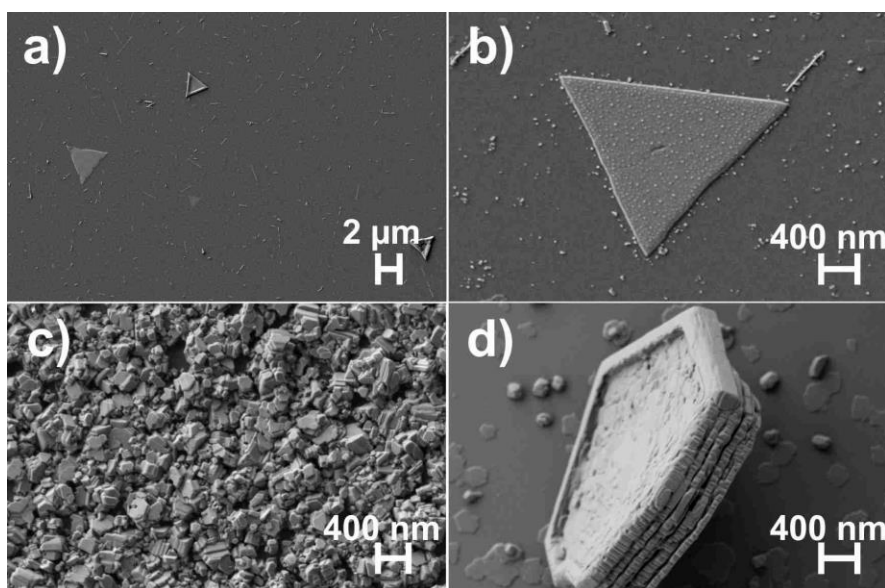
Figure 5.2 SEM micrographs corresponding to a, b) VO₂ crystal on mica c) VS₂ crystallites film and polymorphs on SiO₂/Si. d)1T-VS₂ phase crystal layered on mica.

EDX results of the samples shown in **Figure 5.2** are summarized in **Table 5.1**. **Figure 5.2a, b** reveals a weight composition close to VO_2 with absence of sulfur, which suggests that the triangles are VO_2, not VS_2.

For the crystallite film, the weight composition is of 21.6 % vanadium, 13.3% sulfur and 15.3% oxygen. These results indicate the presence of oxides presumably mixed with sulfides in addition caused by the substrate. The crystal shown in **Figure 5.2d** has an elemental composition closest to a 1T-VS_2 phase. All other elements that are present may be caused by the mica substrate.

Table 5.1 EDX analysis results

Product in Figure 5.2	Elements	Composition Weight%
a, b	V (Kα)	18.6%
	O (Kα)	40.0%
	F (Kα)	12.0%
	Mg (Kα)	10.8%

	Al (Kα)	3.86%
	Si (Kα)	11.3%
	K (Kα)	3.48%
c	V (Kα)	21.6%
	S (Kα)	13.3%
	O (Kα)	15.3%
	Si (Kα)	49.9%
d	V (Kα)	28.6%
	S (Kα)	44.8%
	C (Kα)	10.0%
	O (Kα)	13.7%
	F (Kα)	0.67%
	Mg (Kα)	0.80%
	Al (Kα)	0.48%
	Si (Kα)	0.79%
	K (Kα)	0.24%

AFM scans and SEM/EDX were acquired immediately after synthesis. Further observations on the same crystals highlights that oxidation over VS_2 flakes was observed after 1 month. Over time, small particles develop over the flake samples which were attributed to further oxide formation. The preferential geometry of growth of VS_2 is still under study as it can be attributed to several factors including nucleation, thermodynamics, and diffusion of the TMDs.[25] Additionally, the growth of these crystals will depend on the gas flow parameters, the position in the furnace (downstream) and substrate nucleation sites.

5.2 Raman Spectroscopy of Vanadium Oxides

Raman spectra of the vanadium oxides polymorphs and vanadium sulfide were acquired using 532 nm as the excitation and a power of 0.9 mW at the sample was used in standard

confocal conditions (spot size at the focal plane ~1μm^2, Irradiance ~9×10^4 W/cm^2).The Raman modes and assignments from the references described in this manuscript are summarized in **Table 5.2.** The most common and reproducible results appeared when the VCl$_3$ and S were used as precursors. Oxide formation was also observed in some cases depending on the flow of H$_2$ and whether the precursor (VCl$_3$) may have been slightly oxidized into VClO when exposed to moist air in ambient conditions. By exchanging the salts, ultra-thin triangular and hexagonal structures were obtained and correspond to VO$_2$ as identified by Raman and EDX. The studies made by Su[4] and Littlejohn[5] used inert environment for the characterization preventing excessive oxidation. Moreover, in some cases it was recommended to add another ramp, from room temperature to 150°C, in the synthesis recipe to break any oxygen bonds from VClO while purging the system due to the VCl$_3$ precursor instability upon moist and ambient conditions. V$_2$O$_5$ precursor is not recommended for the synthesis of VS$_2$ in conjunction with KI salt. Instead, several tries were attempted following Zhou *et al*. study[6] using VCl$_3$ along with argon and hydrogen.

The Raman spectra of the different crystals obtained are shown in **Figure 5.3**. Red spectrum (1) in **Figure 5.3a** shows modes that followed the same synthesis method as 2H-VS$_2$, however A$_{1g}$ and E$_{2g}$ modes that were supposed to be observed at 404 and 384 cm^{-1}, respectively, were absent. E$_{2g}$ 2H-VS$_2$ mode was shifted more than 6 cm^{-1} while A$_{1g}$ mode was not present in the spectrum (**Table 5.2**), which contrasted with published work. It is hypothesized that the mass transportation of the gaseous precursor (S and V$_2$O$_5$) and decomposition of the V$_2$O$_5$ (into VO$_2$) forming the reaction on the surface of the substrate were limited. Addition of molten salt (KCl) into the reaction promotes oxyhalides that decrease melting points to initiate the reaction at lower temperature, [7] nevertheless, no kinetic study has been previously reported revealing the feasibility and stability for this reaction to occur. Assignments in **Table 5.2** reveal a probable mixture of V$_2$O$_5$ and VS$_2$, which agrees with EDX results (certain amount of oxygen is present in the product as shown in **Table 5.1**).

Figure 5.3a black spectrum (2) shows a pure 1T-VS$_2$ phase crystal that has the different modes assigned in **Table 5.2**, revealing the reproducibility of work previously reported. [8, 9] Inset optical image is shown for each of the corresponding spectra, revealing the nature of hexagonal structure for this crystal. It was revealed by Zhou *et al.* [6] that KI could be used to promote the synthesis of 1T-VS$_2$. However, it was determined once more as shown in **Figure 5.3a** blue spectrum (3), the characterization of vanadium oxides mixture of VO$_2$ and V$_2$O$_5$ determining the lack of sulphuration during the reaction. Furthermore, large 2D crystal layers were formed that may have been caused by the addition of the KI molten salt despite not previously observed using KCl salt.

The spectra 1-3 shown in **Figure 5.3b** correspond to VO$_2$ (A) phase, VO$_2$ (M1) and α-V$_2$O$_5$, respectively. For **Figure 5.3b**, spectra 1 and 2 indicate that oxide formation took place because of the VCl$_3$ oxidization process generated VClO compound, making it almost impossible to promote the VS$_2$ reaction. Crystals corresponding to the red spectrum in **Figure 5.3b** as shown as an inset, is iridescent and their Raman spectra are typically associated with a α-V$_2$O$_5$ phase with the presence of A$_g$ and B$_g$ phonon modes. Finally, the spectrum associated with **Figure 5.3b** plot 3 corresponds to a VO$_2$ (M1) phase.

Table 5.2 Raman vibrational modes assignments of VS$_2$, VO$_2$, V$_2$O$_5$ polymorphs

Spectra shown in Fig.5.3	Precursors and parameters	Raman wavenumber (Cm^{-1})	Assignment	Reference
a1	V$_2$O$_5$+S+KCl	130.7	Phonon 1T-VS$_2$	[4, 5, 10]
		167.9	Phonon 1T-VS$_2$	
	10 sccm H$_2$	233.9	B$_g$ β -V$_2$O$_5$	
	50 sccm Ar	276.3	E$_{2g}$ VS$_2$ 1T	
		356.7	A$_g$ β-V$_2$O$_5$	
		377.6	E$_{2g}$ 2H-VS$_2$/ A$_g$ 1T-VS$_2$	
a2	VCl$_3$+S	129.3	Phonon 1T-VS$_2$	[8, 9, 11]

		167.2	Phonon 1T-VS$_2$	
	20 sccm H2	274.4	E$_{2g}$ 1T-VS$_2$	
	80 sccm Ar	326.0	A$_{1g}$ 1T-VS$_2$	
a3	V$_2$O$_5$+S+KI	151.5	Phonon 1T-VS$_2$ / V$_2$O$_5$	[10]
		194.5	A$_g$ M1-VO$_2$	
	10 sccm H$_2$	301.0	-	
	80 sccm Ar	355.0	Ag α-V$_2$O$_5$	
		682.0	Mica substrate	
		892.0	-	
b1	VCl$_3$+S	199.0	Mica substrate	[10]
		280.0	Mica substrate	
	4 sccm H$_2$	334.0	A$_{1g}$ 1T-VS$_2$ / Ag α-V$_2$O$_5$	
	90 sccm Ar	406.0	Ag α-V$_2$O$_5$	
		551.0	α-V$_2$O$_5$/ Al$_2$O$_3$	
		682.0	Mica substrate	
b2	VCl$_3$+S	143	Ag α-V$_2$O$_5$	[10]
		199.6	Mica substrate	
	4 sccm H$_2$	279.1	Mica substrate	
	90 sccm Ar	403.2	Ag α -V$_2$O$_5$	
		602.8	-	
		678.6	Mica substrate	
b3	V$_2$O$_5$+S+KI	138.0	Ag M1-VO$_2$	[10, 12]
		184.0	Ag M1-VO$_2$	
	10 sccm H$_2$	289.0	A-VO$_2$/B$_{1g}$, B$_{3g}$line α -	
	50 sccm Ar	343.0	V$_2$O$_5$	
		874.0	Ag M1-VO$_2$	
			Amorphous VO$_2$-VO$_2$	
			oxidation	
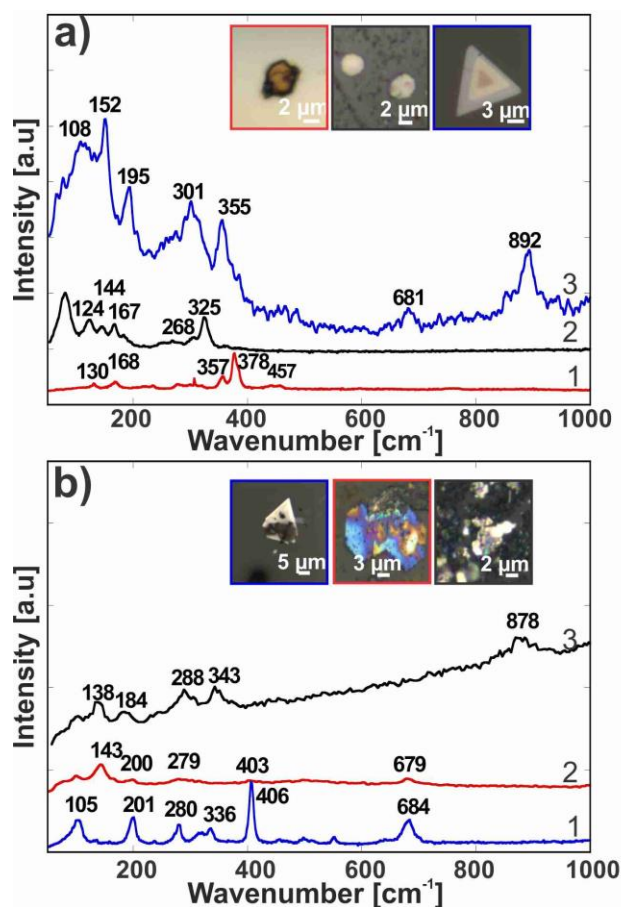
Figure 5.3 a) Raman spectra of the different samples described in Table 5.2, 1) Red spectrum was conducted on a mixture of VOx, 2) Black spectrum is associated with the 1T-VS$_2$ phase and 3) Blue spectrum is a mixture of VO$_2$ and V$_2$O$_5$. b) Raman spectra of the different synthesis trials described in Table 5.2, 1) Blue spectrum is a mixture of α-V$_2$O$_5$ and VS$_2$ 2) Red spectrum was performed on α-V$_2$O$_5$ and 3) spectrum (black) of M1-VO$_2$. Raman spectra are complemented with the optical images of the corresponding samples.

5.3 Promoted Photo-Oxidation from VS$_2$

To determine a possible photoinduced oxidation process, flakes were irradiated under distinct energies using a 638 nm laser excitation focused onto a ~1 µm^2 surface (**Figure 5.4a**). At first Raman spectrum (blue) was acquired after irradiation of 2.5 mW (Irradiance

2.5×10^5 W/cm^2) during 200 seconds revealing a stable 1T-VS$_2$. Increasing the power, spectra with less features were collected as shown by the black and red spectra in **Figure 5.4a** under 6.25 mW (Irradiance 6.25×10^5 W/cm^2) and acquisition time of 40 s and 100 s, respectively. These spectra correspond VO$_2$ phase. Under 6.25 mW and longer irradiation time (200 s), the spectrum shows new features highlighting the presence of both VO$_2$ and V$_2$O$_5$. As the irradiation increases the phase transition from VO$_2$ to VO$_2$+V$_2$O$_5$ occurs at an increase of energy from 0.63 joules (red spectrum) to 1.25 Joules (green spectrum). This oxidation process was observed in most flakes with an immediate optical change both in the morphology and color of the flakes as observed in **Figure 5.4b-g**. After reaching 1.13 joules of energy α-V$_2$O$_5$ was obtained (shown in green of **Figure 5.4a**) which is most likely a mixture of phases. As mentioned in the introduction, VO$_2$ has a MIT property that switches back and forth depending on its temperature once it reaches over 68 °C, after which it anneals into an unreversible α-V$_2$O$_5$ compound.

Figure 5.4b, c corresponds to optical images taken while acquiring the Raman spectra shown in **Figure 5.4a** at 0.50 and 0.65 joules (blue and red). **Figure 5.4d, e** corresponds to a flake that was initially VO$_2$ and further oxidized to V$_2$O$_5$. Noteworthy, the same coloration of the optical image is shown in **Figure 5.3b** plot 2, revealing a complete transformation from VO$_2$ to α-V$_2$O$_5$. To evaluate if the mica substrate was possibly involved in the photon-oxidating process, irradiation of the flakes under distinct power was performed using a SiO$_2$/Si substrate. Both substrates are insulators however mica should have a bandgap of approximately 7.85 eV while SiO$_2$/Si should be approximately 8.9 eV. **Figure 5.4f, g** reveal the optical transition of VS$_2$ to VO$_2$ using SiO$_2$/Si as substrate. It was hypothesized that the interaction with the substrate has a mayor impact in the charge distribution and thermal distribution of the flake. These observations indicate that even though the results over oxidation were the same as found in flakes b and c deposited on mica, the thermal effects appear more prominent over SiO$_2$/Si substrates.

In addition to the measurements conducted at 638 nm, the Raman spectra were acquired in confocal mode using 532 nm as the excitation. The power was set successively at 0.9 mW

$(9 \times 10^4$ W/cm^2) with 300 s acquisition time and 9 mW $(9 \times 10^5$ W/cm^2) with a much shorter acquisition time of 3 s. These acquisition times were critical and longer acquisition under both irradiances resulted in the presence of a mixture of VO$_2$ and V$_2$O$_5$. For shorter acquisition times the Raman spectra of VS$_2$ remains stable. A slower transition was observed at 638 nm excitation, as expected since VS$_2$ is less resonant at 638 nm than at 532 nm. Interestingly, less fluorescence background was observed using 532 nm as compared to measurements done at 638 nm.
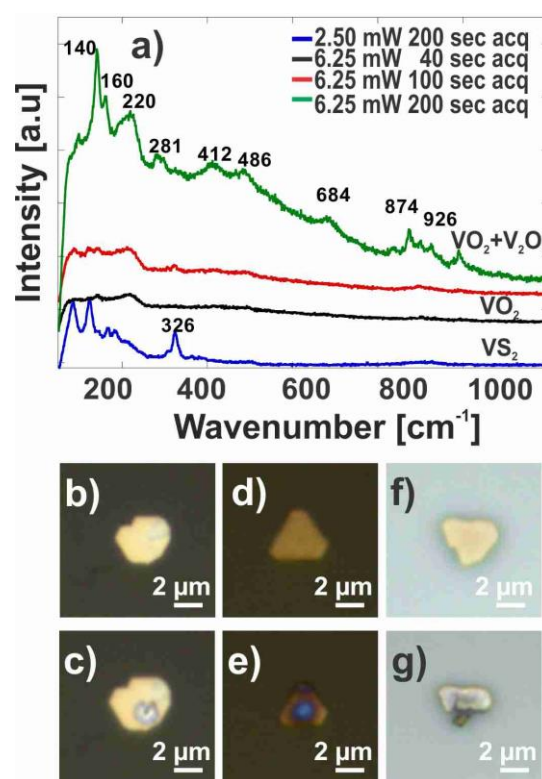
Figure 5.4 a) Raman spectra of the induced oxidation of VS$_2$ under distinct power and irradiation time, b, c) Optical transition from VS$_2$ to VO$_2$ on mica substrate. d, e) Optical transition from VO$_2$ to V$_2$O$_5$ on mica substrate. f, g) Optical transition from VS$_2$ to VO$_2$ on SiO$_2$/Si substrate.

5.4 TERS of Vanadium Oxides Mixtures.

To understand better the oxidation process, TERS was used to correlate the Raman spectra with the topography of the flakes. **Figure 5.5a** shows the topography of a portion of a VS_2 flake onto the as-grown mica substrate. The TERS experiments were acquired with a wavelength of 532 nm and with a power of 9 mW focused onto a ~$2\mu m^2$ area on the sample (Irradiance of 4.5×10^5 W/cm^2). This translates into a power of ~22.6 µW below the coated tip which has a typical diameter of ~80 nm. In these experiments, we used commercial OMNI TERS FM (Ag) probes (Ag coating of about 300 nm) that are coated with a thin ~10 nm protective Au layer to protect Ag from oxidation. Plasmon modes of Ag nanostructures are usually reported to be more efficient when excited with 532 nm. In addition, the incident 532 nm excitation was selected to minimize the background fluorescence from the mica substrate which is significant under 638 nm excitation.

In these experimental conditions, the collected spectra appear to reveal oxidation of the VS_2 flakes during the mapping even though a short acquisition time was used (150 ms per pixel). The local oxidation may be enhanced by the LSPR confined at the extremity of the tip that can presumably induces modest local temperature changes at the tip-sample junction that can be sufficient to promote the oxidation of the VS_2 flakes. [13]
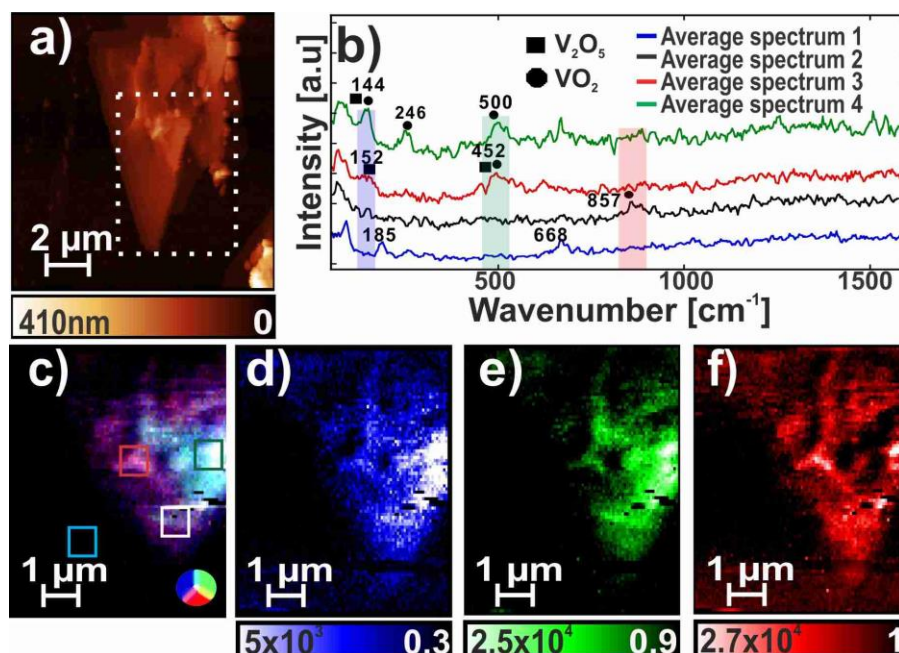
Figure 5.5 a) AFM scan of the topography of flake. b) Average TER spectra collected at different areas. c) TERS all colored map revealing average area shown in b. d) TERS map corresponding to the integration of the [113-193] cm^{-1} region with TERS intensity range of 0.3-5×10^3 arbitrary units. e) TERS map corresponding to the integration of the [453-572] cm^{-1} region with TERS intensity of 0.9 - 2.5×10^4 arbitrary units. f) TERS map corresponding to the integration of the [796-932] cm^{-1} region TERS intensity range of 1-2.7×10^4 arbitrary units.

TERS experiments were conducted on a selected flake with topography shown in **Figure 5.5a.** The representative TERS spectra are shown in **Figure 5.5**b and are collected from different areas indicated in **Figure 5.5c**. These spectra were obtained by averaging 100 TERS spectra. Spectrum 1 corresponds to a zone represented by the blue square outside the flake and shows modes at 91, 185, 258, 308 and 672 cm^{-1} that correspond to the mica substrate. Spectrum 2 (white square in **Figure 5.5c**) displays only one mode at 857 cm^{-1} associated with VO$_2$ (B) phase and to the V=O stretching mode of an octahedra structure. [14] This mode might be related to the strong-spin interaction at the phase structure transition occurring due to the thermal laser excitation. The red area **(Figure 5.5c)** corresponding to

spectra 3 displays 152, 352, 500 and 617 cm^{-1} modes. The mode at 152 cm^{-1} is related to V_2O (B) where the V-O-V is associated with stretching or bending mode. In addition, the latter mode has also been associated with V_2O_5, these modes are determined by vibrational shear and sliding motion of VO_5-VO_5 atomic chains of the compound. [10, 15] The spectral width of these modes may be attributed to the loss of crystallinity on that area of the flake. α-V_2O_5 B_{2g} mode at 352 cm^{-1} can be observed due to breathing oscillations of the chains that occur along an α-axis. Nevertheless, the small intensity reveals a probable mixture and crystallinity loss as well. The 452 cm^{-1} mode is assigned to the VO_2 mode and has been previously resolved experimentally using Al_2O_3 substrate. [16] In addition, the mode is also observed on M2-VO_2 phase showing a similar tendency to α-V_2O_5. Different phases generate vibrational modes in the range of 614 to 619 cm^{-1} for VO_2 so it is uncertain which specific phase this mode can correspond to, nevertheless the broadening of the mode indicates a loss of crystallinity.[17] The average green spectra in **Figure 5.5b** and corresponding zone in **Figure 5.5c** shows significant spectral shift and enhancement. It reveals a shift of approximate 8 cm^{-1} for the 152 cm^{-1} mode indicating a crystalline VO_2 (M1). Other modes such as 246 and 500 cm^{-1} (A_g phonon M1-VO_2) show a shift of more than 50 cm^{-1} from the previous average spectrum. This determination may be attributed to the thickness of the flakes, at the edge starting from 35 nm and average spectra revealing an approximate thickness of 50-70 nm while the last average spectrum 4 is taken at a thickness of approximate 130 nm which is characteristic of a bulk nature VO_2 (M1), nevertheless the mode at 144 cm^{-1} can be attributed as well to V_2O_5 as previously mentioned.

From the collected spectra we observe an increase in the TERS intensities of all three bands on the wrinkled areas and locations where strains are found. This is expected since there is an increase in the electric field as well as a change in the orientation of the material in those sectors. It was shown in previous studies in TMDs that straining the flakes will distort and broaden phonon modes with large spectral shifts. [18]

Selection and integration of 3 modes from the spectra (highlighted band regions in **Figure 5.5**b as blue, green, and red) were acquired to generate the TERS maps shown in **Figure 5.5d-f**. The colored maps correspond to the **Figure 5.5d** [113-193] cm^{-1} (blue map), **Figure 5.5e**[453-572] cm^{-1} (green map) and **Figure 5.5f** [796-932] cm^{-1} (red map) spectral regions respectively.

According to the results observed the flake reveals a mix of VO$_2$ phases characteristic of a bulk flake. The morphology and TERS results indicate the amorphous sites of the flake indicating an in-homogenous flake growth. The TERS blue map shown in **Figure 5.5d** indicates the mode associated with VO$_2$ or V$_2$O$_5$ composition, while it shows a higher TERS intensity of 0.3 - 5$\times$10^3 arbitrary units in comparison to the other modes integrated. Furthermore, the intensity contrast distribution in the map shows that the mode is most intense where there is an increase in the layers and when comparing to the topography found in **Figure 5.5a**. The green map observed in **Figure 5.5e** is most likely a mix of modes coming from VO$_2$ and V$_2$O$_5$, its TERS intensity ranges from 0.9 - 2.5$\times$10^4 showing a better resolution of the strains position in the overall surface of the flake. The last which is the red map chosen by integrating a VO$_2$ (B) phase mode which has an intensity of 1 - 2.7$\times$10^4, reveals crisper details over the surface of the flake such as grain like strains that are smaller. This may be attributed to the semi-metallic character found in VO$_2$ compounds.

Inhomogeneous broadening of the modes may be expected due to amorphous sites within the flake and change in the environment, nevertheless the TERS results show consistency in the characteristic results for oxide mixture and the spectral shift of specific sites over the surface indicating the different crystalline phases and amorphous sites. Results reveal that surface shows a semi-metallic property except in the location where several layers are present. The property presented in the VO$_2$ compound is attributed to faster acquisition of the map, to avoid the photo-oxidation.

To further reveal the enhancement and confirmation of TERS a comparison near field versus far field (tip in versus out) was accomplished. Measurements were performed using 5 second acquisition for both tip in and out under the same parameters of laser excitation

and grating. The greater the energy by changing acquisition time, the more visible damage over the flake was observed. **Figure 5.6** reveals the enhancement specifically of the B_{1g} and the B_{2g} modes at 149 and 286 cm^{-1}, respectively, that are characteristic of α-V_2O_5 mode. [19] However the modes show a spectral shift compared to references, that is attributed to the plasmonic resonances. The mode B_{1g} at 149 cm^{-1} shows a shift of 4 cm^{-1} towards higher wavenumbers when comparing to the 145 cm^{-1} found in literature for bulk crystals of V_2O_5. [20] Furthermore, the B_{2g} mode shows a shift of 2 cm^{-1} also towards a higher wavenumbers region. This reveals that there is an interaction between the metal tip and the insulator V_2O_5 under 532 nm excitation. TERS has been previously reported in 1D nanorod VO_2, polarization studies showed transition of M1 and M2 phases however no R (metallic) phase was confirmed, this indication reveals that we had mixtures of VOx components in our flakes. [3] These spectral shifts differ from the micro-Raman measurements. When acquiring the near- and far-field spectra, the increased acquisition time has presumably promoted a photon-oxidation reaction and resulting damages occurred in a part of the flake changing the surface roughness and generating particles. For TERS mapping new flakes were chosen to avoid photon-oxidation and by changing to faster acquisition time.
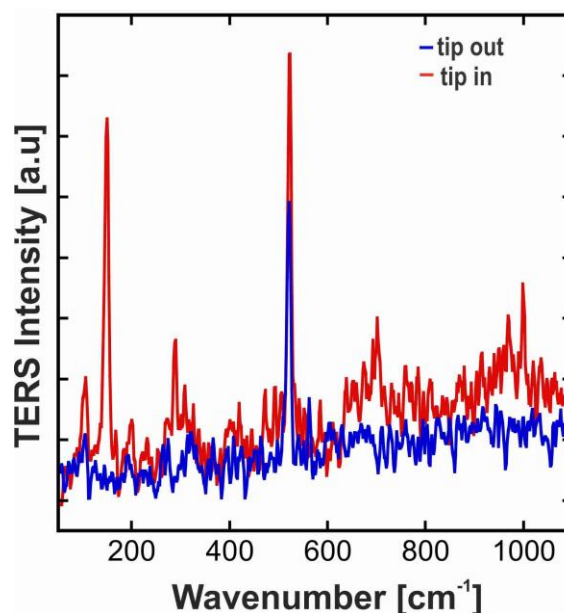
Figure 5.6 TERS intensity showing near field (tip in) versus tip out (far field).

Using the FWHM of the TERS signal our experiments revealed a spatial resolution of ~ 80 nm over maps exceeding 10 μm × 10 μm surfaces. This spatial resolution surpasses diffraction limited measurements and is adapted to these thin flakes providing the possibility to spectroscopically identify nanoscale features such as edges, strains, and particles located over the map.

5.5 Conclusions

In this chapter, we have reviewed and compared our results to previous synthesis of 1T-VS$_2$ performed in APCVD conditions. APCVD synthesis of 1T-VS$_2$ ambient conditions will promote polymorphs. Raman spectroscopy was used to determine the characterization difference between the TMDs and oxide formation. It was found that VO$_2$ (M1), (A), (R) phases and the α-V$_2$O$_5$ appear in some cases. This highlights the difficulties promoting the reaction of VS$_2$ using a V$_2$O$_5$ precursor. Raman spectra further revealed the transition occurring to the VS$_2$ oxidizing into VO$_2$ for increased laser power. A clear change in the surface and color morphology of the flakes occurred at the end of the transition when incident energy reached 1.13 joules.

TERS data unveils strains that affect the VO$_2$ phase transition in the form of spectral shifts at different locations of two different flakes. The mixture of different oxides such as V$_2$O$_5$, VO$_2$ and different phases were observed on bulkier areas and strains generating in some cases amorphous sites. The energy associated to the local surface plasmon resonance and the coupling between the coated tip (plasmon) and insulator (VO$_2$) generate a slight enhancement. Spectral shifts associated with the mica substrate are indicative of the strong plasmonic interaction between the Au-coated tip and the and the TMD flake. TERS maps in combination with the associated spectra provides a spatially resolved snapshot of the distribution of VO$_2$ and oxide mixtures with a spatially resolution better than 100 nm.

5.6 References

(1) Basu, R.; Patsha, A.; Chandra, S.; Amirthapandian, S.; Karkala Gururaj, R.; Dasgupta, A.; Dhara, S. Polarized Tip-Enhanced Raman Spectroscopy in Understanding Metal-to-Insulator and Structural Phase Transition in VO2. *J. Phys. Chem. C* **2019**, *123* (17), 11189-11196.

(2) Xia, C.; Lin, Z.; Zhou, Y.; Zhao, C.; Liang, H.; Rozier, P.; Wang, Z.; Alshareef, H. N. Large Intercalation Pseudocapacitance in 2D VO$_2$ (B): Breaking through the Kinetic Barrier. *Adv. Mater.* **2018**, *30* (40), 1803594.

(3) Basu, R.; Patsha, A.; Chandra, S.; Amirthapandian, S.; Karkala Gururaj, R.; Dasgupta, A.; Dhara, S. Polarized Tip-Enhanced Raman Spectroscopy in Understanding Metal-to-Insulator and Structural Phase Transition in VO$_2$. *J. Phys. Chem. C* **2019**, *123* (17), 11189-11196.

(4) Su, J.; Wang, M.; Li, Y.; Wang, F.; Chen, Q.; Luo, P.; Han, J.; Wang, S.; Li, H.; Zhai, T. Sub-Millimeter-Scale Monolayer p-Type H-Phase VS$_2$. *Adv. Funct. Mater.* **2020**, *30* (17), 2000240.

(5) Littlejohn, A. J.; Li, Z.; Lu, Z.; Sun, X.; Nawarat, P.; Wang, Y.; Li, Y.; Wang, T.; Chen, Y.; Zhang, L.; et al. Large Metallic Vanadium Disulfide Ultrathin Flakes for Spintronic Circuits and Quantum Computing Devices. *ACS Appl. Nano Mater.* **2019**, *2* (6), 3684-3694.

(6) Zhou, J.; Lin, J.; Huang, X.; Zhou, Y.; Chen, Y.; Xia, J.; Wang, H.; Xie, Y.; Yu, H.; Lei, J.; et al. A Library of Atomically Thin Metal Chalcogenides. *Nature* **2018**, *556* (7701), 355-359.

(7) Manukyan, K. V.; Kirakosyan, K. G.; Grigoryan, Y. G.; Niazyan, O. M.; Yeghishyan, A. V.; Kirakosyan, A. G.; Kharatyan, S. L. Mechanism of Molten-Salt-Controlled Thermite Reactions. *Ind. Eng. Chem. Res.* **2011**, *50* (19), 10982-10988.

(8) Hossain, M.; Qin, B.; Sen, S. K. Chemical Synthesis and Substrate Temperature Effect on Morphology of 2D Vanadium Disulfide. *Cryst. Res. Technol.* **2021**, *56* (3), 2000184.

(9) Yuan, J.; Wu, J.; Hardy, W. J.; Loya, P.; Lou, M.; Yang, Y.; Najmaei, S.; Jiang, M.; Qin, F.; Keyshar, K.; et al. Facile Synthesis of Single Crystal Vanadium Disulfide Nanosheets by Chemical Vapor Deposition for Efficient Hydrogen Evolution Reaction. *Adv. Mater.* **2015**, *27* (37), 5605-5609.

(10) Shvets, P.; Dikaya, O.; Maksimova, K.; Goikhman, A. A Review of Raman Spectroscopy of Vanadium Oxides. *J. Raman Spectrosc.* **2019**, *50* (8), 1226-1244.

(11) Hossain, M.; Wu, J.; Wen, W.; Liu, H.; Wang, X.; Xie, L. Chemical Vapor Deposition of 2D Vanadium Disulfide and Diselenide and Raman Characterization of the Phase Transitions. *Adv. Mater. Interfaces* **2018**, *5* (16), 1800528.

(12) Vilanova-Martínez, P.; Hernández-Velasco, J.; Landa-Cánovas, A. R.; Agulló-Rueda, F. Laser Heating Induced Phase Changes of VO_2 Crystals In Air Monitored by Raman spectroscopy. *J. Alloy Compd.* **2016**, *661*, 122-125.

(13) Downes, A.; Salter, D.; Elfick, A. Heating effects in tip-enhanced optical microscopy. *Opt. Express* **2006**, *14* (12), 5216-5222.

(14) Shaohong, Z.; Juan, F.; Qiucheng, S.; Liangpeng, W.; Xinjun, L. In Situ Characterization on Thermal Transitions of $VO_2(B)$: Toward $VO_2(R)$ and V_2O_3. *Rare Metal Mat. Eng.* **2016**, *45* (6), 1374-1380.

(15) Parmar, R.; de Freitas Neto, D. B.; Matsubara, E. Y.; Gunnella, R.; Rosolen, J. M. Electro-insertion of Mn2+ ions into $V_2O_5 \cdot nH_2O$ on MWCNTs coated carbon felt for binder-free Na+ ion battery electrodes. *Sustain. Energy Fuels* **2020**, *4* (8), 3951-3962.

(16) Ureña-Begara, F.; Crunteanu, A.; Raskin, J. P. Raman and XPS characterization of vanadium oxide thin films with temperature. *Appl. Surf. Sci.* **2017**, *403*, 717-727.

(17) Zhou, Y.; Xu, Q.; Ge, T.; Zheng, X.; Zhang, L.; Yan, P. Accurate Control of VS_2 Nanosheets for Coexisting High Photoluminescence and Photothermal Conversion Efficiency. *Angew. Chem. Int. Edit.* **2020**, *59* (8), 3322-3328.

(18) Yang, S.; Chen, Y.; Jiang, C. Strain engineering of two-dimensional materials: Methods, properties, and applications. *InfoMat* **2021**, *3* (4), 397-420.

(19) Dhananjaya, M.; Prakash, N. G.; Narayana, A. L.; Hussain, O. M. Microstructural and Supercapacitive Properties of One-Dimensional Vanadium Pentoxide Nanowires Synthesized by Hydrothermal Method. *Appl. Phys. A-Mater.* **2018**, *124* (2), 185.

(20) Su, Q.; Huang, C. K.; Wang, Y.; Fan, Y. C.; Lu, B. A.; Lan, W.; Wang, Y. Y.; Liu, X. Q. Formation of Vanadium Oxides with Various Morphologies by Chemical Vapor Deposition. *J. Alloy Compd.* **2009**, *475* (1), 518-523.

Chapter 6

6 Hidden layers of TMDs WS$_2$ Semiconductor Characterized Through TERS

In this Chapter, we investigate the formation of a flower-like structure that grows over the surface of a WS$_2$ semiconductive flake grown by CVD. This secondary structure cannot be clearly identified by topography measurements and the phase image was key to reveal this secondary structure with excellent resolution and contrast. Furthermore, Raman measurements conducted in confocal and in TERS modes provide excellent optical contrast to differentiate the different domains of this secondary structure based on the change of intensity of the lattice vibrations. In addition, nanomechanical measurements using the advanced modes force modulation (FMM) and Peak Quantitative Nanomechanics (QNM) were used to understand the origin of the hidden flower. The cantilever torsion in the FMM indicates a reduced friction force within the fine surface structure meanwhile the change in the amplitude and phase of the FMM experiments displays the hidden flower from which is concluded that also the Young's modulus differs in these domains. QNM technique shows that the adhesion force is reduced in these domains. Last, Kelvin Probe Force Microscope (KPFM) measurements reveal a change of the electrical properties within these domains. The correlation of these nanomechanical and nanoelectrical measurements conducted at the scale of a single flake together with the spatially resolved Raman mapping provided the necessary data to understand the growth of this secondary structure.

6.1 Growth of WS$_2$ Flakes

The height of WS$_2$ monolayer is typically of 0.65 nm. Between the WS$_2$ monolayers only weak van der Waals interactions exist, due to the passivated surface, which prevents the monolayer from bonding with the neighbouring plane and permits the mechanical exfoliation. The stacking of 1H layers can result in a hexagonal symmetry (2H phase, semiconductor) or rhombohedral symmetry (3R phase, semiconductor). [1]

For the specific case of WS_2, two pathways involving the nucleation and the subsequent growth are generally discussed. The smooth and passivated surface usually prevents the 2D material to directly nucleate. Therefore, the primary mechanism involves the direct nucleation around a localized defect over the substrate which is then followed by the lateral growth of the single layer crystal. [2] The second proposed mechanism involves the formation of nanoparticles, e.g., WO_3, which is followed by the formation of a layered material shell and further lateral growth. [3, 4] The lattice structure of the substrate itself has an important influence on the growth and orientation of the WS_2. So far crystals were grown on Si/SiO_2, graphene and Au surfaces. The crystals grown on Si/SiO_2 show a random orientation. [5, 6]

Furthermore, the WO_3/S ratio and the S introduction time has a large influence on the growth and the shape of the WS_2 flakes. [7] In general, the WS_2 flake shows a hexagonal shape with alternating S and W terminated edges. Increasing the sulfur concentration results in a faster growth of the W terminated edges. In consequence these edges become shorter with time which is finally forming the triangular shape of the WS_2 flakes. [8]

 Increasing the exposure time of the flake to the sulfur leads to larger flakes. In general, the formation of the WS_2 crystals is quite complex and depends additionally on the generation of defects and lattice mismatches, which results in a core-shell growth[4, 9] and screw dislocation. [10, 11] In addition, hexagonally shaped flakes with a heterostructure of sulfur- and tungsten vacancies were reported. [12-18] Those vacancies were revealed by photoluminescence (PL) and Raman spectroscopy or labeling with a fluorophore. [19] The understanding of the formation of such peculiar structures is therefore critical for the future application of these materials. The WS_2 flakes were grown on a silicon substrate coated with a 280 nm silicon dioxide layer by atmospheric pressure CVD in a single zone tube furnace using a solid source (tungsten trioxide (WO_3) and sulfur (S)) as described in Chapter 2, experimental methods.

6.2 Topography and Optical Microscopy of WS$_2$

The WS$_2$ flakes were first imaged with an AFM operating in intermittent contact mode. The amplitude and the phase of this oscillation are changing during the scanning due to the tip-sample interaction. The change in the amplitude reveals topographic information meanwhile a change in the phase is giving indications for a change in the material properties of the sample, such as adhesion, stiffness, or frictional properties. **Figure 6.1a-c** shows the topography (a) and the phase (b) image of a flake obtained with an AFM in intermittent contact mode as well as the corresponding optical image (c). A sketch of the AFM working in intermittent contact mode can be found in **Figure 6.1d**. A well-formed flake of triangular shape, with a flat surface and 3.9 nm in height (which corresponds to 5-6 monolayers of WS$_2$), is seen in the topography scan. The optical microscope image of this flake (see **Figure 6.1c**) reveals the presence of a dust particle located on the right apex of the triangular flake. To avoid a contamination of the AFM probe with this particle, the AFM micrograph was not centered and is not showing the complete flake. The corresponding AFM phase image (**Figure 6.1b**), reveals a finer structure within the flake, which is not visible in the topography, indicating a change in the sample composition. Three triangles with different phase shifts are covered by a three-fold symmetry "flowerlike" structure mimicking the shape of a Trillium flower. The formation is only seen in the phase and not in the topography image and only in hard tapping condition. The flower structure is not visible in the optical microscopy image (**Figure 6.1c**), indicating that such secondary structure presumably has different composition and mechanical properties as compared to the underneath triangular flake.
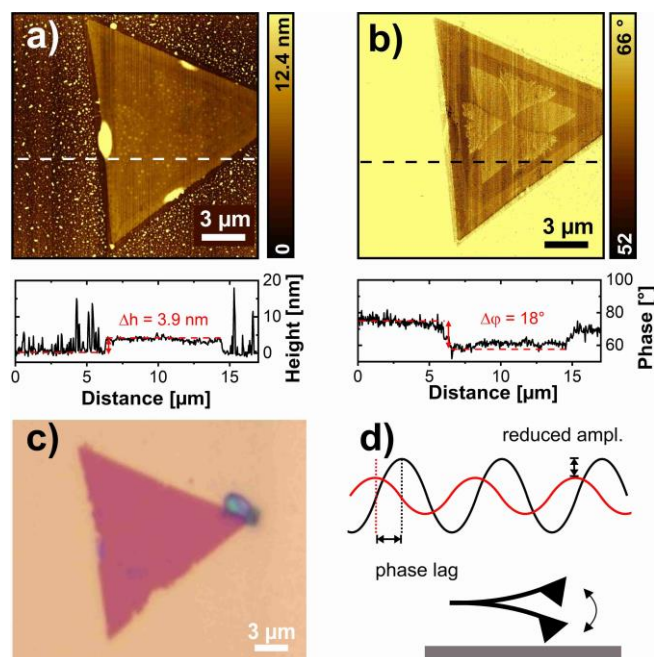
Figure 6.1. AFM scans of WS$_2$ flake performed in intermittent contact mode. The height map is shown in a) and the phase in b). A cantilever with a spring constant of 48 N/m was used for these measurements. The optical microscope image of the flake can be found in c) and a sketch of the AFM working in intermittent contact mode in d). Adapted with permission from [20]. Copyright 2022 American Chemical Society.

6.3 Raman Spectroscopy of a WS$_2$ Single Flake

To further analyze the structure and composition of the threefold symmetry confocal Raman spectra and maps were acquired using λ=532 nm as the excitation source. Previous studies acquired with λ=514 nm as the excitation source revealed Raman spectrum is dominated by first order modes LA(M) at 176 cm^{-1}, 2LA (M) at 351 cm^{-1}, E$^1_{2g}$ (Γ) at 356 cm^{-1} and A$_{1g}$(Γ) at 418 cm^{-1}.[21] **Figure 6.2a** is showing selected Raman spectra at different positions within the fine structure. The first spectrum got recorded within one of the three petals of the flower (Position I), the second spectrum was obtained outside the leaves, but within the inner triangle (Position II) and the last spectrum is located close to the edge of the flake (Position III). All spectra collected on the WS$_2$ flake are showing two Raman modes in addition to the Silicon peak at 520.7 cm^{-1}. The first peak, located around 351 cm$^-$

^{1}, is a convolution of the in-plane E^{1}_{2g} mode and the 2LA mode. The out-of-plane A_{1g} mode appears around 419 cm^{-1}. Under 532 nm excitation PL can appear in WS$_2$ in the [2600-3700] cm^{-1} spectral range. Comparing the Raman spectra collected on the distinct area shows that no new modes appear and only the relative intensities of the E_{2g}+2LA and A_{1g} are altered. The convoluted E^{1}_{2g}+2LA peak is decreasing by a two-fold factor going from the edge of the flake to the inner triangle and the drop further increases inside the threefold symmetry. Here, the intensity of the E^{1}_{2g}+2LA peak is reduced by a three-fold factor with respect to the edge of the flake. The same change is also observed for the A_{1g} mode. Further analysis shows that the wavenumber associated with the A_{1g} mode is slightly shifted depending on its position. At the edge of the flake (position III) the mode appears at 419.2 cm^{-1}, within the inner triangle (position II) at 418.8 cm^{-1} and inside the petal of the flower (position I) at 418.0 cm^{-1}, indicating a total shift of 1.2 cm^{-1}. The width of the gaussian function in the same regions is changing from 16.7 cm^{-1} to 16.2 cm^{-1} and 18.8 cm^{-1}, respectively. The peak position of the convoluted E^{1}_{2g}+2LA peak is changing from 348.6 cm^{-1} to 349.9 cm^{-1} and 350.15 cm^{-1} with associated widths that varies from 22.7 cm^{-1} to 21.3 cm^{-1} and 21.7 cm^{-1}. Therefore, the difference between the E^{1}_{2g}+2LA and A_{1g} peaks is changing from 70.6 cm^{-1} at position III to 68.9 cm^{-1} at position II and 67.8 cm^{-1} at position I. The PL intensity is reduced by one order of magnitude (15×) from the edge of the flake (position III) towards the center (position II or I). The origin of the PL quenching is at this moment unclear but may be caused by strain, doping effects or nonradiative recombination.

Figure 6.2b is showing the integrated Raman intensity map (blue map) of the strain related E^{1}_{2g} and 2LA mode of the WS$_2$. Similar to the AFM phase image, the threefold symmetry is clearly revealed, indicated by a lower Raman intensity towards the center. The same is also true for the doping related A_{1g} mode (see **Figure 6.2c** green map) and the PL (2600 – 3700 cm^{-1}, **Figure 6.2d** red map) of the WS$_2$ flake. Both maps show the same structure as for the blue map of the E^{1}_{2g}+2LA peak reported. Interestingly, the dust particle, which can be seen in the optical microscope image of the flake (**Figure 6.2c**), is absent in the Raman maps. **Figure 6.2e** is a map of the ratio of the E^{1}_{2g}+2LA peak (blue map) with respect to the A_{1g} mode (green map). In this map, a sharp boundary between the outer and inner

triangle became visible, beside the threefold symmetry, indicating two domains. A change in the ratio can give indications for a strain caused by a lattice mismatch between these two domains.
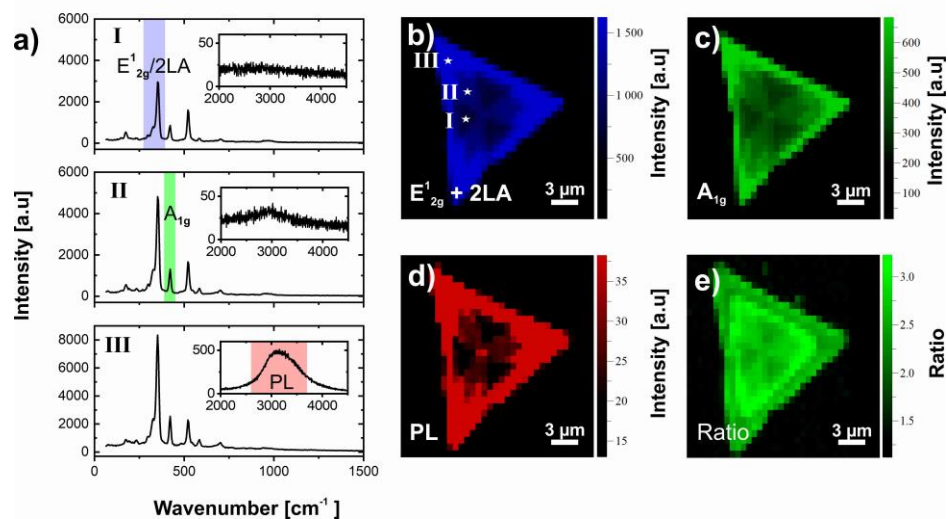

Figure 6.2 Confocal Raman spectra of different spots within the WS₂ flake (a) and the corresponding Raman map (b-e). The integration time of the Raman spectra was set to 0.5 s and the irradiance to $1 \cdot 10^5$ W/cm². A grating of 600 gr/mm, pinhole of 300 μm and slit of 100 μm were used. The blue map (b) shows the integrated intensity of the convoluted in-plane E^1_{2g} and 2LA mode (351 cm^{-1}), while the green map (c) displays the Raman map of the out-of-plane A_{1g} mode (419 cm^{-1}). The position from where the spectra of a) were taken are indicated in the blue Raman map (b). The PL map of the spectral range 2600 – 3700 cm^{-1} is shown in d). The ratio of the blue and green map can be found in e). The maps consist of 30×30 point-spectra with a spacing of 0.6 μm along the x and y direction (18×18) μm². Adapted with permission from [20]. Copyright 2022 American Chemical Society.

6.4 Tip-Enhanced Raman Spectroscopy (TERS) of the WS₂ Hidden Flower

The confocal Raman microscopy on the WS₂ flakes showed some limitations. The spatial resolution is limited by diffraction and a longer acquisition time or higher intensity yields

to oxidation of the flake. In this context, TERS can overcome such spatial resolution limitation by surpassing the diffraction limit and enabling the acquisition with lower excitation intensity and/or with shorter acquisition times. A 532 nm laser excitation was focussed from the side on the apex of a front side Ag-coated AFM cantilever. This generates a local hot spot through excitation of the plasmon mode of the Ag-coated tip thereby enhancing the local electromagnetic field at the junction between the tip and the sample and subsequently, enhancing the Raman signal. At each pixel of the TERS map a spectrum is acquired with the tip in direct contact with the surface. Between two pixels of the map, the sample is moved in intermittent contact mode in order to prevent the probe from damage and to keep the plasmonic enhancement. This provides beside the Raman map (with a high spatial and spectral resolution) simultaneous topographic information. **Figure 6.3** summarizes the obtained TERS results. Averaged spectra of 25 pixel at different positions within the flake are presented in **Figure 6.3a**. Analyzing the recorded spectra shows the same trend, which was already observed with the confocal Raman microscope and which is visible in the corresponding maps, namely that the intensity of the LA, $E^1_{2g}+2LA$ and A_{1g} mode is continuously decreasing from the edge of the flake towards the center of the threefold symmetry. Additionally, the peak position of the silicon (Si) mode is changing from 520.3 cm^{-1} at the edge of the flake (position 4 in **Figure 6.3a**) to 519 cm^{-1} (at positions 2 and 3) and finally to 518.8 cm^{-1} in the center of the leaf of the threefold symmetry (position 1). This indicates a coupling between the substrate and the WS_2 flake which is shifting the phonon mode of the silicon. A similar trend was observed for the LA mode, which is another in-plane longitudinal acoustic mode. Here, the peak position at the edge of the flake is 179.9 cm^{-1} (position 4), 175.9 cm^{-1} at position 2, 173 cm^{-1} in the center of the flake (position 3) and 173.2 within the threefold symmetry (position 1). The convoluted $E^1_{2g}+2LA$ peak shows a smaller shift of 352.2 cm^{-1} at the edge (position 4) to 350.3 cm^{-1} (at position 2 and position 3) and 350.7 cm^{-1} within the fine structure (position 1). The origin of the mode spectral shift is unclear at this moment, but in the TERS experiments the enhancement of the Raman signal depends on many parameters, such as polarization and illumination angle of the incident light.[22] The tip angle with respect to the surface of the sample is also an important parameter. This leads to an enhancement of the

in-plane and the out-of-plane mode, but with different enhancement factors. In the current study the light is linearly polarized and is illuminating the cantilever under an angle of 60°. Considering the tip-tilt angle of 11° this results in a tip illumination angle of 49° and the appearance of the in-plane E^1_{2g} and 2LA modes in the TERS spectra (see **Figure 6.3**) and the out-of-plane A_{1g} mode, as well. The A_{1g} mode shows a change in the peak position towards the same direction. Here, the peak appears at 421.4 cm^{-1} at the edge of the flake (position 4), reduces to 421 cm^{-1} at position 2, followed by a further reduction to 419.9 cm^{-1} in the center of the flake (position 3) and 419.7 cm^{-1} within the fine structure (position 1). In **Figure 6.3b,** an overlay of the AFM topography with the TERS map of the E^1_{2g}+2LA (311 - 383 cm^{-1}) peak is shown with enhanced contrast and resolution. The small boxes indicate the position of the spectra recorded in **Figure 6.3a.** In this map the threefold symmetry is clearly visible. This permits to assign the Raman map to characteristic features in the topography of the WS$_2$ flake and is only possible with the TERS technique. In **Figure 6.3c** the TERS map of the LA mode (152 – 202 cm^{-1}) is shown. In this map, the threefold symmetry is also indicated but not as pronounced as compared to the map of the E^1_{2g}+2LA mode, presumably because of a poorer signal-to-noise ratio. The TERS map of the A_{1g} mode (400 – 440 cm^{-1}, see **Figure 6.3d**) shows the fine structure within the WS$_2$ flake more clear, same as in the confocal Raman map (see **Figure 6.2b**), but not as much as in the case of the E^1_{2g}/2LA peak (see **Figure 6.3b**). The increase in the Raman signal as a function of the tip sample distance is shown in **Figure 6.3e**. The tip-in spectrum is acquired when the tip is in direct contact with the surface. In such experiments, the signal contains both the near- and far- fields contributions. In order to obtain the far-field scattering the tip was lifted a few nanometers away from the surface, which results in a drastic drop of the signal-to-noise ratio.

The difference between the tip-in/tip-out experiments can be used to estimate the local enhancement factor (EF) of the TERS experiments by considering the diffraction limited excitation area of the far-field $A_{FF} \sim 2$ μm^2 and the near-field area of the hot-spot ($A_{NF} \approx \pi(r_{tip})^2 \sim 0.003$ μm^2) confined at the extremity of the Ag tip ($r_{tip} \sim 30$ nm). The EF, based

on **equation 1.4**, was estimated to 4565 for the LA mode, 2629 for the E^1_{2g}+2LA peak, 5450 for the A_{1g} mode and 2250 for the Si peak.
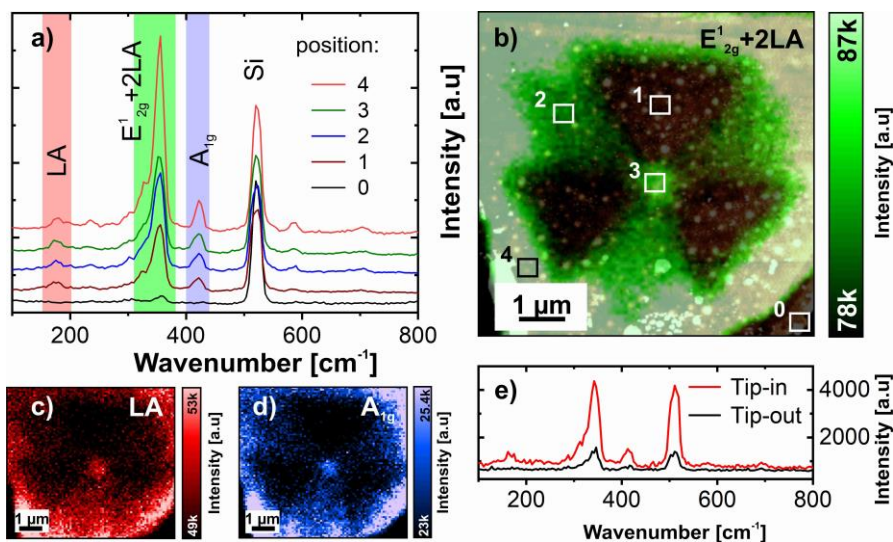

Figure 6.3. Micrographs and spectra of the TERS measurements. Averaged spectra of 25 pixel of five different positions on the flake are seen in a). In b) the overlay of the topography and the TERS map of the convoluted E^1_{2g}+2LA peak (311 - 383 cm^{-1}) is shown, highlighting the threefold symmetry. The small boxes indicate the position of the spectra recorded in a). The TERS map of the LA (152 – 202 cm^{-1}) and A_{1g} mode (400 – 440 cm^{-1}) are displayed in c) and d). A grating with 600 gr/mm, a pinhole of 300 μm, a slit of 100 μm, an exposure time of 0.4 s and a scan speed of 1.1 line/s was used for the acquisition of the TERS maps. The map consists of 100 × 100 spectra (scan size 7.5 × 7.2 μm^2), with a spacing of 75 nm along X (72 nm along Y). The laser power at the apex of the tip was adjusted to 1.2 μW. The acquired Raman spectra when the tip is in contact and withdrawn from the surface shown in e), indicating a strong enhancement of the signal. Adapted with permission from [20]. Copyright 2022 American Chemical Society.

6.5 Electrical Properties of WS_2

To complete the Raman investigation and the mapping of the nanomechanical properties, the electronic properties of the WS_2 flake were investigated using KPFM in amplitude modulation. In the first pass of a KPFM experiment, the topography in intermittent contact mode is obtained. The recorded topography (**Figure 6.4a,b**) is not showing the threefold symmetry, of previous topography measurements. In the second pass the surface potential is measured with a constant tip lift of 15 nm. A sketch of the AFM working in AM-KPFM mode is presented in **Figure 6.4c**. Here, a conductive cantilever with a spring constant of 5 N/m is used. **Figure 6.4d** shows a map of the relative change in the surface potential/ CPD with respect to the SiO_2. The threefold symmetry is clearly visible in the map and the cross section **(Figure 6.4e)** is showing a change in the surface potential of $\Delta V_{CPD} = 0.05$ V. The work function difference between the tip and the sample is calculated from the CPD following **equation 1.2**. The sample consists of pure SiO_2 and a stack of WS_2 on SiO_2. Therefore, the surface potential difference between these two regions is used to calculate the work function of the WS_2 (Φ_{WS_2}):

$$\Delta V_{CPD} = V_{WS_2} - V_{SiO_2}$$

$$= \frac{1}{e}\left(\Phi_{tip} - \Phi_{WS_2}\right) - \frac{1}{e}\left(\Phi_{tip} - \Phi_{SiO_2}\right) = \frac{1}{e}\left(\Phi_{SiO_2} - \Phi_{WS_2}\right) \tag{6.1}$$

$$\Leftrightarrow \Phi_{WS_2}/e = \Phi_{SiO_2}/e - \Delta V_{CPD}$$

Here, Φ_{SiO_2} is the work function of the SiO_2 with a literature value of ~5.0 eV.[23] **Figure 6.4f** shows the change in the work function along the WS_2 flake. A work function of ~4.6 eV for a mono-layer of WS_2 and ~4.2 eV for bulk WS_2 is reported in literature.[24] Therefore, the measure work function of 4.55 eV, which is increasing by 50 meV within the tungsten vacancies to 4.6 eV, shows that the flake composing of 5 – 6 monolayers cannot be considered as bulk material. From this it follows that trap states within the tungsten-

vacancy domains act as a dopant and tune the work function of the WS_2 towards an insulating material.
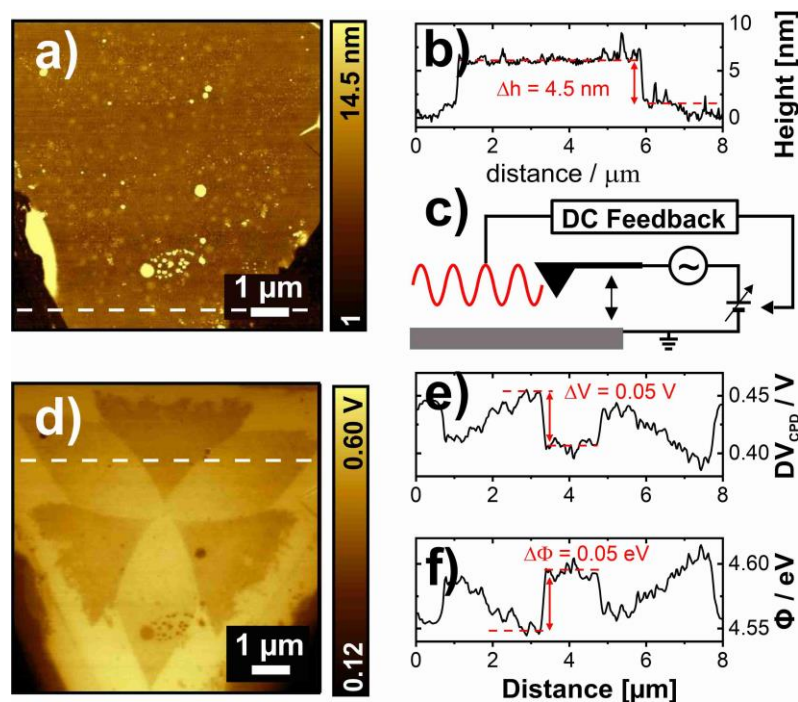

Figure 6.4 Results of the KPFM measurements on the WS_2 flake in amplitude modulation. In the first pass the topography is obtained and in the second pass the surface potential is measured with a constant tip lift of 15 nm. The AFM micrograph of the flake topography is shown in a) and the cross section in b). In c) a sketch of the 2nd pass of an AFM working in AM-KPFM mode is presented. The map of the relative change of the surface potential with respect to the SiO_2 is shown in d). A cross section along the threefold symmetry is shown in e) and indicated by the dashed white line in d). The work function of the WS_2 is calculated from the relative change of the surface potential and the result is displayed in f). Adapted with permission from [20]. Copyright 2022 American Chemical Society.

6.6 Mechanical Properties of WS_2 Flakes

To further analyze the mechanical properties of WS_2 flake, more advanced AFM modes such as force modulation (FMM) and PeakForce Quantitative nanomechanics (QNM) modes were used. All FMM and QNM were conducted by post-doctoral researcher Dr. Joachim Jelken.

FMM yields the nanomechanical properties associated with the distinct domains of the threefold symmetry. Topography, lateral force map of trace and retrace obtained from the FMM mode are depicted in **Figure 6.5a-d.** The topography map (**Figure 6.5a**) shows the same results as in intermittent contact mode, a flat and 4.2 nm height flake is observed. **Figure 6.5b** shows the torsion of the cantilever for trace while **Figure 6.5c** in retrace scan direction. The torsion is inverted in both images, giving strong indication that the friction force on the flake is higher compared to the substrate. Regions with a larger friction force increase the cantilever torsion.

Only a change in the friction force appears in an inverted signal in the trace and retrace. Regions with a larger friction force increase the cantilever torsion. The fine structure within the flake (tungsten vacancies) shows a small reduction in the friction force with respect to the rest of the flake but still larger than the friction force of the substrate. The torsion signal is further analyzed to reveal if it is topographic or frictional origin. The sum signal of the cantilever torsion in trace and retrace ($\Sigma/2$) carries mainly the topographic information, because it shows the same cantilever torsion in trace and retrace which will add in the sum. A change in the friction results in an opposite cantilever torsion in trace and retrace, which cancels out in the sum of these two signals. Here, the difference between these signals ($\Delta/2$) is mainly showing the change in the friction force and suppresses the cantilever torsion due to a change in the topography. **Figure 6.5d** is showing the sum ($\Sigma/2$) and the difference ($\Delta/2$) of the cantilever torsion in trace and retrace, indicating clearly that the origin of the change in the signal is a change in the frictional force and not cause by a change of the topography.
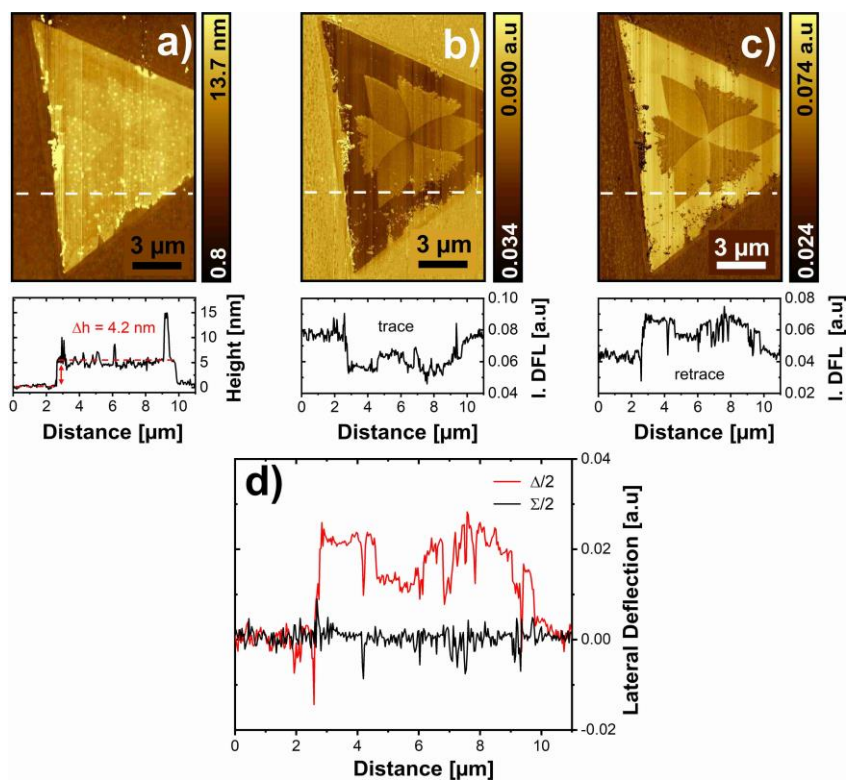
Figure 6.5 Vertical deflection (a) and torsion (b-c) of the AFM cantilever during the scan of the WS$_2$ flake recorded in force modulation mode. The DC signal of the vertical deflection reveals topographic information (a), while from the torsion the friction force is obtained, measured in trace (b), and retrace (c). The sum ($\Sigma/2$) and difference signal ($\Delta/2$) of the cantilever torsion in trace and retrace revels that the change in the cantilever torsion is frictional origin, as shown in d). A force modulation cantilever with a spring constant of 2 N/m was used for the measurement. Adapted with permission from [20]. Copyright 2022 American Chemical Society.

An increase in the amplitude corresponds with a region of higher Young's modulus. The modulus of the WS$_2$ flakes being in the range of ~300 GPa, [25] gives rise to use an AFM cantilever with a stiff spring constant of 48 N/m. Measurements with a force modulation cantilever (soft spring constant of 2 N/m) were not showing any change in the amplitude or phase, only in the friction force. **Figure 6.6a-c** shows the topography (a), the lock-in amplitude (b) and lock-in phase (c) in force modulation mode. In the following the analysis

was performed on a different flake, which showed the same flower-like structure. The optical image of this flake can be seen in **Figure 6.6d** and is not showing the flower-fine-structure. A sketch of the AFM working in FMM mode is presented in **Figure 6.6e**.

The topography map agrees with the results found in intermittent contact mode, namely a flat flake without any fine structure and of four WS_2 monolayers in height is observed. The lock-in amplitude shows a positive contrast between the substrate and WS_2 flake. This is in agreement with the expected Young's modulus of the Si substrate of 130-190 GPa [26] and of the WS_2 of 300 GPa. [25] The threefold-symmetry within the flake is clearly visible by a reduced amplitude in the tungsten vacancies (see **Figure 6.5b**), indicating a smaller Young's modulus. Additionally, the lock-in phase map (see **Figure 6.5c**) shows an increase in the phase shift within the threefold symmetry.
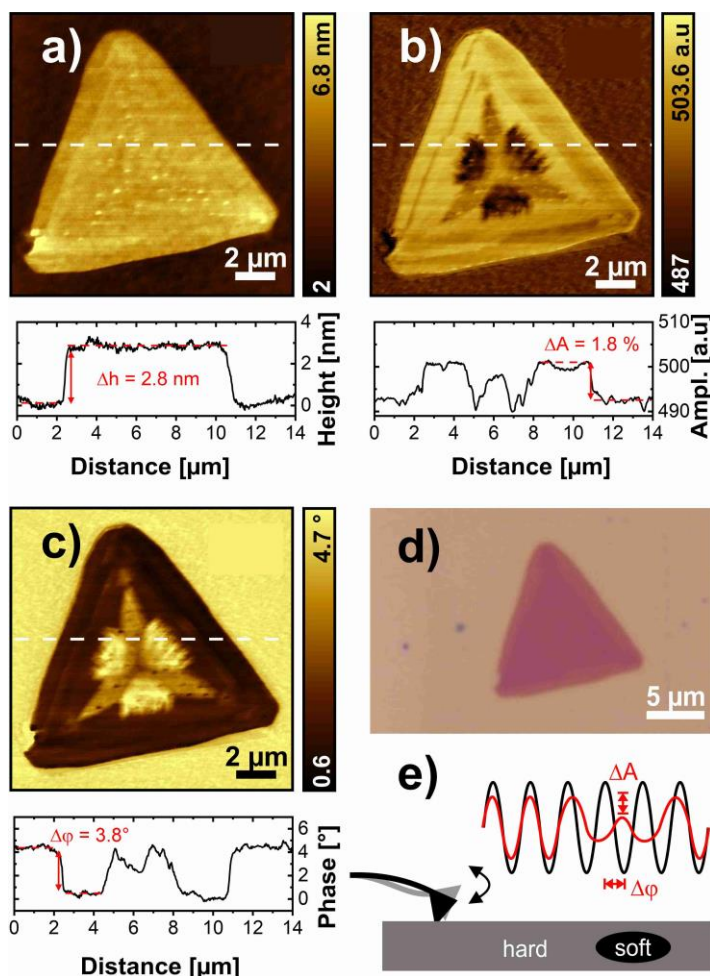
Figure 6.6 Force modulation AFM micrographs of WS$_2$ flake. The DC signal of the vertical cantilever deflection provides topographic information (a), while the analysis of the AC signal with the help of a lock-in-controller delivers the change in amplitude (b) and phase (c). A cantilever with a spring constant of 48 N/m was used for the measurements. In d) the optical microscope image of the flake is shown. A sketch of the AFM working in force modulation mode is presented in e). Adapted with permission from [20]. Copyright 2022 American Chemical Society.

In QNM mode adhesion force, the Young's modulus, the topography and the sample deformation are obtained. The mechanical properties of the sample are obtained through force vs. distance curves. The curves allow to obtain the Young's modulus of the sample by analyzing the slope of the force vs. distance curve and applying the DMT model [27]

(Derjaguin, Muller, Toropov). Additional information such as energy dissipation and sample deformation are measured in this mode as well.

Figure 6.7 shows the results of the PeakForce QNM measurements on a WS_2 flake. The topography **Figure 6.7a** is showing a flat flake of 3 nm in height (~ 4 monolayer of WS_2) without a fine structure, same as in the intermittent contact and FMM mode. In contrast the adhesion map (**Figure 6.7b**) reveals the same macroscopic structure with the threefold symmetry as seen in the phase map in the intermittent contact mode (see **Figure 6.1b**) and the change in amplitude, phase and cantilever torsion in the FMM (**Figure 6.6**). The flake shows an in increase in the adhesion force of 50 nN (compared to the substrate), while within the branches of the flower (tungsten vacancies) the adhesion force is reduced by ~25 nN.

Mapping the mechanical properties together with TERS spectroscopy is a powerful complementary approach to fluorescence labeling of defects in 2D-TMDs to indicate sulfur- or tungsten-vacancy domains. [19]
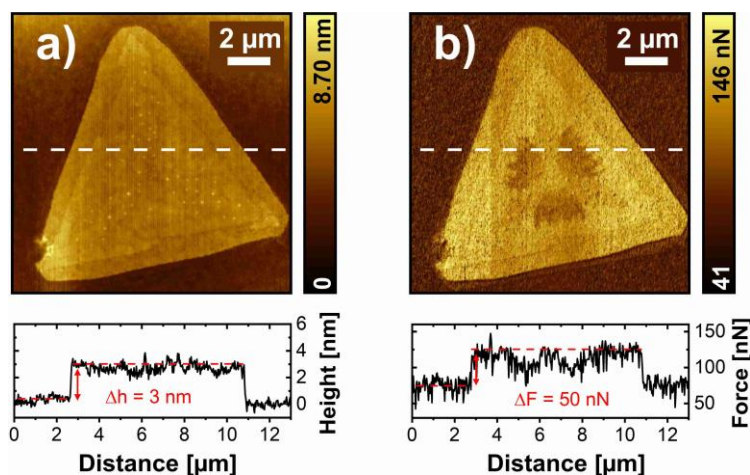

Figure 6.7 AFM micrographs performed in PeakForce QNM mode. Controlling the peak force reveals topographic information (a) and the adhesion force is obtained from the Pull-off point of the withdraw curve (b). The cantilever spring constant for these experiments was 200 N/m. Adapted with permission from [20]. Copyright 2022 American Chemical Society.

6.7 Conclusions

In this work, a one step growth using a single-zone tube furnace is presented, producing a lateral heterostructure within a WS_2 flake with different mechanical, electronic and optical properties. Here, the sulfur introduction time is controlling the sulfur concentration which affect the shape of the flake and defect generation. Due to the initial rapid growth of the flake, as a result of a higher sulfur concentration, an inner threefold symmetry is formed. A lower sulfur concentration at the end of the growth process results in an overall triangular shape of the flake without secondary structures. Spatially resolved Raman- and PL-spectroscopy revealed that these domains consist of tungsten vacancies, indicated by a strong photoluminescence quenching. TERS provides the required spatial resolution reveal characteristic features of the hidden structure. Probing the electronical properties using KPFM reveals a local reduction of the surface potential (increased work function) within the threefold symmetry. Probing the nano-mechanical properties of the WS_2 flake, using different AFM modes, shows that within the defect domains the friction and adhesion forces are reduced. Flower-like domains show indications of an increased Young's modulus. Therefore, the defect domains control the optical, mechanical, and electronic properties of the semiconductor-semiconductor heterojunction within the WS_2 flake, which makes it interesting for further applications.

6.8 References

(1) Voiry, D.; Mohite, A.; Chhowalla, M. Phase Engineering of Transition Metal Dichalcogenides. *Chem. Soc. Rev.* **2015**, *44* (9), 2702-2712.

(2) Aljarb, A.; Cao, Z.; Tang, H.-L.; Huang, J.-K.; Li, M.; Hu, W.; Cavallo, L.; Li, L.-J. Substrate Lattice-Guided Seed Formation Controls the Orientation of 2D Transition-Metal Dichalcogenides. *ACS Nano* **2017**, *11* (9), 9215-9222.

(3) Cain, J. D.; Shi, F.; Wu, J.; Dravid, V. P. Growth Mechanism of Transition Metal Dichalcogenide Monolayers: The Role of Self-Seeding Fullerene Nuclei. *ACS Nano* **2016**, *10* (5), 5440-5445.

(4) Jo, S.; Jung, J.-W.; Baik, J.; Kang, J.-W.; Park, I.-K.; Bae, T.-S.; Chung, H.-S.; Cho, C.-H. Surface-Diffusion-Limited Growth of Atomically Thin WS_2 Crystals From Core–Shell Nuclei. *Nanoscale* **2019**, *11* (18), 8706-8714.

(5) Cong, C.; Shang, J.; Wu, X.; Cao, B.; Peimyoo, N.; Qiu, C.; Sun, L.; Yu, T. Synthesis and Optical Properties of Large-Area Single-Crystalline 2D Semiconductor WS_2 Monolayer from Chemical Vapor Deposition. *Adv. Opt. Mater.* **2014**, *2* (2), 131-136.

(6) Lee, Y.-H.; Yu, L.; Wang, H.; Fang, W.; Ling, X.; Shi, Y.; Lin, C.-T.; Huang, J.-K.; Chang, M.-T.; Chang, C.-S.; et al. Synthesis and Transfer of Single-Layer Transition Metal Disulfides on Diverse Surfaces. *Nano Lett.* **2013**, *13* (4), 1852-1857.

(7) Zafar, A.; Zafar, Z.; Zhao, W.; Jiang, J.; Zhang, Y.; Chen, Y.; Lu, J.; Ni, Z. Sulfur-Mastery: Precise Synthesis of 2D Transition Metal Dichalcogenides. *Adv. Funct. Mater.* **2019**, *29* (27), 1809261.

(8) Xu, Z.; Lv, Y.; Li, J.; Huang, F.; Nie, P.; Zhang, S.; Zhao, S.; Zhao, S.; Wei, G. CVD Controlled Growth of Large-Scale WS_2 Monolayers. *RCS Adv.* **2019**, *9* (51), 29628-29635.

(9) Kang, S.; Eshete, Y. A.; Lee, S.; Won, D.; Im, S.; Lee, S.; Cho, S.; Yang, H. Bandgap Modulation in the Two-Dimensional Core-Shell-Structured Monolayers of WS_2. *iScience* **2022**, *25* (1), 103563.

(10) Fan, X.; Zhao, Y.; Zheng, W.; Li, H.; Wu, X.; Hu, X.; Zhang, X.; Zhu, X.; Zhang, Q.; Wang, X.; et al. Controllable Growth and Formation Mechanisms of Dislocated WS_2 Spirals. *Nano Lett.* **2018**, *18* (6), 3885-3892.

(11) Zhao, Y.; Jin, S. Stacking and Twisting of Layered Materials Enabled by Screw Dislocations and Non-Euclidean Surfaces. *Acc. Mater. Res.* **2022**, *3* (3), 369-378.

(12) Lin, W.-H.; Tseng, W.-S.; Went, C. M.; Teague, M. L.; Rossman, G. R.; Atwater, H. A.; Yeh, N.-C. Nearly 90% Circularly Polarized Emission in Monolayer WS_2 Single Crystals by Chemical Vapor Deposition. *ACS Nano* **2020**, *14* (2), 1350-1359.

(13) Lin, Y.-C.; Li, S.; Komsa, H.-P.; Chang, L.-J.; Krasheninnikov, A. V.; Eda, G.; Suenaga, K. Revealing the Atomic Defects of WS_2 Governing Its Distinct Optical Emissions. *Adv. Funct. Mater.* **2018**, *28* (4), 1704210.

(14) Jeong, H. Y.; Jin, Y.; Yun, S. J.; Zhao, J.; Baik, J.; Keum, D. H.; Lee, H. S.; Lee, Y. H. Heterogeneous Defect Domains in Single-Crystalline Hexagonal WS_2. *Adv. Mater.* **2017**, *29* (15), 1605043.

(15) Wu, K.; Zhong, H.; Guo, Q.; Tang, J.; Yang, Z.; Qian, L.; Yuan, S.; Zhang, S.; Xu, H. Revealing the Competition between Defect-Trapped Exciton and Band-Edge Exciton Photoluminescence in Monolayer Hexagonal WS_2. *Adv. Opt. Mater.* **2022**, *10* (6), 2101971.

(16) Sheng, Y.; Wang, X.; Fujisawa, K.; Ying, S.; Elias, A. L.; Lin, Z.; Xu, W.; Zhou, Y.; Korsunsky, A. M.; Bhaskaran, H.; et al. Photoluminescence Segmentation within Individual Hexagonal Monolayer Tungsten Disulfide Domains Grown by Chemical Vapor Deposition. *ACS Appl. Mater. Inter.* **2017**, *9* (17), 15005-15014.

(17) Kumar, P.; Singh, B.; Kumar, P.; Balakrishnan, V. Competing Thermal Expansion Mismatch and Lattice Strain Engineered Growth of Crack Free WS_2 In-Plane Heterostructures. *J. Mater. Chem. C* **2018**, *6* (42), 11407-11415.

(18) Kumar, P.; Verma, N. C.; Goyal, N.; Biswas, J.; Lodha, S.; Nandi, C. K.; Balakrishnan, V. Phase Engineering of Seamless Heterophase Homojunctions with Co-Existing 3R and 2H Phases in WS_2 Monolayers. *Nanoscale* **2018**, *10* (7), 3320-3330.

(19) Zhang, M.; Lihter, M.; Chen, T.-H.; Macha, M.; Rayabharam, A.; Banjac, K.; Zhao, Y.; Wang, Z.; Zhang, J.; Comtet, J.; et al. Super-Resolved Optical Mapping of Reactive Sulfur-Vacancies in Two-Dimensional Transition Metal Dichalcogenides. *ACS Nano* **2021**, *15* (4), 7168-7178.

(20) Jelken, J.; Avilés, M. O.; Lagugné-Labarthet, F. The Hidden Flower in WS_2 Flakes: A Combined Nanomechanical and Tip-Enhanced Raman Exploration. *ACS Nano* **2022**, *16* (8), 12352-12363.

(21) Berkdemir, A.; Gutiérrez, H. R.; Botello-Méndez, A. R.; Perea-López, N.; Elías, A. L.; Chia, C.-I.; Wang, B.; Crespi, V. H.; López-Urías, F.; Charlier, J.-C.; et al. Identification of Individual and Few Layers of WS_2 Using Raman Spectroscopy. *Sci. Rep.* **2013**, *3* (1), 1755.

(22) Maximiano, R. V.; Beams, R.; Novotny, L.; Jorio, A.; Cançado, L. G. Mechanism of Near-Field Raman Enhancement in Two-Dimensional Systems. *Phys. Rev. B* **2012**, *85* (23), 235434.

(23) Lee, N. J.; Yoo, J. W.; Choi, Y. J.; Kang, C. J.; Jeon, D. Y.; Kim, D. C.; Seo, S.; Chung, H. J. The Interlayer Screening Effect of Graphene Sheets Investigated by Kelvin Probe Force Microscopy. *Appl. Phys. Lett.* **2009**, *95* (22), 222107.

(24) Britnell, L.; Ribeiro, R. M.; Eckmann, A.; Jalil, R.; Belle, B. D.; Mishchenko, A.; Kim, Y.-J.; Gorbachev, R. V.; Georgiou, T.; Morozov, S. V.; et al. Strong Light-Matter Interactions in Heterostructures of Atomically Thin Films. *Science* **2013**, *340* (6138), 1311-1314.

(25) Falin, A.; Holwill, M.; Lv, H.; Gan, W.; Cheng, J.; Zhang, R.; Qian, D.; Barnett, M. R.; Santos, E. J. G.; Novoselov, K. S.; et al. Mechanical Properties of Atomically Thin Tungsten Dichalcogenides: WS_2, WSe_2, and WTe_2. *ACS Nano* **2021**, *15* (2), 2600-2610.

(26) Hopcroft, M. A.; Nix, W. D.; Kenny, T. W. What is the Young's Modulus of Silicon? *J. Microelectromech. S.* **2010**, *19* (2), 229-238.

(27) Derjaguin, B. V.; Muller, V. M.; Toporov, Y. P. Effect of Contact Deformations on the Adhesion of Particles. *J. Colloid. Interf. Sci.* **1975**, *53* (2), 314-326.

Chapter 7

7 Conclusions and Outlook

In this thesis, we have extensively studied 1D and 2D materials using advanced nanoscale characterization instruments. These materials, produced and/or prepared in our laboratory, were further characterized with tip-enhanced Raman spectroscopy (TERS) which provided critical results that can be used to evaluate the crystalline polydispersity of the obtained materials, resulting in more reproducible samples. Other state-of-the-art characterization were accomplished using complementary techniques such as SEM, EDX, AFM advanced modes and KPFM. More specifically, these characterization procedures were applied to single-walled carbon nanotubes (SWNT), graphene and transition metal dichalcogenides (TMDs) flakes. In Chapter 3, carbon-containing materials such as graphene, graphite and SWNTs are investigated. Poor crystallinity in graphite was revealed at specific locations by Raman spectroscopy, TERS hyperspectral maps provided the possibility to classify SWNT depending on their metallic or semiconductive character. In this chapter, introductory machine learning in the form of artificial neural networks was exploited for a novel rapid analysis of the TERS hyperspectral maps.

In chapters 4-6, transition metal dichalcogenides 2D materials were grown using atmospheric pressure CVD. Specifically, WS_2 and VS_2 were investigated in order to reveal the presence of peculiar patterns at their surface or how their properties were altered though photooxidation. The synthesis of these materials with distinct sizes, thicknesses, chemical composition, and shapes is well described. In Chapter 4, the synthesis, and characterization of metallic 1T phase VS_2 is explored. The formation of a spiral periodic pattern at the surface of the VS_2 flake is caused by the rapid change in sulfur feeding rate through precursors, temperature, and cooling rate. The Raman spectra collected using confocal microscopy and/or tip-enhanced Raman are also carefully exploited to better understand the growth and orientations of the crystallites. Additionally, the electron work function modulation of the periodic spirals over the surface is revealed by KPFM yielding a quantitative value for the work function change. The novelty of this work relies on the

formation of periodic spiral pattern on the surface of VS_2 flakes. On these spirals, TERS and KPFM measurements reveal the growth orientation of crystallite formation that can affect chemical and electronic properties of VS_2 flakes.

The synthesis of VS_2 by CVD generates yields to various polymorphs and oxides, characterized by Raman spectroscopy. Interestingly, a photo-oxidation is promoted during the Raman and TERS experiments. Such photo-oxidation process occurs at a given energy density as discussed in Chapter 5. In the same chapter the TERS maps reveal the presence of crystalline and amorphous vanadium oxide. The findings described in this chapter determine the energy dose threshold required to avoid oxidation of VS_2 flakes and reveal the advantage of TERS technique to probe vanadium oxide mixtures.

A semiconducting WS_2 with hidden layered flower-like structure is investigated in Chapter 6. Here, though the CVD process sulfur introduction time affects the shape of the flake and growth rate, such that an inner threefold symmetry is formed. Tungsten vacancies are discussed which explain the photoluminescence (PL) quenching of the signal; confocal Raman and TERS results further contribute to understand such mechanisms. Electronic and mechanical properties are identified through KPFM and advanced nanomechanical AFM modes. The study shows the importance of using advanced AFM (not previously reported for WS_2) and TERS technique to identify the tungsten vacancies within the surface affecting the chemical, mechanical and electronic properties of WS_2 flakes.

Future applications of this work include the use of 1D and 2D materials to generate hybrid heterojunctions. Currently, 2D heterostructures composed of different metallic and semiconductive materials are extensively used as building blocks devices. [1] The electronic band structure at the junction interface is altered, forming the so-called heterojunction that is not available for single metal or semiconductive materials. Most metal-semiconductive heterostructures are limited to and generally focused on graphene based heterostructures. [2] It is proposed that stacking of TMDs with metallic and/or semiconductive heterostructures such as VS_2/WS_2 can lead to materials with highly tunable properties that can be exploited for electronics applications with tunable bandgap or in photonics applications with tunable

photonic bandgap. The full control of growth mechanism, [3] interface composition, size and heterogeneity between the junctions would be necessary prerequisite for the development of the next-generation of devices. [4, 5] To this end, TERS technique together with advanced nanomechanical measurements have a central role to play to optimize these materials with a better control over the CVD grown heterojunctions.[6] VS_2 flakes could be further researched to understand their enhancing applicability as a SERS substrate since metallic TMDs have abundant energy states near the Fermi level, as well as strong interactions with organic molecules. [7] Moreover, VS_2 spiral periodic flakes potentially could be functionalized and decorated with a metallic nanoparticles characterized through TERS, given it can help find unique modes resulting from the coupling of exciton-plasmon (plexciton). [8] On the same idea, nanofabricated plasmonic structures could be grown above the VO_x/WS_2 and be compared with bare heterostructure to determine plexciton mechanisms. The goal would be to effectively tune the coupling strength and properties of plasmon-exciton polaritons by changing the morphology or size of the coupled nanofabricated structure. [9]

Recent developed hybrid devices involving 1D/2D quasi-van der Waals materials offer an enhancement in photoresponsivity. [10] 1D/2D hybrid systems combine the advantages of the strong light absorption of nanoarrays and the excellent electrical properties of 2D TMDs. In this regard, 1D SWNTs in combination with WS_2 could be researched to probe the multiple excitation wavelengths and photo response through TERS study.

7.1 References

(1) Wei, Y.; Zhang, F.; Wei, J.; Yang, Z. CdSe 1D/2D Mixed-Dimensional Heterostructures: Curvature-Complementary Self-Assembly for Enhanced Visible-Light Photocatalysis. *Small* **2021**, *17* (33), 2102047.

(2) Tan, J.; Li, S.; Liu, B.; Cheng, H.-M. Structure, Preparation, and Applications of 2D Material-Based Metal–Semiconductor Heterostructures. *Small Structures* **2021**, *2* (1), 2000093.

(3) Zhang, K.; Ding, C.; Pan, B.; Wu, Z.; Marga, A.; Zhang, L.; Zeng, H.; Huang, S. Visualizing Van der Waals Epitaxial Growth of 2D Heterostructures. *Adv. Mater.* **2021**, *33* (45), 2105079.

(4) Zhou, X.; Hu, X.; Yu, J.; Liu, S.; Shu, Z.; Zhang, Q.; Li, H.; Ma, Y.; Xu, H.; Zhai, T. 2D Layered Material-Based van der Waals Heterostructures for Optoelectronics. *Adv. Funct. Mater.* **2018**, *28* (14), 1706587.

(5) Jariwala, D.; Marks, T. J.; Hersam, M. C. Mixed-Dimensional Van Der Waals Heterostructures. *Nat. Mater.* **2017**, *16* (2), 170-181.

(6) Garg, S.; Fix, J. P.; Krayev, A. V.; Flanery, C.; Colgrove, M.; Sulkanen, A. R.; Wang, M.; Liu, G.-Y.; Borys, N. J.; Kung, P. Nanoscale Raman Characterization of a 2D Semiconductor Lateral Heterostructure Interface. *ACS Nano* **2022**, *16* (1), 340-350.

(7) Song, X.; Wang, Y.; Zhao, F.; Li, Q.; Ta, H. Q.; Rümmeli, M. H.; Tully, C. G.; Li, Z.; Yin, W.-J.; Yang, L.; et al. Plasmon-Free Surface-Enhanced Raman Spectroscopy Using Metallic 2D Materials. *ACS Nano* **2019**, *13* (7), 8312-8319.

(8) Asgari, N.; Hamidi, S. M. Exciton-plasmon coupling in two-dimensional plexitonic nano grating. *Opt. Mater.* **2018**, *81*, 45-54.

(9) Liu, W.; Lee, B.; Naylor, C. H.; Ee, H.-S.; Park, J.; Johnson, A. T. C.; Agarwal, R. Strong Exciton–Plasmon Coupling in MoS2 Coupled with Plasmonic Lattice. *Nano Lett.* **2016**, *16* (2), 1262-1269.

(10) Zheng, Y.; Cao, B.; Tang, X.; Wu, Q.; Wang, W.; Li, G. Vertical 1D/2D Heterojunction Architectures for Self-Powered Photodetection Application: GaN

Nanorods Grown on Transition Metal Dichalcogenides. *ACS Nano* **2022**, *16* (2), 2798-2810.

Appendices A

Appendix A1 The acquired Raman spectra when the tip is in contact (tip in) and withdrawn (tip out) from the surface indicating a low enhancement of the signal of graphite.
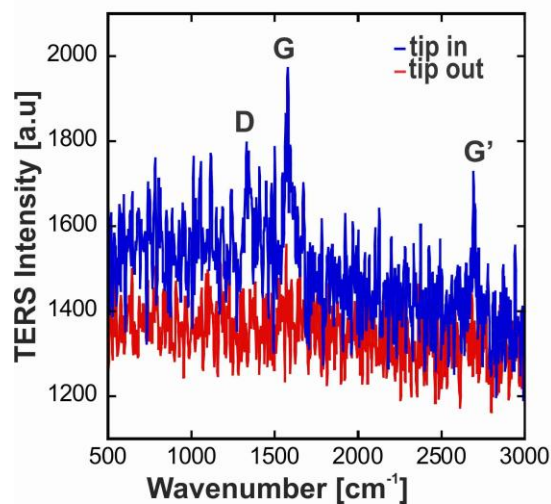
Appendix A2 The acquired Raman spectra when the tip is in contact (tip in) and withdrawn (tip out) from the surface indicating enhancement of the signal of SWNTs.
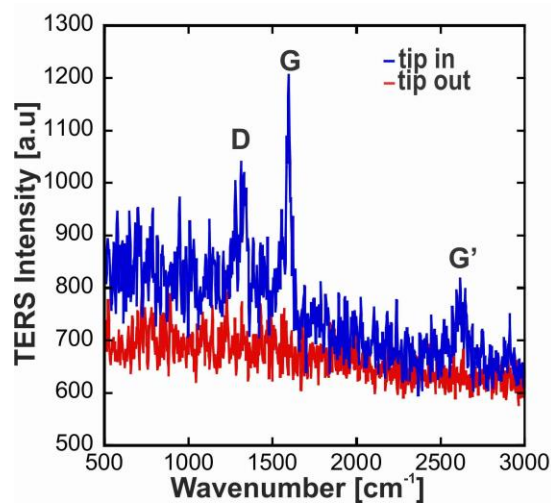
Appendices B

Appendix B3 Copyrights and permissions granted from their respective holders.

Chapter 1: Figure 1.3

Chapter 1: Figure 1.4

SPRINGER NATURE

Thank you for your order!

Dear Ms. Maria Aviles,

Thank you for placing your order through Copyright Clearance Center's RightsLink® service.

Order Summary

Licensee:	University of Western Ontario
Order Date:	Aug 30, 2022
Order Number:	5378610207276
Publication:	Nature Photonics
Title:	Why all the fuss about 2D semiconductors?
Type of Use:	Thesis/Dissertation
Order Total:	0.00 CAD

View or print complete details of your order and the publisher's terms and conditions.

Sincerely,

Copyright Clearance Center

Tel: +1-855-239-3415 / +1-978-646-2777
customercare@copyright.com
https://myaccount.copyright.com

CCC   **RightsLink**

SPRINGER NATURE

Why all the fuss about 2D semiconductors?

Author: Andres Castellanos-Gomez
Publication: Nature Photonics
Publisher: Springer Nature
Date: Mar 31, 2016

Copyright © 2016, Nature Publishing Group, a division of Macmillan Publishers Limited. All Rights Reserved.

Order Completed

Thank you for your order.

This Agreement between University of Western Ontario -- Maria Aviles ("You") and Springer Nature ("Springer Nature") consists of your license details and the terms and conditions provided by Springer Nature and Copyright Clearance Center.

Your confirmation email will contain your order number for future reference.

License Number   5378610207276   🖶 Printable Details

License date   Aug 30, 2022

☑ Licensed Content

Licensed Content Publisher	Springer Nature
Licensed Content Publication	Nature Photonics
Licensed Content Title	Why all the fuss about 2D semiconductors?
Licensed Content Author	Andres Castellanos-Gomez
Licensed Content Date	Mar 31, 2016

📋 Order Details

Type of Use	Thesis/Dissertation
Requestor type	academic/university or research institute
Format	print and electronic
Portion	figures/tables/illustrations
Number of figures/tables/illustrations	1
High-res required	no
Will you be translating?	no
Circulation/distribution	1000 - 1999
Author of this Springer Nature content	no

📄 About Your Work

Title	Characterization of 1D and 2D Materials with Tip-Enhanced Raman Spectroscopy
Institution name	University of Western Ontario
Expected	Nov 2022

📁 Additional Data

Portions	Figure 1

Chapter 1: Figure 1.8

Marketplace™

Dear Maria Aviles,

Thank you for placing your order on Marketplace™.

Order Summary:
Order date: 30 Aug 2022
Order number: 1263020
No. of items: 1
Order total: 0.00 CAD

Billing Summary:
Payment method: Invoice
An invoice will be generated and emailed within 24 hours.

To view your order details, click the following link, sign in, and search for your order:
Manage Account.

How was your experience? Click here to give us feedback

Please do not reply to this message.

To speak with a Customer Service Representative, call +1-855-239-3415 toll free or +1-978-646-2600 (24 hours a day), or email your questions and comments to support@copyright.com.

Sincerely,

The CCC Marketplace Team

Tel: 1-855-239-3415 / +1-978-646-2600
support@copyright.com
Manage Account

CCC

LICENSED CONTENT

Publication Title	Journal of materials chemistry. C, Materials for optical and electronic devices
Article Title	Nanoscale investigation of materials, chemical reactions, and biological systems by tip enhanced Raman spectroscopy – a review
Author/Editor	Royal Society of Chemistry (Great Britain)
Date	01/01/2013
Language	English
Country	United Kingdom of Great Britain and Northern Ireland
Rightsholder	Royal Society of Chemistry

Publication Type	e-Journal
Start Page	1307
End Page	1319
Issue	6
Volume	6
URL	http://pubs.rsc.org/en/journals/journ...

REQUEST DETAILS

Portion Type	Image/photo/illustration
Number of images / photos / illustrations	2
Format (select all that apply)	Print, Electronic
Who will republish the content?	Academic institution
Duration of Use	Life of current edition
Lifetime Unit Quantity	Up to 4,999
Rights Requested	Main product

Distribution	Canada
Translation	Original language of publication
Copies for the disabled?	No
Minor editing privileges?	No
Incidental promotional use?	No
Currency	CAD

NEW WORK DETAILS

Title	Characterization of 1D and 2D Materials with Tip-Enhanced Raman Spectroscopy
Instructor name	Dr. François Lagugné-Labarthet

Institution name	University of Western Ontario
Expected presentation date	2022-11-06

ADDITIONAL DETAILS

Order reference number	N/A

The requesting person / organization to appear on the license	María Olivia Avilés Galarza

REUSE CONTENT DETAILS

Title, description or numeric reference of the portion(s)	Fig.1, Fig.2
Editor of portion(s)	Kolhatkar, G.; Plathier, J.; Ruediger, A.
Volume of serial or monograph	6
Page or page range of portion	1307-1319

Title of the article/chapter the portion is from	Nanoscale investigation of materials, chemical reactions, and biological systems by tip enhanced Raman spectroscopy – a review
Author of portion(s)	Kolhatkar, G.; Plathier, J.; Ruediger, A.
Issue, if republishing an article from a serial	6
Publication date of portion	2018-01-01

Chapter 3

Deciphering tip-enhanced Raman imaging of carbon nanotubes with deep learning neural networks

Chapter 4

Periodic Spiral Ripples on VS2 Flakes: A Tip-Enhanced Raman Investigation

Chapter 6

The Hidden Flower in WS2 Flakes: A Combined Nanomechanical and Tip-Enhanced Raman Exploration

Author: Joachim Jelken, María O. Avilés, François Lagugné-Labarthet

Publication: ACS Nano

Publisher: American Chemical Society

Date: Aug 1, 2022

Copyright © 2022, American Chemical Society

Curriculum Vitae

Name: María Olivia Avilés Galarza

**Post-secondary   Escuela Superior Politécnica del Litoral
Education and   Guayaquil, Ecuador
Degrees:**   2008-2015 Bachelor in Chemical Engineering

The University of Western Ontario
London, Ontario, Canada
2017-2022 PhD current

Related Work

Teaching Assistant (CHEM 2213/A) LAB
CHEM 2213: Organic Chemistry for Life Sciences
Department of Chemistry, The University of Western Ontario
Fall 2017, Fall 2018, Fall 2019, Summer 2019

Teaching Assistant (CHEM 1302/B) LAB/Resource Room
CHEM 1302: Discovering Chemical Energetics
Department of Chemistry, The University of Western Ontario
Winter 2019, Winter 2020, Fall 2021
Winter 2019, Winter 2020, Winter 2022

Teaching Assistant (CHEM 1301/A LAB)
CHEM 1301: Discovering Chemical Structure
Department of Chemistry, The University of Western Ontario
Fall 2020, Fall 2021

Research Assistant in Dr. François Lagugné-Labarthet
https://publish.uwo.ca/~flagugne/
Department of Chemistry, The University of Western Ontario
2017-present

PUBLICATIONS

1. Kozachuk, M. S.; **Avilés, M. O**.; Martin, R. R.; Potts, B.; Sham, T.-K.; Lagugné-Labarthet, F., Imaging the Surface of a Hand-Colored 19th Century Daguerreotype. *Appl. Spectrosc.* **2018**, 1-10.
2. Dhindsa, J. S.; Maar, R. R.; Barbon, S. M.; **Avilés, M. O**.; Powell, Z. K.; Lagugné-Labarthet, F.; Gilroy, J. B., A π-Conjugated Inorganic Polymer Constructed from

Boron Difluoride Formazanates and Platinum(ii) Diynes. *Chem. Comm.* **2018**, 54, 6899-6902.

3. Kajendirarajah, U.; **Avilés, M. O**.; Lagugné-Labarthet, F.; Deciphering Tip-Enhanced Raman Imaging of Carbon Nanotubes with Deep Learning Neural Networks. *Phys. Chem. Chem. Phys.* **2020**, 22, 17857-17866

4. Mazaheri, L; Jelken, J; **Avilés, M. O**; Legge, S; Lagugné-Labarthet, F; Investigating the Performance of Wide -Field Raman Microscopy with Stochastic Optical Reconstruction Post-Processing. *Appl. Spectrosc.***2020**, 76, 3, 340-351

5. Farhat, P; **Avilés, M. O**; Legge, S; Wang, Z; Sham, T.K; Lagugné-Labarthet, F; Tip-Enhanced Raman Spectroscopy and Tip-Enhanced Photoluminescence of MoS2 Flakes Decorated with Gold Nanoparticles. *J. Phys. Chem C.* **2022**, 126,16, 7086-7095

6. Jelken, J; **Avilés, M. O**; Lagugné-Labarthet, F; The Hidden Flower in WS_2 Flakes: A Combined Nano-Mechanical and Tip-Enhanced Raman Exploration. *ACS Nano.* **2022**, 16, 8, 12352–12363

7. **Avilés, M. O**; Jelken, J; Lagugné-Labarthet, F; Periodic Spiral Ripples on VS_2 flakes: A Tip-Enhanced Raman Investigation *J. Phys Chem. Lett.* **2022**,13,41, 9771-9776.

8. **Avilés, M. O**; Wang, Z; Sham, T.K; Lagugné-Labarthet, F; On the Oxidation of VS_2 2D platelets using Tip-Enhanced Raman Spectroscopy. *Curr. Opin. Solid State Mater. Sci.*- Submitted.

CONFERENCES POSTER AND TALKS

1. **Avilés, M. O**; Kozachuk, M.; Martin, R.; Sham, T.K.; Lagugné-Labarthet, F. (2018) Characterizing a 19th Century Hand-Colored Daguerreotype by Synchrotron, Micro-Raman, and Micro-Fourier Transform Infrared Spectroscopies. Ottawa, ON.

2. Dhindsa, J.; Maar, R.; Barbon, S.; **Avilés, M. O**.; Powell, Z.; Lagugné-Labarthet, F.; Gilroy, J.B. (2019) Low Band Gap Polymers and Model Compounds Derived from Boron Difluoride Formazanates and Platinum Diynes.

3. McRae, D. M; **Avilés, M. O**.; Lagugné-Labarthet, F. (2019) Localized Plasmon-Mediated Reduction of Diazonium Salts. Canadian Society of Chemistry Conference, Quebec City, QB.

4. McRae, D. M.; Therien, D. A. B.; **Avilés, M. O**.; Félidj, N.; Mangeney, C.; Lagugné-Labarthet, F. (2019) Functionalization of Metallic Nanostructures by Plasmon-Mediated Reduction of Diazonium Salts. International Conference on Enhanced Spectroscopies, London, ON.

5. **Avilés, M. O**.; Kajendirarajah, U.; Lagugné-Labarthet, F. (2019); Conference CCCE Poster. Title: Characterization of carbon-based materials using Tip-Enhanced Raman Spectroscopy, Quebec City, QB.

6. **Avilés, M. O**.; Farhat, P.; Lagugné-Labarthet, F. (2019); Tip-Enhanced Raman Spectroscopy of 2D MoSe2 flakes prepared by Liquid Exfoliation, NanoOntario Conference, Poster Session, November.
7. **Avilés, M. O**.; Farhat, P.; Lagugné-Labarthet, F. (2019); Tip-Enhanced Raman Spectroscopy of Semiconducting Materials, ICES4, Poster Session, June.
8. **Avilés, M. O**.; Lagugné-Labarthet, F. (2019); Characterization of carbon-based materials using Tip-Enhanced Raman Spectroscopy, CCCE 102nd Canadian Chemistry Conference and Exhibition, Poster Session, June.
9. Farhat P; **Avilés, M. O**.; Wang, Z; Sham, T. K.; Lagugné-Labarthet, F. (2020); Tip-Enhanced Raman Spectroscopy (TERS) of Transition Metal Dichalcogenides, Graphene & 2D Materials International Conference, November.
10. **Avilés, M. O**.; Kajendirarajah, U; Lagugné-Labarthet, F. (2020); Tip-Enhanced Raman Image Analysis of Carbon Nanotubes with Deep Learning Neural Networks, CCCE 103rd Canadian Chemistry Conference and Exhibition, Virtual Abstract, May.
11. **Avilés, M. O**.; Farhat, P; Wang, Z; Sham, T. K.; Lagugné-Labarthet, F (2020).; Tip-Enhanced Raman Spectroscopy of Vanadium Disulfide by Chemical Vapor Deposition, CCCE 103rd Canadian Chemistry Conference and Exhibition, Virtual Abstract, May.
12. Farhat, P**, Avilés, M. O**.; Wang, Z; Sham, T. K.; Lagugné-Labarthet, F (2021).; Raman and Photoluminescence of Au-decorated MoS2 flakes by Tip-Enhanced Scattering, CCCE 104th Canadian Chemistry Conference and Exhibition, Virtual Talk, June.
13. **Avilés, M. O.**; Wang, Z.; Sham, T. K.; Lagugné-Labarthet, F. (2021) Tip-Enhanced Raman Spectroscopy of Vanadium Disulfide flaked deposited by Chemical Vapor Deposition. Canadian Society of Chemistry Conference, Virtual Program Talk.
14. **Avilés, M. O.**; Lambin, C.; Lagugné-Labarthet, F. (2021), Exploring the hidden features in 2D Transition Metal Dichalcogenides. NanoOntario Conference, Virtual Program Talk.
15. Lambin, C.; **Avilés, M. O.**; Jelken, J.; Lagugné-Labarthet, F. (2022), Tip-Enhanced Raman Spectroscopy of CVD grown MoS2 flakes, CCCE 105nd Canadian Chemistry Conference and Exhibition, Poster, June.